Numerical Simulation of Pool Boiling from Reentrant Type Structured Surfaces

Numerische Simulation des Blasensiedens an hinterschnittenen Oberflächen
Vom Fachbereich Maschinenbau der Technischen Universität Darmstadt
zur Erlangung des akademischen Grades Doktor-Ingenieur (Dr.-Ing.)
genehmigte Dissertation von M.Sc. Jochen Dietl aus Ulm
Tag der Einreichung: 20.04.2015, Tag der Prüfung: 02.07.2015
Darmstadt 2015 — D 17

1. Gutachten: Prof. Dr.-Ing. Peter Stephan
2. Gutachten: Prof. Dr.-Ing. Johannes Janicka

TECHNISCHE
UNIVERSITÄT
DARMSTADT

TTD
Technische Thermodynamik

Numerical Simulation of Pool Boiling from Reentrant Type Structured Surfaces
Numerische Simulation des Blasensiedens an hinterschnittenen Oberflächen

Genehmigte Dissertation von M.Sc. Jochen Dietl aus Ulm

1. Gutachten: Prof. Dr.-Ing. Peter Stephan
2. Gutachten: Prof. Dr.-Ing. Johannes Janicka

Tag der Einreichung: 20.04.2015
Tag der Prüfung: 02.07.2015

Darmstadt — D 17

Bitte zitieren Sie dieses Dokument als:
URN: urn:nbn:de:tuda-tuprints-46535
URL: http://tuprints.ulb.tu-darmstadt.de/4653

Erklärung zur Dissertation

Hiermit versichere ich, die vorliegende Dissertation ohne Hilfe Dritter nur mit den angegebenen Quellen und Hilfsmitteln angefertigt zu haben. Alle Stellen, die aus Quellen entnommen wurden, sind als solche kenntlich gemacht. Diese Arbeit hat in gleicher oder ähnlicher Form noch keiner Prüfungsbehörde vorgelegen.

Darmstadt, den 20. April 2015

Jochen Dietl

Vorwort

Die vorliegende Ausarbeitung entstand im Rahmen meiner Anstellung als wissenschaftlicher Mitarbeiter am Institut für Technische Thermodynamik der TU Darmstadt. Betreut wurde ich bei meiner Arbeit vom Leiter des Instituts Prof. Dr.-Ing. Peter Stephan. Dabei konnte ich in großem Ausmaß von Herrn Stephans umfangreichen Erfahrungen profitieren und wertvolle methodische und inhaltliche Anregungen erhalten. Die Arbeitsbedingungen, die von Herrn Stephan am Institut geschaffen wurden, lassen keine Wünsche offen. Für die Möglichkeit, meine Dissertation in der Zeit meiner Anstellung anfertigen zu können, sowie die andauernde Unterstützung möchte ich mich herzlich bedanken.

Zu einem großen Anteil verdanke ich die Möglichkeit zur Promotion auch meinen Eltern, welche mir mein Studium finanziert, mich gefördert und angespornt haben. In allen Lebenslagen konnte ich mich stets darauf verlassen, dass mir vonseiten meiner Familie jede Unterstützung zukommt, die sie leisten kann.

Meine Kollegen in allen Funktionsbereichen sorgten dafür, dass ich meiner Beschäftigung mit viel Freude nachgehen konnte. Durch ihre Hilfsbereitschaft waren die Mühen der Anfertigung der Ausarbeitung leicht zu bewältigen. Hervorheben möchte ich dabei Martin Still sowie Stefan Batzdorf, die nicht nur meine Ausarbeitung korrigiert, sondern mir auch zuvor stets als Diskussionspartner und mit Ratschlägen unterstützend zur Seite gestanden haben.

Auch Christian Kunkelmann möchte ich an dieser Stelle noch einmal für die Betreuung meiner Masterarbeit und die Vorarbeit durch die Entwicklung des Simulationsmodells danken. Die postiven Erfahrungen, die ich während der Anfertigung meiner Masterarbeit sammeln konnte, haben zu meiner Entscheidung die Beschäftigung aufzunehmen mit beigetragen.

Achim Gotterbarm und Jean El Hajal von der Wieland-Werke AG möchte ich danken für die interessanten Diskussionen und Anregungen bezüglich meiner Forschungsarbeit. Ihr Blick aus der Praxis hat mir sehr dabei geholfen, geeignete Ziele für meine Arbeit festzulegen.

Für die Übernahme des Korreferats bedanke ich mich bei Prof. Dr.-Ing. Johannes Janicka.

Abstract

Enhancement of heat transfer in pool boiling can be achieved by employing a structured surface. So called reentrant type surfaces, consisting of subsurface tunnels connected through pores with the pool, were found to strongly improve the performance of heat exchanger tubes. Although employed since decades, several of the processes within the tunnel are not understood and the presented models are not able to predict the different boiling modes. With the rapid development of numerical methods in the last years, the simulation of boiling is possible by today, allowing to study the processes with high temporal and spatial resolution.

In the presented thesis, numerical simulations of boiling from reentrant type structured surfaces are performed. Processes are studied at single reentrant cavities and at a piece of subsurface tunnel with two pores. The dimensions and shapes of the cavity, tunnel, and pore are varied to obtain the influence of geometric properties on the process. Furthermore, a simplified model is created to calculate flow into the subsurface tunnel with reduced computational effort, in order to study a wider parameter range.

The employed numerical model is based on the VOF method and was validated in earlier works. In this work, the solver is adapted to work with capillary flows at low contact angles. The simplified model is based on solving the Young-Laplace equation to obtain the pressure jump at the bubble and the liquid film inside the structure. With the pressure differences the evolution of the liquid film during bubble growth and departure can be predicted. The results for the amount of liquid in the tunnel obtained from the numerical simulation and the simplified model are in good agreement.

Kurzzusammenfassung

Durch die Verwendung von strukturierten Oberflächen ist es möglich, den Wärmeübergang beim Blasensieden zu verbessern. Hinterschnittene Oberflächen, bestehend aus Kanälen, die über Poren mit dem Flüssigkeitsbehälter verbunden sind, haben sich dabei im Einsatz auf Wärmeübertragerrohren bewährt. Obwohl sich diese Strukturen seit Jahrzehnten im Einsatz befinden, sind einige Zusammenhänge noch nicht verstanden und vorhandene Modelle nicht in der Lage den Siedeprozess vorherzusagen. Durch die schnelle Entwicklung numerischer Methoden ist es heute möglich, Siedeprozesse zu simulieren und diese damit mit hoher zeitlicher und räumlicher Auflösung zu untersuchen.

In der vorliegenden Arbeit werden numerische Simulationen des Siedens an hinterschnittenen Oberflächen durchgeführt. Es werden die Prozesse in einzelnen Kavitäten sowie in einem Kanalausschnitt betrachtet. Die Form und Größe der Kavität, des Kanals und der Pore werden variiert, um den Einfluss der Geometrie auf den Prozess zu untersuchen. Weiterhin wird ein vereinfachtes Modell entwickelt, um die Strömung in den Kanal mit reduziertem Aufwand berechnen und eine größere Anzahl an Parameterkombinationen betrachten zu können.

Der verwendete Strömungslöser wurde bereits in vorangegangenen Arbeiten validiert und hier angepasst zur Berechnung kapillarer Strömungen bei kleinen Kontaktwinkeln. Das vereinfachte Modell basiert auf der Lösung der Young-Laplace Gleichung, um den Drucksprung an den Phasengrenzen zu erhalten. Mithilfe der Druckdifferenzen kann der Zusammenhang zwischen Blasenwachstum und Entwicklung des Filmvolumens berechnet werden. Bei der Vorhersage des Filmvolumens im Kanal zeigen die numerische Simulation und das vereinfachte Modell eine gute Übereinstimmung.

The results of the simulations show that with single reentrant cavities obtaining thin film evaporation inside the cavity is difficult if only one pore exists at each cavity. Introducing an additional channel next to the pore, connecting the liquid pool with the liquid film, similar processes can be observed inside the cavity as observed with subsurface tunnels. Simulations with the section of the subsurface tunnel indicate a strong dependence of the processes on pore size but also pore shape. With the given geometry, very high heat transfer coefficients are obtained, caused by the evaporation of the thin liquid films inside the structure.

From the parameter study with the simplified model, the influence of geometric properties on the operation range of the surface can be deduced. Furthermore, the model gives characteristic dimensionless parameters governing the process. Small bubble diameters as well as wide and deep tunnels are beneficial to prevent flooding of the structures. The point of dryout is delayed with a large open pore area. The introduction of two additional sub-stages of the boiling modes is suggested, namely the vapor expansion stage and the partial dryout stage, which should be considered in future modeling approaches.

In summary, numerical simulations and analysis of the boiling process from structured surfaces performed in this work, improve the understanding of the interrelations of important parameters and lead to suggestions regarding the design of the surfaces and modeling of the heat transfer.

Die Ergebnisse der Simulationen zeigen, dass es schwierig ist, mit isolierten Kavitäten mit einer einzigen Pore stabile Flüssigkeitsfilme in der Kavität zu erhalten. Mit einer zusätzlichen Verbindung zwischen Flüssigkeitsfilm und Flüssigkeitsbehälter ist es dagegen möglich, ähnliche Siedeprozesse in der Kavität zu beobachten, wie sie auch in Kanälen mit Poren auftreten. Die Ergebnisse der Simulation mit dem Kanalausschnitt deuten auf einen großen Einfluss der Porengröße und Porenform auf den Betriebszustand hin. Durch die Verdampfung dünner Flüssigkeitsfilme in der Struktur erhält man sehr hohe Wärmeübergangskoeffizienten für die eingesetzten Geometrien.

Die Parameterstudie unter Verwendung des vereinfachten Modells erlaubt die Untersuchung des Einflusses geometrischer Größen auf den Betriebsbereich. Basierend auf dem Modell können außerdem charakteristische dimensionslose Größen abgeleitet werden, die den Siedeprozess bestimmen. Kleine Blasen zusammen mit tiefen und breiten Kanälen verhindern ein Fluten der Struktur. Das Austrocknen der Struktur kann mit großen offenen Porenflächen vermieden werden. Es wird vorgeschlagen zwei zusätzliche Betriebszustände in zukünftigen Modellierungsansätzen zu berücksichtigen, welche das partielle Fluten und das partielle Austrocknen der Struktur abbilden.

In dieser Arbeit wurden numerische Simulationen und eine Analyse des Siedeprozesses an strukturierten Oberflächen durchgeführt. Beides fördert das Verständnis der Zusammenhänge zwischen den Parametern und führt zu Empfehlungen in Bezug auf die Gestaltung der Struktur und der Modellierung des Wärmetransportes.

Contents

Nomenclature

Latin letters		Unit
A	Dispersion constant	J
	Area	m^2
a	Capillary length	m
c	Specific heat capacity	J/kg K
d	Diameter	m
F	VOF indicator variable	-
	Force	N
f	Frequency	1/s
	Evaporation coefficient	-
$\mathbf{f}$	Force vector	N
g	Gravitational acceleration	m/s^2
H	Enthalpy	J
h	Heat transfer coefficient	$W/m^2\,K$
	Height	m
$\dot{h}$	Specific enthalpy source	W/m^3
Δh_v	Specific heat of vaporization	J/kg
k	Thermal conductivity	W/m K
L	Length	m
$\dot{m}$	Mass flow	kg/s
N	Number	-
n	Number density	$1/m^2$
$\mathbf{n}$	Interface normal vector	-
p	Pressure	N/m^2
Q	Heat	J
$\dot{Q}$	Heat flow	W
q	Heat flux	W/m^2
R	Thermal resistance	m^2K/W
	Radius	m
R_{gas}	Specific gas constant	J/kg K
r	Radial coordinate	m
s	Path coordinate	m
T	Temperature	K, °C

u	Velocity	m/s
$\mathbf{u}$	Velocity vector	m/s
$\mathbf{u}_\mathrm{r}$	Compressive velocity vector	m/s
V	Volume	m^3
x, y, z	Cartesian coordinates	m

Greek letters		**Unit**
β	Thermal expansion coefficient	1/K
δ	Film thickness	m
ζ	Flow resistance	$\mathrm{Pa\,s/m^3}$
η	Coordinate normal to wall	m
$\varTheta$	Contact angle	rad, deg
κ	Curvature	1/m
μ	Dynamic viscosity	kg/m s
ν	Kinematic viscosity	$\mathrm{m^2/s}$
ξ	Coordinate parallel to wall	m
ρ	Density	$\mathrm{kg/m^3}$
$\dot{\rho}$	Specific mass source	$\mathrm{kg/s\,m^3}$
σ	Surface tension	N/m
τ	Time	s
$\varPhi$	Distance Field	m
φ	Angle	rad
χ	Physical property	-
$\Delta\varPsi$	Diffusion length scale	m
ψ	Diffused mass source	$\mathrm{kg/m^3\,s}$
Ω	Computational domain	m^3

Subscripts

0	Initial value
a	Active pores
ad	Adsorbed
b	Bubble
buoy	Buoyancy
c	Cavity
cap	Capillary
ch	Channel
char	Characteristic
cell	Numeric cell
cl	Contact line
dep	Departure
dist	Distance
drag	Drag
dyn	Dynamic
ex	External
f	Film
h	Height
i	Inertia
in	Internal
int	Interface
l	Liquid
le	Ledge
lift	Lift
lo	Lower
m	Meniscus
max	Maximal
ne	Non-evaporating
new	New value
old	Old value
out	Outer area
p	Pore
ref	Reference
res	Residual
s	Solid
sat	Saturation
t	Tube

th	Thermal
tun	Tunnel
up	Upper
v	Vapor
w	Wall

Superscripts

$'$	Derivative with respect to coordinate
$\cdot$	Derivative with respect to time
$*$	Dimensionless

Characteristic Numbers

Bo	Bond number
Pr	Prandtl number
Re	Reynolds number

Abbreviations

2D	Two-dimensional
3D	Three-dimensional
ALE	Arbitrary Lagrangian-Eulerian
CFC	Chlorofluorocarbon
CFD	Computational fluid dynamics
CFL	Courant-Friedrichs-Lewy number
CLSVOF	Coupled Level-set Volume-of-fluid
CSF	Continuous surface force
CSS	Continuous surface stress
DNB	Departure from nucleate boiling
FT	Front-tracking
HPLS	Hybrid Particle-level-set
LS	Level-set
MAC	Marker-and-cell
MULES	Multidimensional universal limiter with explicit solution
ONB	Onset of nucleate boiling
PF	Phase-field
PISO	Pressure implicit split operator
PLIC	Piecewise linear interface calculation
PPIC	Piecewise parabolic interface calculation
SLIC	Simple line interface calculation
VOF	Volume-of-fluid

1 Introduction

Phase change and boiling are employed in many devices requiring the transfer of heat. Applications can be found basically in every branch of industry as well as the private sector. To increase efficiency and reduce size and costs of heat exchangers, enhancement techniques were developed. In pool boiling heat transfer, enhanced surfaces are commonly employed, where the heat transfer surface is structured on the scale of single bubbles.

Boiling is a complex, seemingly chaotic process, which leads to difficulties in predicting characteristic properties. With the prediction of boiling heat transfer on plane surfaces already being challenging, models for predicting heat transfer with enhanced surfaces are rare. With the lack of accurate models, development of boiling surfaces is in large parts based on empirical work. Therefore, increasing the understanding of the different processes occurring at enhanced surfaces and the influence of geometric parameters is the goal of ongoing research.

Experiments have been the backbone of the research on boiling processes with enhanced surfaces. Thermal measurements and visualization studies were performed on the scale of heat exchangers, single tubes as well as single nucleations sites with bubble interaction and isolated bubbles. With sophisticated experimental techniques, the location of liquid films inside micro-structures and temperature gradients within the wall can be determined.

In the last decade, numerical studies of the boiling process were frequently performed accompanying experimental works to obtain additional information about properties and gain insight into details. On the larger scales Euler-Euler methods are employed, which are not resolving the processes occurring at single bubbles. At the scale of single bubbles, interface resolving techniques are state of the art. As numerical simulations theoretically have no limitations in resolving time and space, they provide an excellent method for studying processes on this scale in boiling heat transfer.

With several numerical codes for simulating phase change and boiling being well tested and validated by today, numerical simulations are performed which are uncoupled from experimental works. Without the limitations of experimental boundary conditions, the influence of single parameters and the interrelation of processes can be investigated. The rapid development of computing power and numerical methods is constantly pushing the boundaries of what is feasible.

In this work, processes occurring with a certain kind of enhanced boiling surfaces are studied with the help of numerical methods. In Chapter 2 these surfaces are described and the current knowledge about the processes is presented. The numerical method is introduced in Chapter 3. Chapter 4 and Chapter 5 are devoted to the simulation setup and results, which are obtained with the presented model. From the simulation results important processes are identified and modeled in Chapter 6. By this it is possible to extend the parameter range examined in this work and obtain additional information about interrelations of surface and heat transfer properties. The findings are discussed with regard to the application in Chapter 7. Finally, Chapter 8 gives the summary and conclusion of this work.

2 State of the Art

The boiling process has been scientifically investigated for more than a century. Descriptions of the fundamentals of phase change and boiling processes can be found in various textbooks such as Carey [19] or Baehr and Stephan [9]. In this chapter, a short overview of boiling enhancement methods is given, followed by an extensive literature review concerning boiling from reentrant type surfaces and numerical simulations of nucleate boiling. But first, some of the terms commonly employed when describing boiling processes and repeatedly appearing in this work are given.

Each boiling process can be characterized by an individual boiling curve. The boiling curve relates the heat flux q at the surface with the superheat $\Delta T = T_\mathrm{w} - T_\mathrm{sat}(p)$ of the surface. The concept of the boiling curve was introduced by Nukiyama [97] and is given for a typical pool boiling process qualitatively in Figure 2.1.

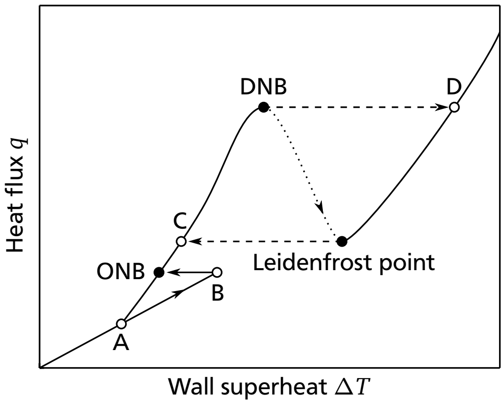

Figure 2.1: Pool boiling curve according to Nukiyama [97]

In technical applications, the heat transfer coefficient given by $h = q/\Delta T$ is often the parameter of interest. Therefore, instead of plotting q versus ΔT, the heat transfer coefficient h versus ΔT or versus q is often given in heat transfer studies.

Starting with a fluid at saturation temperature and a wall superheat of $\Delta T = 0$, increasing the heat flux leads to an increase in wall superheat without bubbles to appear, first. At the wall, a thermal boundary layer develops with the fluid temperature locally exceeding saturation temperature. Heat is transferred from the wall to the fluid by natural convection. In order for bubbles to appear, nucleation is required. In Figure 2.1, the point where the first nucleation site is activated is given by the letter B.

It is distinguished between homogeneous nucleation and heterogeneous nucleation. With homogeneous nucleation, the superheat of the fluid needs to be high enough to drop out of the metastable regime of a superheated liquid. In technical applications, typically heterogeneous nucleation occurs at small amounts of entrapped gas or vapor at small surface defects or discontinuities. Once the first bubble grows, the heat transfer coefficient suddenly increases and the surface temperature decreases from point B to the point ONB, which is the onset of nucleate boiling. This is where the nucleate boiling regime is located.

In the nucleate boiling regime, first, isolated bubbles grow on the surface at active nucleation sites and depart. With increasing heat flux, the number of active nucleation sites and the bubble density increase.

The heat transfer coefficient typically increases with heat flux due to the increase in active nucleation sites. Once the bubble density is high enough, bubbles start to interact and bubble merger can occur.

With more and more vapor being created with rising heat flux, the departure from nucleate boiling DNB is reached eventually. At this point, phase change is fast enough at the wall for no more liquid being able to wet the surface. Therefore, the heat transfer coefficient drastically decreases which can lead to a sudden increase in wall superheat, indicated by the arrow between point DNB and point D in Figure 2.1. The heat flux at this point is often referred to as the critical heat flux.

Point D lies in the film boiling regime, which starts at the Leidenfrost point. If the heat flux is decreased, the wall superheat is not decreasing back to the point DNB. Instead, the heat flux needs to be decreased below the heat flux at the Leidenfrost point to reach the nucleate boiling regime again. In this case, due to the sudden increase of the heat transfer coefficient, the wall superheat decreases and jumps to point C in Figure 2.1.

If the heat flux is decreased further, the nucleation sites can stay active below the heat flux which was required to activate them. Finally, at point A, the nucleate boiling regime is left again and natural convection occurs only.

The effect that the required superheat to activate the nucleation sites at point B can be higher than the wall superheat at which the nucleate boiling regime is left at point A is called boiling hysteresis. Depending on wall roughness and purity of the fluid the boiling hysteresis can be less or more pronounced. The boiling hysteresis can be reduced or completely avoided if boiling occurred at the surface before.

Even though extensively studied, predicting the boiling curve for a certain set of parameters is very difficult and associated with a high level of uncertainty.

2.1 Enhancement of boiling heat transfer

Boiling is a highly efficient method of heat transfer and employed in many industrial applications. Consequently, there is a strong urge to control and improve the process. Well known reviews about enhancement of boiling heat transfer were published by Thome [121] or Webb and Kim [127].

Methods for enhancing boiling heat transfer can be separated in active methods, such as vibration or jet impingement, and passive methods. Active systems require some sort of power supply and control system while passive systems are driven by the boiling process itself. Therefore, it is beneficial to try to fulfill the heat transfer task with passive systems before employing active methods.

The performance of a heat transfer surface with phase change occurring is characterized by an individual boiling curve. Next to the heat transfer coefficient at the design point, the onset of nucleate boiling, dryout and boiling hysteresis are of special interest. In technical applications, also the influence of fouling and aging of the surface is of importance. Onset of nucleate boiling and dryout typically limit the range that the surface can be operated in with a high heat transfer coefficient. Going beyond the point of dryout can have drastic consequences as the surface temperature strongly increases and can exceed the melting point of the employed wall material. In most cases the boiling hysteresis is undesired. A strong hysteresis requires the surface to be considerably superheated before the nucleate boiling regime and consequently the operation range is obtained. Aging of the surface is one of the aspects often preventing the transfer of seemingly promising surface technology from academic research to industrial application.

Passive methods to increase the heat transfer in boiling often aim at

- increasing the heat transfer area,
- increasing the nucleation site density,
- creating thin liquid films at the surface.

To do so, the wetting characteristics can be adapted by coatings of the surface or supplements in the fluid, or the surface can be structured. In many industrial applications, good results are obtained with surface structuring. Surfaces can be roughened, porous, nano structured, or micro structured on the scale of the bubble. Also composite surfaces combining two or more of those properties are possible. All of those surface structures show an improvement of the heat transfer coefficient in certain parts of the boiling curve compared to a plain surface.

Nano structured surfaces are mostly created by some kind of coating. Therefore, they suffer like other coatings rather strongly from aging. Furthermore, with nano structures, the manufacturing processes are still in the development. The effect of roughness mainly is due to an increase in nucleation site density. The enhancement of the heat transfer is limited as no thin films are created. Porous surfaces as well as micro structured surfaces typically combine an increase in area, increase in nucleation site density, and creation of thin liquid films if designed correctly. Porous surfaces show a strong increase of the heat transfer coefficient at rather low heat fluxes, but dryout is observed earlier. Micro structured surfaces often require a higher wall superheat than porous surfaces to be activated but show extremely high heat transfer coefficients over a wide range of heat fluxes. As the openings in the surface are larger than with porous surfaces, fouling is less critical. Due to these properties, micro structured surfaces are widely employed in evaporators and condensers.

For flooded evaporators, micro structured surfaces are employed on the outer side of the heat exchanger tubes, located in the refrigerant. A review on flooded evaporators is given by Browne [17]. For those tubes, reentrant type structures were developed which are the topic of the next section.

Currently, there is no complete model describing the evaporation from reentrant type surfaces and many effects are not understood. Therefore, the development of structured boiling surfaces is still mainly based on empirical methods.

2.2 Pool boiling from reentrant type surfaces

This section gives an overview of the open literature dealing with reentrant type surfaces for enhancing nucleate pool boiling. Reentrant type surfaces considered here are single reentrant cavities and surfaces consisting of subsurface tunnels which are connected through pores with the liquid pool. Typically, a cavity is referred to as reentrant cavity if it is connected through a pore of smaller dimensions to the liquid pool, as illustrated in Figure 2.2. In pool boiling, such a reentrant cavity is on the scale of a single bubble departing at the pore.

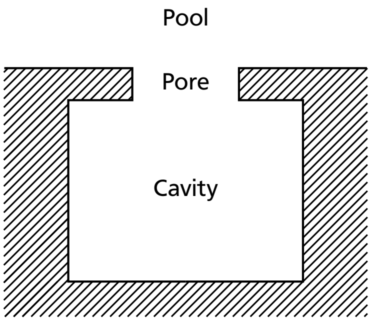

Figure 2.2: Illustration of reentrant cavity

2.2.1 Boiling from single reentrant cavities

Experimental studies of boiling at single reentrant cavities with clearly defined geometry are rare. In boiling experiments some authors employ cavities on the surface to obtain stable nucleation sites or to control the spacing and number of nucleation sites. These cavities often either have an undefined geometry (see e.g. [109]) or are of cylindrical or conical shape.

Fabricating single reentrant cavities on a heater is difficult and to the knowledge of the author, no studies were performed aiming at observing processes occurring inside the cavities up to now. Ragi [101] introduced a method to form single reentrant cavities by brazing a shaped foil onto a structured base surface, with the pores being pierced into the foil. Boiling from those surfaces showed an increase compared to a plain surface and an increase of the heat transfer coefficient with cavity density.

Marto and Rohsenow [84] performed boiling experiments with sodium at single reentrant cavities with a pore diameter of 100 µm without giving a comment on the fabrication procedure. They showed that the cavities act as stable nucleation sites and required the lowest wall superheat for activation of all surfaces tested.

The group of Bhavnani and Jaeger (Phadke et al. [98], Goyal et al. [42], Bhavnani et al. [13], Nimkar et al. [96]) tested surfaces with equally spaced reentrant cavities made of silicon for chip cooling with different refrigerants. The cavities had a pyramidal shape with a square pore. The edge length of the pore was in a range between 12 µm and 500 µm. The distance between the cavities was varied. The surfaces were mounted vertically on a heater such that the cavities interact through rising bubbles. Comparing the studies, considerable differences in the heat transfer coefficient can be observed for different surface.

Kubo et al. [66] performed experiments on a horizontal heater with circular reentrant cavities and FC-72 as working fluid. The cavities were manufactured in silicon with very small pore diameters ranging from 1.6 µm to 3.1 µm. The pore diameter as well as number of cavities on the heater were varied. The influence of degassing and subcooling on nucleate boiling from such a surface was studied. It was observed that with a degassed fluid the boiling hysteresis increases and the heat transfer coefficient decreases.

Shoji and Takagi [108] manufactured a single reentrant cavity with a micro-electrical discharge machine in copper and took measurements with water as working fluid. The cavity had a diameter of about 100 µm , the pore diameter is not given. The experiments demonstrated that the cavity worked as stable nucleation site and wall superheat was lower compared to a conical cavity.

2.2.2 Boiling from subsurface tunnels

Subsurface tunnels with pores can be found on the outside of tubes for heat exchangers. These tubes are used for example in shell and tube type heat exchangers and flooded evaporators in refrigeration, process, and petrol industry. By employing enhanced surfaces, the size of the heat exchanger or the driving temperature differences can be decreased. Figure 2.3 shows a cut through such a tubular surface with subsurface tunnels.

Figure 2.3: Tubular surface with subsurface tunnels

The structure is fabricated by a rolling process. First, fins are created forming the tunnel and afterwards the tips of the fins are split or bent and further deformed to close the tunnel and form the pores. By this, a continuous tunnel is formed reaching from end to end of the tube. Typical depths of the subsurface tunnels are 0.6 mm to 1 mm. Pore diameters can be found between 0.06 mm to 0.5 mm.

Kim and Choi [59] divided such subsurface structures found on tubes into three categories, shown in Figure 2.4.

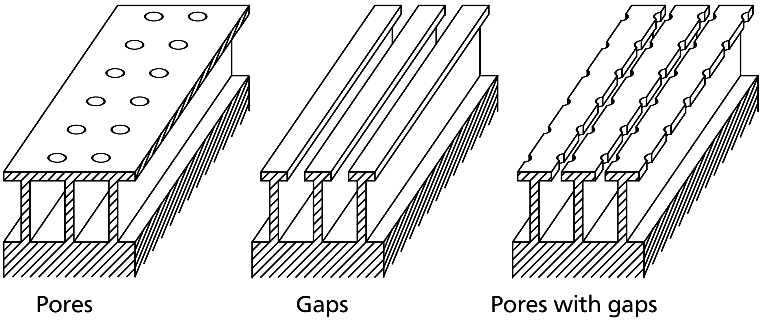

Figure 2.4: Characterization of subsurface tunnels according to Kim and Choi [59]

They suggested distinguishing the surfaces by the way the tunnel is connected to the liquid pool. Due to the complex manufacturing process and small sizes, it is often difficult to characterize the real surfaces in terms of clearly defined geometric shapes. Instead, pores can be somewhere in-between circular, square, or rectangular and in the tunnel there might be ledges and corners with variations in opening angle and base radii.

There are several different tubes available with reentrant type structures. Well known manufacturers include Wieland-Werke AG, Wolverine Tube Inc. and Hitachi Ltd. Experiments with their tubes can be found in literature. The evaporator tubes employed in experiments and developed by these companies include

Wieland-Werke AG: GEWA-T, GEWA-TX, GEWA-SE, GEWA-YX, GEWA-B, and GEWA-PB,

Wolverine Tube Inc.: Turbo-B, Turbo-BII HP, and Turbo-BII LP,

Hitachi Ltd.: Thermoexcel-E and Thermoexcel-HE.

GEWA-T is a tube with subsurface tunnels connected through a gap to the liquid pool. GEWA-TX, GEWA-SE, and GEWA-YX are modified versions of this tube. With GEWA-B and GEWA-PB tubes the subsurface tunnels are connected through pores to the liquid pool. For comparisons, measurements are also sometimes performed with a GEWA-K tube, which is a standard low fin tube. Figure 2.5 shows a cut through a GEWA-PB boiling surface.

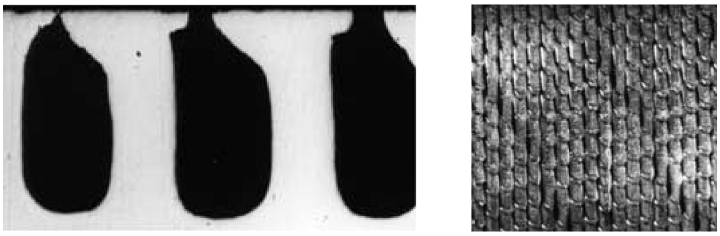
Side view
Top view

Figure 2.5: GEWA-PB tube, from Chen et al. [23]

The Turbo-B tube was the first tube with subsurface tunnels manufactured by Wolverine Tube Inc., appearing in the open literature. The Turbo-BII tube was introduced later and there exist versions for high pressure refrigerants (HP) and low pressure refrigerants (LP). Here, the tunnel is connected by pores with the pool. Figure 2.6 shows the Turbo-BII HP tube.

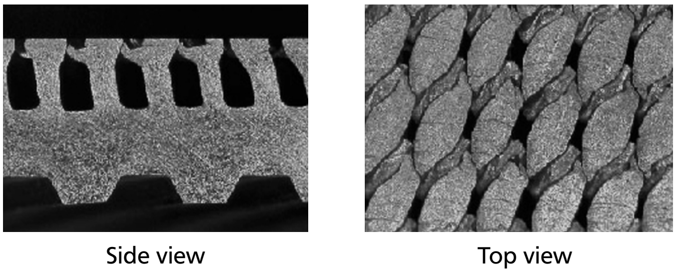

Figure 2.6: Turbo-BII HP tube, from Kedzierski [57]

Tubes with porous coatings are sometimes referred to as reentrant tubes as well. They tend to have high heat transfer coefficients at lower heat fluxes, but can be more prone to fouling and the critical heat flux is reached earlier. The cavities in porous coatings usually have no defined geometry. Therefore, such surfaces are not further considered in this section. It shall be noted that some authors use porous coated surfaces (e.g. Linde High Flux) to compare their results obtained with other structured surfaces.

Boiling characteristics

In order to gain a better understanding of the processes and phenomena occurring inside the subsurface tunnels and at the pores of the reentrant surfaces, several authors performed visualization studies. Nakayama [95] proposed three boiling modes, illustrated in Figure 2.7.

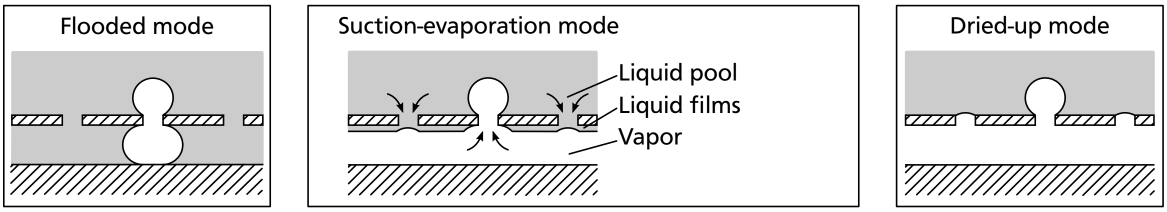

Figure 2.7: Boiling modes according to Nakayama [95]

Flooded mode: In the flooded mode, the subsurface tunnels are mainly filled with liquid and evaporation occurs only from single nucleation sites located inside the tunnel or on the outer surface.

Suction-evaporation mode: During the suction evaporation mode, which is the most effective boiling mode, evaporation occurs from liquid menisci in the corners of the subsurface tunnels. Ayub and Bergles [7] stated that all of the wall surface in the tunnel is covered with a thin liquid film. According to Chien and Webb [28], evaporation occurs mainly at liquid menisci in the corners and a small portion at a liquid film on the side walls. As an increase in heat transfer has been observed for a tunnel with rectangular shaped tunnel base compared to a tunnel with circular base, the theory of evaporating liquid menisci is generally widely accepted.

Dried-up mode: At high heat fluxes the dried-up mode can occur. Liquid menisci are completely evaporated and no more liquid can enter the tunnel. Consequently, evaporation can only occur on the outer surface of the tubes and the heat transfer coefficient typically decreases.

The boiling modes are widely accepted to be an adequate characterization of the physical processes and several authors were able to observe these boiling modes [7][28][29][133]. Still, some details of the processes and the influence of the different parameters are a subject under discussion.

Wondra et al. [133] observed further rising heat transfer coefficients for $q > 100\,\mathrm{kW/m^2}$ and suggested an additional boiling mode after the dried up regime, which is also able to transfer heat very effectively. They assumed a kind of flow-boiling in the reentrant tunnel as because of pressure fluctuations liquid might be able to enter the tunnels from time to time.

While Luke and Kruck [79] assumed that vapor flows around the tube inside the tunnel, others observed bubbles leaving the tunnel not only at the top, but also at the bottom [7][87]. It is also possible that nucleation occurs at the outer surface if the reduced pressure is high enough [41]. In general, it can be observed that the number of active pores is increasing with heat flux [22][25].

By counting bubbles and estimating bubble diameters, some authors evaluated the heat which is removed as latent heat with the vapor from the surface [22][25][93]. Figure 2.8 shows the latent heat ratio from some of their measurements. The latent heat ratio is the latent heat related to the total heat transferred.

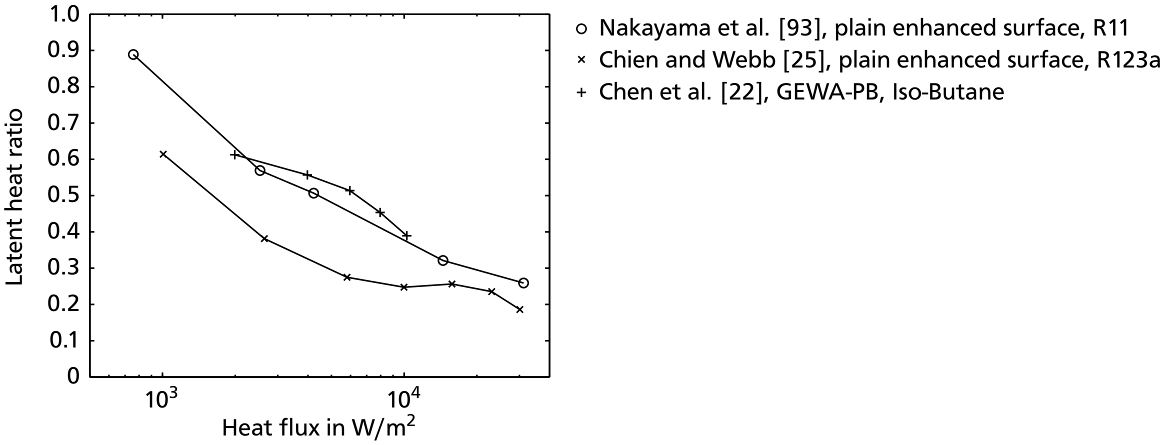

Figure 2.8: Ratio of the latent heat to total heat transfer

From their data it can be concluded that the latent heat ratio is decreasing with increasing heat flux. With increasing heat flux, more vapor is produced and consequently convective heat transfer on the outer surface increases. Chien and Webb [25] reported that surfaces with higher heat transfer coefficients show higher latent heat ratios. They concluded that evaporation from the subsurface tunnel is the most effective and important heat transfer mechanism.

Heat transfer performance

Many experiments were conducted to determine the heat transfer performance of tubes with various fluids. Especially in many older studies, chlorofluorocarbons (CFC) like R11 or R22 were used as working fluids, which have a high ozone-depleting potential and are banned today. Figure 2.9 shows heat transfer coefficients from experiments with fluid R134a and different surfaces. R134a is widely used in refrigeration processes and thus one of the fluids frequently employed in measurements. Comparing the results, a large variation in heat transfer coefficients can be observed even though the fluid is the same and all of the employed structures consist of subsurface tunnels with pores. Obviously, small changes in geometry and pressure can lead to a significant performance increase or decrease.

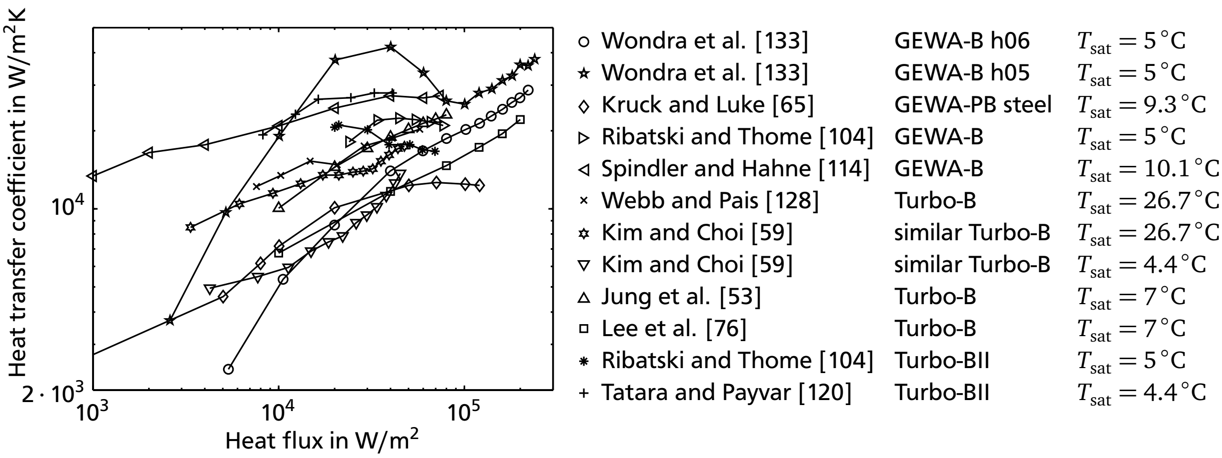

Figure 2.9: Boiling curves from literature with fluid R134a

Similar to plain surfaces, the heat transfer coefficient mostly increases with heat flux [23][53][54][76][79][120][128][134]. In some cases, the wall superheat even decreases with rising heat flux [133]. A surface at which the wall superheat is constant and thus independent from the heat flux is considered an ideal boiling surface. For GEWA-B and Turbo-BII HP with R134a, Ribatski and Thome [104] observed a reduction in heat transfer coefficient with rising heat flux, which is opposed to the results of Tatara and Payvar [120] for the same fluid and tube and could not be explained.

The heat transfer coefficient is also increasing with reduced pressure [23][41][53][59][65][79][80][89]. Jung et al. [54] showed that this is not only true for halogenated refrigerants but also hydrocarbons such as isobutane (R600a), butane (R600), propane (R290), propylene (R1270) and dimethylether (RE170). No explanation can be given for the results of Mertz [87] which show no dependence of the heat transfer coefficient on pressure for some surfaces. Nakayama et al. [95] found an improvement of heat transfer with rising pressure only at low heat fluxes. Ribatski and Thome [104] found only little influence of pressure and no clear trend.

The experiments show that for most parameters, reentrant type surfaces generally have a much better performance than finned tubes. While it is likely that the improvement of the heat transfer with standard low-fin tubes is mainly based on the increased surface area, different boiling phenomena occur with reentrant cavities, increasing the heat transfer far beyond an improvement which could be obtained with an increased surface area. This was concluded by Ayub and Bergles [7], who conducted measurements with water and R113 on plain, GEWA-T, and standard low fin GEWA-K tubes. They found that the fin density of the GEWA-K tubes had little effect on the performance and if one evaluated the data on basis of the total surface area, there was virtually no difference. Similar observations were made by Memory et al. [86] as well as Ribatski and Thome [104] at a lower heat flux.

In order to evaluate the performance of reentrant tubes, an enhancement factor was defined which relates the heat transfer coefficient of the structured surface to that of a plain surface. It is important to note which surface area is chosen to define the heat transfer coefficient, as the area can be calculated with the inner diameter, the outer diameter or the wetted area. Ribatski and Thome [104] also point out that for plain tubes the roughness has a strong influence on the heat transfer and show that enhancement factors are quite different if calculated with a rough tube instead of an industrial manufactured tube.

Figure 2.10 shows some of the measured enhancement factors found in literature. For the cases where heat transfer data for the plain tube was evaluated at different heat fluxes than the data for the enhanced tube, the heat transfer coefficients of the enhanced tube is interpolated to the heat flux values of the plain tube.

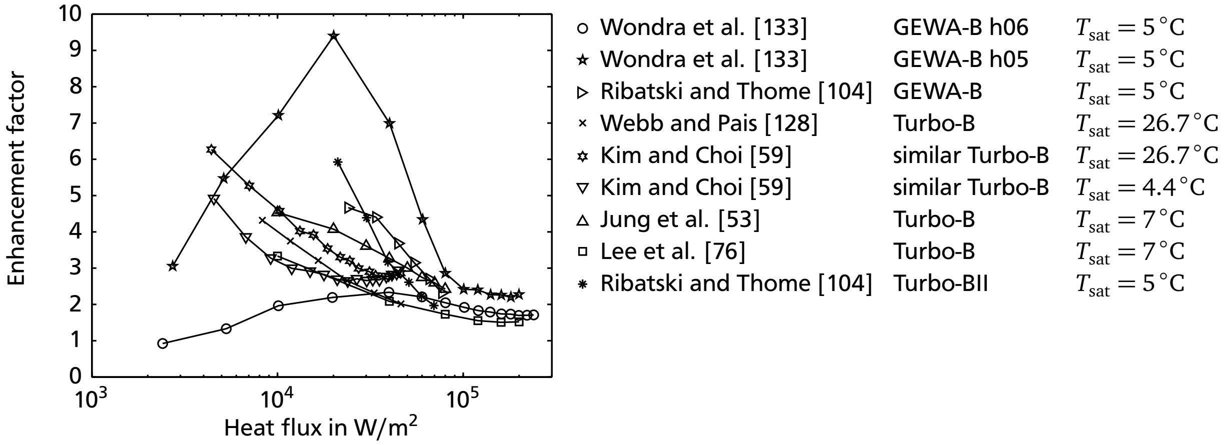

Figure 2.10: Heat transfer enhancement from literature with fluid R134a

Enhancement factors usually are highest at low heat fluxes and the performance gets similar to plain tubes with rising heat fluxes [41][79][104][123]. Some authors even reported worse heat transfer coefficients than with plain tubes for high heat fluxes [23][87]. The same applies for rising reduced pressure [41][65][79][87][89]. Therefore, fluids having a low vapor pressure take longer advantage of an enhanced boiling surface with rising heat flux [54]. Jung et al. [53] and Luke and Müller [80] argued that the relative advantage of using boiling surfaces is less if already many nucleation sites are activated, which is the case for both of these conditions. Opposed to that, Rajalu et al. [102] found a slight increase of the enhancement factor with heat flux for a heat flux in the range between 11 kW/m^2 and 42 kW/m^2. No explanation was given. Also the boiling data of Wondra at al. [133] show an increase of the enhancement factor with heat transfer .

Several authors noted that the boiling hysteresis can be significantly reduced when using reentrant type surfaces [8][23][24]. Small pores seem to have a positive effect on the temperature overshoot [123]. Chen et al. [23] argued that the best performing tubes also have the lowest temperature overshoot and vice versa. This is not in agreement with the results of Kedzierski [56]. In his experiments, temperature overshoots were considerably lower with GEWA-K tubes, which is a standard finned tube, than with Turbo-BII-LP tubes. Apparently the boiling hysteresis is strongly influenced by the surface-fluid combination.

Crossover characteristic and influence of geometry

The gap width or the pore diameter connecting the subsurface tunnel with the liquid pool have a strong influence on the boiling performance [7][8][93]. In general, there seems to exist an optimal gap width or pore size, which is different for each fluid and working condition [24][27][28][59][86][94][95][128]. Chien and Webb [28] observed a “crossover characteristic” illustrated in Figure 2.11, which was confirmed by other authors also for other surface-fluid combinations. According to the concept of the crossover characteristic, a surface having small pores has a high performance at a low heat flux but dries out early, while bigger pores perform better at higher heat fluxes but are flooded more easily at lower ones. The pore pitch has a similar effect as the pore diameter in this case as the total area connecting the tunnels with the pool is affected by both parameters. In this context, comparing GEWA-T and Thermoexcel-E tubes, Marto and Lepere [83] noticed that GEWA-T is usable at higher heat fluxes because of larger openings but that the necessary superheat for activation of the nucleation sites is higher, too.

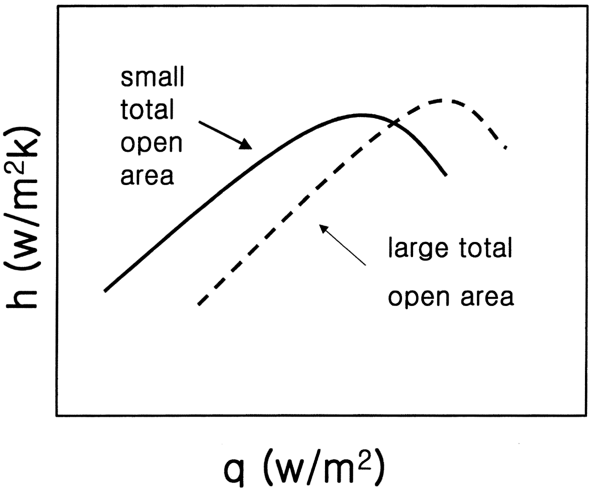

Figure 2.11: Illustration of the "crossover characteristic", from Kim and Choi [59]

It can be observed that the factor $\rho_\mathrm{v}\Delta h_\mathrm{v}$ has a similar influence on the boiling mode as the pore size. For the same heat flux, a low value of $\rho_\mathrm{v}\Delta h_\mathrm{v}$ leads to more created vapor volume than a high value of $\rho_\mathrm{v}\Delta h_\mathrm{v}$. Is the factor high, tunnels are more easily flooded but the dryout occurs later [24][133]. Wondra et al. [133] explained the better performance of R134a compared to FC-72 with the two times higher value of $\rho_\mathrm{v}\Delta h_\mathrm{v}$ with R134a.

Some authors state that the size of the tunnel is less important than gap width or pore diameter. But it seems like a rectangular fin base leads to a higher heat transfer than a circular fin base. Wondra et al. [133] observed a strong dependence of the heat transfer on the tunnel height. They argued that at lower heat fluxes a smaller tunnel allows an earlier shift into the suction evaporation mode, which is consistent with the observations for different values of $\rho_\mathrm{v}\Delta h_\mathrm{v}$.

Analyzing the heat transfer data, it can be concluded that heat transfer coefficients are much higher when using surfaces with pores instead of a circumferential gap, connecting the subsurface tunnel with the pool of fluid. Typical enhancement factors for GEWA-T tubes are about 3 to 5, while for GEWA-B, Thermoexcel-E, or Turbo-BII tubes factors between 7 and 15 were observed.

Further effects relevant for application

In industrial applications, tubes with structured surfaces are usually employed in bundles and with fluids which can show oil contamination from pumps. The influence of those conditions were addressed in several experimental setups.

For plain tubes it has been reported that lower tubes in a pool increase the heat transfer of upper tubes within a tube bundle because of the increased convection at the upper tubes. Two parameters were defined to quantify this effect.

Bundle effect: Ratio between the heat transfer coefficient of the upper tube with lower tubes activated and the heat transfer coefficient of the same tube if activated alone.

Bundle factor: Ratio between the average heat transfer coefficient of a whole tube bundle and the heat transfer coefficient of a single, isolated tube.

With tubes having reentrant type surfaces, the bundle effect is less pronounced than with plain tubes. This leads to the conclusion that the heat transfer in the subsurface tunnels is hardly affected by the fluid flow outside and heat transfer is dominated by nucleate boiling [123]. Memory et al. [85] found a positive bundle effect for Thermoexcel-HE and Turbo-B tubes with R114, which decreases with rising heat flux. Opposed to that, Trewin et al. [123] reported that with GEWA-T tubes the heat transfer coefficient is the same or even lower when used in bundles. They said, suppression of nucleate boiling is the reason for this behavior. Robinson and Thome [105][122] reported a significant bundle effect for Turbo-BII HP tubes with various refrigerants. It was observed that the bundle effect decreases with increasing reduced pressure and there is an optimal void fraction for an increase in the heat transfer coefficient.

If oil lubricated compressors are used in refrigeration plants, the refrigerant can show an oil contamination. The oil can strongly affect the boiling performance of the tubes. According to Mohrlock et al. [89], following effects might occur when dealing with refrigerant-oil mixtures.

Blocking: Close to the surface, the more volatile component of the mixture, which is the refrigerant, evaporates and the mass fraction of the oil increases. Thus, the wall superheat and the fluid viscosity increase. In reentrant cavities, the oil might lead to clogging of the pores.

Decreasing bubble size: Because of the smaller departure diameter, the area influenced by a nucleation site can be reduced and a higher nucleation site density is possible. With smaller bubbles the convective heat transfer might be reduced.

Foaming: Close to the surface, many small bubbles separated by a thin layer of liquid from the surface can exist. Thin film evaporation can increase the heat transfer in this case but oil might accumulate in the film and with an inhibited flow of fluid towards the wall the heat transfer can also be reduced.

Oil contamination usually deteriorates the performance of a boiling surface and also reduces the improvement factor of an enhanced surface [23][60][61][62][123]. Spindler and Hahne [114] reported a strong decrease of the heat transfer with a GEWA-B tube and R134a-oil mixtures. In their study, the heat transfer can get as low as 20 % of the heat transfer with pure R134a. Kim and Min [62] and Kim and Kim [60] reported a degradation of up to 67 % for a surface similar to Turbo-B and R123a with 5 % oil. When using mixtures, the boiling hysteresis might also get stronger [23][123].

Some authors reported that the degradation gets stronger with rising heat flux [23][61][89]. Mohrlok et al. [89] even observed a decrease of the heat transfer coefficient with rising heat flux. Chen et al. [23] found heat transfer coefficients for enhanced surfaces being lower than heat transfer coefficients for plain surfaces at high heat fluxes. The strong decrease of the heat transfer coefficient at higher heat fluxes is attributed to the immiscibility of the oil once a certain concentration is reached at the surface. Opposed to that, Spindler and Hahne [114] reported that the influence of the oil decreases with rising heat flux. Kim and Min [62] and Kim and Kim [60] reported a decrease of the degradation with rising heat flux and R123a-oil mixtures. They argued that more oil is removed from the subsurface tunnel with rising heat flux.

The degradation increases with pressure [23][60][62][89]. According to Chen et al. [23], the reduction of the heat transfer coefficient with rising heat flux and rising pressure might be due to a decrease in diffusion area because of the larger active nucleation site density, or a decrease in turbulent motion because of the smaller bubbles.

The degradation factor has been reported to be different for different surfaces. It is assumed that bigger openings are better to drive out the less volatile component accumulating at the surface and in the subsurface tunnels [24][60][62][123]. Opposed to that, Zarnescu et al. [142] reported an increase in degradation with decreasing tunnel size but found only little influence of the pore size of a Turbo-B surface with a R134a-oil mixture. They observed that the improvement of heat transfer obtained with a rectangular tunnel base compared to a circular tunnel base is eliminated with the oil mixture. They assume that the reason for this is that the oil in the lower menisci is not removed.

Some authors reported an improvement of the performance with small amounts of oil at high heat fluxes [86][89]. This is attributed to foaming at the boiling surface. Kedzierski [57] found such an improvement also at low heat fluxes and a Turbo-BII HP surface. He explained the results with an increase in active nucleation site density.

In general, boiling of mixtures from enhanced surfaces is currently not sufficiently understood. It should be noted that even if the enhancement factor decreases with refrigerant-oil mixtures, enhanced tubes can still outperform plain tubes significantly.

2.2.3 Modeling of evaporation from subsurface tunnels

With the large number of parameters being present, modeling of evaporation from subsurface tunnels is very challenging. So far, no model is available which comes without the use of empirical parameters.

Webb [127] proposes that there are six main geometrical dimensions describing a boiling surface having pores. These are

- tunnel pitch,
- tunnel height,
- tunnel width,
- tunnel base radius,
- pore diameter,
- pore pitch.

Pores without a circular shape are supposed to be described by the largest circle which can be drawn within the pore [127].

Most effort was put into modeling the suction-evaporation mode, as this is the most effective mode of boiling and tubes with reentrant type structures are usually operated in this regime.

For this mode, Nakayama et al. [94] suggested modeling the heat flux as a sum of the latent heat flux and the sensible heat flux.

$$q = q_{\text{in}} + q_{\text{ex}} \tag{2.1}$$

The latent heat flux q_{in} is dominated by the evaporation from liquid menisci inside the tunnels and the sensible heat flux q_{ex} is caused by convection on the outer surface of the tube. This approach was also used by other authors.

External heat flux

To model the external heat flux q_{ex}, several approaches can be found in literature. Nakayama et al. [94] employed correlation (2.2), which was adapted from a correlation for natural convection published by Zuber [146].

$$q_{\text{ex}} = \left(\frac{\Delta T}{C_{\text{q}}}\right)^{1/C_2} \left(\frac{N_{\text{a}}}{A_{\text{out}}}\right)^{-C_1/C_2} \tag{2.2}$$

The empirical constant C_{q} depends on fluid and pressure. A_{out} is the projected area and $\Delta T = T_{\text{w}} - T_{\text{sat}}$ the wall superheat. Ayub and Bergles [7] followed the approach of Nakayama and employed equation (2.2) with the constants $C_{\text{q}} = 3\,\text{K}(\text{cm}^2/\text{W})^{3/5}(1/\text{cm}^2)^{1/5}$, $C_1 = -1/5$, $C_2 = 3/5$. N_{a}, which is the number of active pores, was taken from experiments. For the tubes used by Ayub and Bergles the number of active pores was curve fitted by Equation (2.3).

$$\begin{aligned} N_\mathrm{a} &= -42.94 + 40.96\,\Delta T - 2.53\,\Delta T^2 \quad \text{for water} \\ N_\mathrm{a} &= -32.13 + 20.25\,\Delta T + 0.85\,\Delta T^2 \quad \text{for R113} \end{aligned} \tag{2.3}$$

Chien and Webb [26] took the model for the external heat flux from Haider and Webb [43]. This model uses the correlation of Mikic and Rohsenow [88] with a correction for the transient convection. The heat flux given by the model of Mikic and Rohsenow considers transient conduction as it occurs when the departing bubble removes the thermal boundary layer in a circular area having twice the diameter of the departing bubble and is replaced by fluid with the temperature T_sat flowing to the wall. Knowing the bubble departure diameter $d_\mathrm{b,dep}$, bubble frequency f, and active pore density n_a together with the liquid thermal conductivity k_l, density ρ_l, and specific heat capacity c_l, the time averaged heat flux is then given by Equation (2.4).

$$q_\mathrm{ex(MR)} = 2\sqrt{\pi k_\mathrm{l} \rho_\mathrm{l} c_\mathrm{l} f}\, d_\mathrm{b,dep}^2 n_\mathrm{a} \Delta T \tag{2.4}$$

This heat flux is corrected to account for transient convection, which is considered to be the more important mechanism of external heat transfer by most authors [43], and is given by Equation (2.5)

$$q_\mathrm{ex} = q_\mathrm{ex(MR)} \left(1 + \left(\frac{0.66\pi C_\mathrm{ex}}{Pr_\mathrm{l}^{1/6}}\right)^2\right)^{1/2} \tag{2.5}$$

The empirical constant $C_\mathrm{ex} = 6.42$ was curve fitted and the correlation predicts data of Nakayama et al. [94] and Chien and Webb [25] for boiling from plain surfaces with an error of ±25 %. With the assumptions that the departing bubbles are spherical and that the bubble departure is governed by a force balance between buoyancy and surface tension forces, the bubble departure diameter is given by Equation (2.6).

$$d_\mathrm{b,dep} = \left(\frac{Bo + \sqrt{Bo^2 + 2304\,(96/Bo - 3)}}{192 - 6\,Bo}\right)^{1/2} d_\mathrm{p} \tag{2.6}$$

In there, $Bo = d_\mathrm{p}^2/a^2$ is the Bond-number based on the pore diameter d_p and the capillary length $a = \sqrt{\sigma/(g(\rho_\mathrm{l} - \rho_\mathrm{v}))}$. The active pore density, which is needed for the calculation of the external heat flux, can be calculated from Equation (2.7), which is derived from an energy and mass balance.

$$n_\mathrm{a} = \frac{q_\mathrm{in}}{\rho_\mathrm{v} \Delta h_\mathrm{v} f\, \pi d_\mathrm{b,dep}^3/6} \tag{2.7}$$

A different approach to calculate the required bubble departure diameter was employed by Ramaswamy et al. [103]. They analyzed the forces acting on the bubble, which are an unsteady growth force F_drag, buoyancy force F_buoy, surface tension force F_σ, lift force (lift produced by the departing bubble on the next bubble) F_lift, bubble inertia force $F_\mathrm{b,i}$, and liquid inertia forces $F_\mathrm{l,i}$. For inertia driven growth, the velocity of the bubble front is assumed to be constant and thus the liquid inertia forces are zero. The bubble departs when Equation (2.8) is fulfilled.

$$F_\mathrm{drag} + F_\sigma + F_\mathrm{b,i} = F_\mathrm{buoy} + F_\mathrm{lift} \tag{2.8}$$

The growth force is the drag of the bubble in the liquid caused by the asymmetrical growth away from the wall. It is calculated according to Zeng et al. [143] using Equation (2.9) with the constant $C_\mathrm{S} = 20/3$.

$$F_\mathrm{drag} = \rho_\mathrm{l} \pi R^2 \left(\frac{3}{2} C_\mathrm{S} \dot{R}^2 + R \ddot{R} \right) \tag{2.9}$$

Buoyancy force is given by Equation (2.10).

$$F_\mathrm{buoy} = \left(\rho_\mathrm{l} - \rho_\mathrm{v} \right) g V_\mathrm{b} \tag{2.10}$$

Surface tension force is taken from [26] and calculated with Equation (2.11).

$$F_\sigma = \sigma \pi d_\mathrm{p} \sin \Theta \tag{2.11}$$

According to Kolev [64], the lift force can be written as in Equation (2.12) with the rise velocity of the flow induced by the bubble u_l and the empirical coefficient C_lift.

$$F_\mathrm{lift} = \frac{\pi}{2} \rho_\mathrm{l} (d_\mathrm{b} u_\mathrm{l})^2 C_\mathrm{lift} \tag{2.12}$$

Equation (2.13) gives the bubble inertia force as suggested by Sharma [107].

$$F_\mathrm{b,i} = m_\mathrm{b} \frac{\mathrm{d}u_\mathrm{b}}{\mathrm{d}\tau} + u_\mathrm{b} \frac{\mathrm{d}m_\mathrm{b}}{\mathrm{d}R_\mathrm{b}} \frac{\mathrm{d}R_\mathrm{b}}{\mathrm{d}\tau} \tag{2.13}$$

In there, mass m_b, velocity u_b, and radius R_b of the bubble are employed. Ramaswamy et al. argued that constant C_ex in Equation (2.5) is not universal as proposed by Chien and Webb but is a function of wall superheat. It is emphasized that the model is only valid for the isolated bubble regime.

Internal heat flux

Models for calculating the internal heat flux presented in literature can roughly be classified in three categories.

Type 1: Empirical modeling of heat transfer, no or empirical modeling of liquid flow into the tunnel.

Type 2: Analysis of heat transfer and evaporation at liquid films, empirical modeling of liquid flow.

Type 3: Analysis of heat transfer and evaporation at liquid films, analysis of liquid flow.

So far, no model is available which is capable of a fully predictive calculation of heat transfer performance of tubes with reentrant type structures. Modeling of Type 1 was presented by Ayub and Bergles [7], Nakayama et al. [94], and Chen et al. [21]. Ayub and Bergles assumed thin film evaporation at the tunnel wall with heat flux being given by Equation (2.14).

$$q_\mathrm{in} = \dot{m} \Delta h_\mathrm{v} = \frac{k_\mathrm{l} A_\delta}{\delta} \Delta T \tag{2.14}$$

A_δ / δ is the ratio of liquid film area and film thickness. As it cannot be measured directly, the value was used as fitting parameter and assumed to be constant for one test fluid. The ratio is assumed to depend strongly on surface tension. Therefore, the value A_δ / δ was extended to other fluids by multiplying it with the ratio of the surface tension of the fluid it was originally determined for and the fluid it is supposed to be extended to.

Nakayama et al. suggested dividing the suction evaporation mode into three phases, which are the pressure build-up, pressure reduction, and liquid intake phase. General relations for pressure of the vapor and the liquid, bubble growth, and evaporation of the liquid in the tunnel were given for the three phases and fitted with several empirical parameters to experimental results. The split into three phases as suggested by Nakayama et al. was adopted by other authors. Chen et al. [21] introduced a statistical distribution of the pore size. By applying the mass conservation law to liquid and vapor in the tunnel, bubble diameter, bubble frequency, and active pore density are calculated. The assumption of bubbles growing with constant departure diameter and one growth velocity simultaneously at several pores, as it was used by Nakayama et al. [94] and Chien and Webb [26], is not required. Chen et al. employ a semi-empirical correlation to model heat transfer.

Chien and Webb [26], Ramaswamy et al. [103], and Das et al. [31] presented models of Type 2. Chien and Webb were the first to relate heat transfer at the liquid meniscus to the size of the meniscus depicted in Figure 2.12 and calculated the growth and shrinking of the liquid film in the tunnel with time.

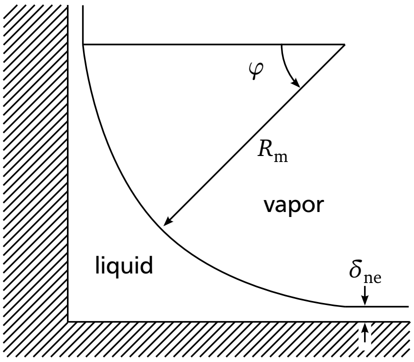

Figure 2.12: Meniscus in tunnel corner according to Chien and Webb [26]

Heat transfer is calculated by a step wise integration over the liquid film and time, leading to Equation (2.15).

$$Q_{\mathrm{tun}} = \int_0^{1/f} \Delta T \left(2\,LN_{\mathrm{m}} \int_0^{\pi/4} \frac{k_{\mathrm{l}}}{\left[R_{\mathrm{m}}(\tau)+\delta_{\mathrm{ne}}(\tau)\right]1/\cos(\varphi)-R_{\mathrm{m}}(\tau)} R_{\mathrm{m}}(\tau)\,\mathrm{d}\varphi \right) \mathrm{d}\tau \tag{2.15}$$

L represents the tunnel length and N_{m} the number of menisci in each tunnel. The temperature difference can only be evaluated outside of the integral if the wall superheat is rather small. If the radius becomes small, the increase in required superheat because of disjoining and capillary pressure has to be considered. With the dispersion constant A the temperature difference in this case is given by Equation (2.16).

$$\Delta T = T_{\mathrm{w}} - T_{\mathrm{sat}}(p_{\mathrm{v}}) \left(1 + \frac{\sigma/R_{\mathrm{m}} + A/\delta^3}{\Delta h_{\mathrm{v}}\rho_{\mathrm{l}}}\right) \tag{2.16}$$

The non-evaporating film thickness δ_{ne} is given by Equation (2.17).

$$\delta_{\mathrm{ne}} = \left(\frac{AT_{\mathrm{sat}}}{\rho_{\mathrm{l}}\Delta h_{\mathrm{v}}(T_{\mathrm{w}} - T_{\mathrm{sat}})}\right)^{1/3} \tag{2.17}$$

The amount of liquid flowing into the tunnel during the liquid intake phase is calculated with an empirical correlation. Das et al. [31] argued that the duration of the liquid intake phase should not be neglected for the sake of completeness of the model. The liquid intake time is modeled for active as well as inactive pores and the larger time is supposed to be considered for calculating the bubble frequency. The results showed that with fluid R11 the liquid intake time is at least two orders of magnitude smaller than growth or waiting time. Consequently, the intake time might only be significant for low gravity conditions or depressurized systems.

Jiang et al. [52] presented a sophisticated model of Type 3, in which the tunnel and the liquid film is discretized in several elements. A simplified set of conservation equations is derived for the elements. They model the mass flow of vapor and liquid from inactive pores towards active pores, assuming one dimensional flow in direction of the tunnel and heat transfer from liquid menisci in the tunnel corners. The set of equations is solved numerically with a finite difference method. The model predicts the number of active pores and bubble frequency.

The presented models show a strong dependence on bubble departure diameter. In the formulation of Mikic and Rohsenow, the external heat flux is proportional to the bubble diameter squared and for internal heat flux the bubble departure diameter limits the duration of the bubble growth period. Therefore, modeling of bubble departure limits the accuracy of the models. Chen and Groll [20] pointed out that the assumption of a spherical bubble can lead to wrong dynamic forces. Even if the bubble is spherical, dynamic forces can not always be neglected. Only very small spherical bubbles are governed by surface tension only. The influence of buoyancy depends on the growth stage. Generally, there are many publications on the dynamics of bubble growth and detachment and the results are diverging quite a bit. For example Buyevich and Webbon [18] stated that surface tension is not necessarily responsible for impeding bubble detachment, which was assumed by most authors.

Ramaswamy et al. showed that the heat transfer model of Chien and Webb is sensitive to the dispersion constant, which is also difficult to determine. For all models, calculation of liquid flow through the pores to the film is empirical, which reflects the lack of knowledge of the details of this process.

Up to now, there is no full model being able to predict which boiling mode is obtained.

2.3 Numerical simulations of boiling phenomena

As time scales as well as length scales are very small in boiling processes, the possibilities to gain insight by measurements are limited. Numerical simulations theoretically do not have limitations in resolving time and space and offer a promising method for studying boiling phenomena. In practice, simulations are limited by the availability of computational power, solution procedures, and models for complicated physical phenomena like nucleation or the influence of surfactants. Computational power and solution procedures have developed rapidly in the last decade. Comparisons with analytical solutions and experimental results show that bubble dynamics, phase change at the liquid-vapor interface, and evaporation at the three phase contact line can be depicted quite well. Nevertheless, the accuracy of numerical results always depends on the knowledge of the boundary conditions and fluid properties, which have to be determined by measurements. A comprehensive review on suitable methods for simulating multiphase flows in microfluidics was given by Wörner [139]. Reviews on numerical simulations of boiling processes and phase change were given by Dhir et al. [32] or Stephan et al. [116].

2.3.1 Methods

First, some of the numerical methods which were developed in the last decades and are used today are introduced. The focus is on procedures which aim at simulations on the scale of single bubbles. In there, the liquid-vapor interface is resolved and its movement is part of the solution unlike in Euler-Euler or Euler-Lagrange methods. For most problems, Mach numbers are small such that the flow can be treated as incompressible, while the Reynolds numbers are too high for inertia to be neglected. Furthermore, even if the scales can become very small in some problems, the fluid can typically be treated as a continuum.

Capturing of the liquid-vapor interface used to be one of the challenging features in multiphase numerical codes. For this task front capturing methods are most commonly used today. In the Volume-of-fluid method **VOF** of Hirt and Nichols [47], an additional variable is introduced indicating the phase of the fluid, which is transported by convection with the flow. For a divergence free flow field, the transport equation for the field indicator variable F is consequently given by Equation (2.18).

$$\frac{\partial F}{\partial \tau} + \nabla \cdot (\mathbf{u}F) = 0 \tag{2.18}$$

Field values of $F = 1$ indicate phase one, field values of $F = 0$ phase two. A cell with a value between $0 < F < 1$ contains a piece of interface. In VOF methods with interface reconstruction, a geometrical representation of the interface is calculated, which can be piecewise constant (e.g. SLIC), piecewise linear (PLIC) or piecewise parabolic (PPIC). For those methods, the convection of the interface is performed with a geometrical advection scheme.

The reconstruction of the interface, especially in 3D and on unstructured grids, can be very challenging. Therefore, in many codes the VOF method is employed without geometrical advection, but the convection equation is solved with differencing schemes. Here, the challenge is finding a scheme which is stable, bounded, and prevents diffusion of the interface. VOF methods are inherently mass conservative if employed with a finite volume discretization.

An approach to capture the interface which is commonly employed with finite difference or finite element discretization, is the Level-set method **LS** of Sussman et al. [119]. In there, a signed distance scalar function, which becomes zero at the interface, is employed to indicate the interface. Reinitialization of the distance field and additional correction steps are required to enforce mass conservation.

Among the front tracking methods, the Marker-and-cell method **MAC** was employed by Welch et al. [129] to simulate multiphase flows. Here, a Lagrangian formulation is used to follow markers which define a certain phase.

The Front-tracking method **FT** of Unverdi and Tryggvason [124] employs surface markers at the interface. In order to be able to simulate bubble or droplet merger, special methods are required.

It is also possible to use a moving mesh to indicate the location of the interface. The **ALE** formulation of Hirt [46] with a finite element discretization is most common in this context.

Lattice Boltzmann methods **LB**, which do not solve the Navier-Stokes equations, are also employed to simulate multiphase flows on small scales. In there, the interaction of fluid particles is calculated. Compared to the Navier-Stokes equations, the Lattice Boltzmann equations are easier to implement and to solve, but assigning macroscopic fluid properties like viscosity or density is not straight forward.

Similar to the VOF method an indicator variable is employed with the Phase-field method **PF**, resulting in an interface spanning across several cells. But opposed to VOF, the finite interface thickness here is physically motivated and calculated with the chemical potential of the fluid. As a consequence, an extremely fine mesh is required in the vicinity of the interface.

In addition to the methods mentioned above, there exist numerous hybrid methods such as HPLS [36] or CLSVOF [118] for which the reader is referred to the literature.

In order to be able to simulate multiphase flows, the effect of surface tension needs to be incorporated in the Navier-Stokes equation. Widely spread is the continuous surface force method CSF of Brackbill et al. [15]. The curvature is calculated by the divergence of the normal vectors of the interface. Alternative approaches are the continuous surface stress method CSS of Lafaurie at al. [72] or an adaption of a ghost fluid method by Liu et al. [78]. Any method to incorporate the effect of surface tension has to deal with spurious currents. These are artificial flows in the vicinity of the interface which are created if surface tension forces and pressure forces are not completely balanced or curvature is calculated inaccurately. In the case of phase change, the parasitic currents can increase the heat transfer towards the interface. There exist numerous methods to reduce spurious currents for different discretization methods and interface representations. For an evaluation of some of the methods see Fuster et al. [37].

Numerical simulations of phase change require the mass and momentum equation to account for the change in normal velocity at the liquid-vapor interface. Consequently, the flow field is not divergence free in this case. The energy equation needs to be solved to obtain the evaporation rate. Several authors presented evaporation models working with different representations of the liquid-vapor interface. Welch [130] presented an evaporation model for a moving mesh method and Welch and Wilson [131] for a VOF method with interface reconstruction. Son and Dhir [111] employed the Level-set method to simulate phase change. The Level-set method was combined with a ghost fluid method by Gibou [40] to accurately determine phase change rates. Juric and Tryggvason [55] introduced an evaporation model for the Front-tracking method with a finite difference discretization. Jamet et al. [51] combined the Phase-field method with an evaporation model to simulate phase change. Yoon et al. [141] used a mesh free method to simulate nucleate boiling. Hardt and Wondra [44] introduced a relaxation model to calculate phase change, which works independently of the employed interface capturing method.

Processes on the scale of single bubbles or droplets can strongly be influenced by effects occurring on much smaller scales, which typically cannot be incorporated in the numerical simulation. In order to deal with this problem, subgrid scale models are introduced which model the processes on the small scales and couple them with the flow simulation. As examples for such subgrid models, Wörner [139] names thin film models or models for the species-concentration in the boundary layer in mass transfer [6]. In heat transfer, so called contact line or microlayer models based on the work of Wayner et al. [126] or Cooper and Lloyd [30] are of special interest. Stephan and Busse [115] were among the first to combine Wayners model of evaporation at the three phase contact line with the simulation of macroscopic fluid flow and phase change. The modeling of the microlayer of Cooper and Lloyd was applied by Lee and Nydahl [73] for the simulation of bubble growth. More details on modeling of evaporation in the vicinity of the three phase contact line is given in Section 3.4.

Multiphase flows including a liquid-vapor interface interacting with a solid wall require the specification of a contact angle. As the prediction of contact angles is difficult, the value often has to be taken from experiments. With moving contact lines, dynamic contact angles can be observed which depend on the speed and direction of the movement. While it is generally advised to employ dynamic contact angles in simulations, the laws describing the dependence of contact angle on the movement are under discussion. The numerical representation of contact angles is straight forward with the CSF method of Brackbill et al., as only the direction of the interface normal at the boundary needs to be adjusted. In VOF methods, the movement of the three phase contact line poses no special difficulties, while in other interface representations, slip or diffusion have to be applied to overcome the apparent singularity at the three phase contact line at a wall with no-slip boundary condition. A review on numerical simulations with moving contact lines was given by Sui et al. [117].

2.3.2 Numerical simulations of boiling from plain surfaces

Numerous studies have been performed to investigate fluid flow and heat transfer of bubbles growing at a plane wall. The physical effects which have to be considered for boiling of a pure fluid from a plain surface, include nucleation, heat and fluid flow in liquid and vapor, phase change at the liquid-vapor interface, evaporation of thin films at the bubble foot, thermal response of the heating surface, and interface dynamics like contact line motion, bubble departure and interaction. By today it is possible to incorporate most of those effects in a boiling simulation. Unfortunately, one of the key elements of many boiling processes is heterogeneous nucleation, for which only very basic modeling approaches were employed so far.

Most authors initially set a bubble nucleus into a superheated thermal boundary layer and thus avoid the stage of nucleation. In this case, for a fixed wall superheat the thickness and temperature profile of the thermal boundary layer needs to be specified. If the heat flux at the wall is provided, additionally the wall temperature is required. Son et al. [112] determined the initial thickness of the thermal boundary layer from a correlation for turbulent natural convective heat transfer, resulting in Equation (2.19).

$$\delta_{\mathrm{th}} = 7.14 \left(\frac{\nu_{\mathrm{l}} k_{\mathrm{l}}}{g \beta \Delta T \rho_{\mathrm{l}} c_{\mathrm{l}}} \right)^{1/3} \tag{2.19}$$

Kunkelmann and Stephan [70] simulated subsequent bubble cycles to obtain the temperature and thickness of the thermal boundary layer. The waiting time between the bubbles was taken from experimental observations. Aktinol and Dhir [4] coupled the setting of a new bubble nucleus to the local wall superheat. Once a certain wall superheat was exceeded, a new bubble nucleus was set. The required superheat was chosen based on the studies of Wang and Dhir [125]. A similar approach was chosen by Li et al. [77]. Dietl and Stephan [35] performed boiling simulations from single reentrant cavities. As the reentrant cavities are holding vapor also after bubble departure, subsequent bubble cycles were simulated to obtain the thermal boundary layer without the need of supplying a waiting period.

With numerical simulations it has been possible to confirm experimental observations and obtain additional information about the boiling process. The strong influence of thin film evaporation at the foot of the bubble was observed by several authors. Son and Dhir [112] reported that 20 % of the wall heat transfer was transferred through the contact line region during a bubble cycle with water at atmospheric pressure. They employed a Level-set method to capture the interface. The wall was taken to be isothermal with various wall superheats being simulated. Kunkelmann et al. [68] studied the influence of contact line speed on the evaporation in the vicinity of the three phase contact line. They employed the VOF method in OpenFOAM. Fluid properties were those of FC-72 and the gravity level was reduced to allow a comparison with experiments performed at parabolic flight campaigns. They found the heat transfer at the three phase contact line being much higher with advancing contact line than with receding contact line. With the wall underneath the bubble being isolated by vapor, it is heating up until the bubble foot starts to shrink. Furthermore, with an advancing contact line, next to the contact line a vortex carries cold fluid from the bulk towards the wall. Therefore, temperature differences are higher with an advancing contact line than with a receding one during nucleate boiling and the heat transfer rate is increased. The amount of the heat transferred through the contact line in relation to the total heat transfer was found to be approximately constant during all phases of bubble growth and independent of contact line speed.

Other effects studied with the help of numerical simulations include the influence of subcooling [10][137][138], gravity [10][99][145], contact angle [1][91], or properties of the wall [4][81][144].

With rising heat flux, bubbles start to interact during nucleate boiling. To study the effects of bubble interaction, simulations were performed with bubbles merging vertically and laterally. Vertical bubble merger were studied by Son et al. [113]. They could not observe any influence of the bubble merger on heat flux.

Simulations of lateral bubble merger require the full three dimensional simulation of at least one half of one bubble and are computationally demanding. Kunkelmann and Stephan [69] performed simulations of a lateral bubble merger. They were able to demonstrate the development of a residual droplet during the merging process, which was also observed experimentally for HFE-7100. Studies of lateral bubble merger were also conducted by Abarajith et al. [2] and Mukherjee and Dhir [90]. Bubble merger with two and three bubbles were performed with the model introduced by Son and Dhir [112]. The arrangement of the bubbles was varied and asymmetrical merger were simulated as well to investigate temperatures and bubble dynamics.

2.3.3 Numerical simulations of boiling from structured surfaces

First simulations for boiling from a reenrant cavity were performed by Wondra and Stephan [135]. They employed the VOF method in Fluent together with the evaporation model of Hardt and Wondra [44]. Simulations were performed with a 2D translational domain and without model for evaporation at the three phase contact line, allowing only qualitative observations of the bubble detachment and film evaporation process.

Numerical simulations of boiling from cavities with different shapes were performed by Lee and Son [74]. A Level-set method was used to convect the liquid-vapor interface, as well as to identify the solid-fluid interface. The cavities studied include a cylindrical cavity, a cylindrical cavity with two steps and a cylindrical cavity surrounded by a ring shaped cavity. In an additional paper Lee et al. [75] also studied a circular cavity surrounded by a fin. The geometries are illustrated in Figure 2.13. The common characteristic of the surface structures is that they can be calculated with an axisymmetric computational domain.

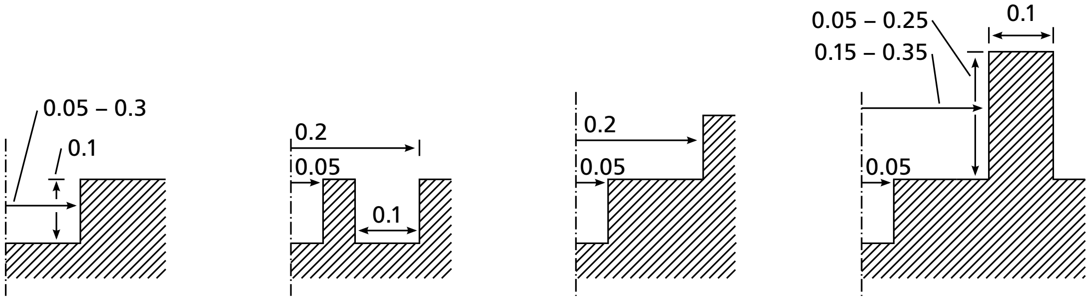

Circular cavity

Cavity with groove

Multi step cavity

Cavity with fin

Figure 2.13: Cavity shapes employed by Lee and Son [74] and Lee et al. [75], dimensions in 10^{-3}m

It was shown that heat transfer increases with the cylindrical cavities because the contact line length increases. Additional steps in the cavity lead to further enhancement of the heat transfer. Surrounding the cavity with a ring shaped groove reduces the heat transfer because the contact line pins at the boundary of the groove and the bubble foot is not growing further. For the cavity surrounded by a fin, gravity was increased to obtain smaller bubbles. The optimal fin spacing was found to be about 0.6 times the bubble departure diameter and heat transfer could be increased by 40 % to 60 % compared to a plain surface.

2.4 Summary of the state of the art and scope of this work

Reentrant type structured surfaces are state of the art in enhancing pool boiling heat transfer. Through thermal measurements and visualization studies several processes occurring at reentrant cavities could be identified and models were created to describe the effects. Up to now, processes occurring inside single reentrant cavities could not be observed and their effect on heat transfer thus not determined.

At subsurface tunnels connected through pores with the pool, boiling modes could be identified on which current modeling approaches and developments are based. The knowledge about the processes inside the tunnel originate from visualization studies, as local measurements are extremely difficult due to the small time and length scales. Therefore, the characteristics of the liquid flow into the tunnel and the influence of single geometric properties on the process are under discussion.

In the last years, numerical methods became powerful enough to simulate the boiling process on the scale of a single bubble qualitatively and quantitatively correctly. Computational cluster allow the simulation of bubble interaction and boiling processes in 3D. Hence, direct numerical simulations were identified as promising method to gain insight into processes in pool boiling in a level of detail which is beyond the capabilities of measurement techniques.

In this work, a state of the art numerical CFD code is applied to study the processes occurring within the cavities of reentrant type surfaces. Different designs of single reentrant cavities are considered and the sensitivity of the results on single numerical and process parameters is investigated. In order to study the processes occurring with subsurface tunnels, boiling from a tunnel section containing two pores is simulated on the “Lichtenberg” high performance computer at TU Darmstadt. Fluid properties were selected to be those of R134a at $T_{\mathrm{sat}} = 20\,^{\circ}\mathrm{C}$, as a large number of studies have been performed with this refrigerant. With the CFD simulations, the following key questions are addressed:

- is it possible to have evaporating liquid films inside single cavities as observed with subsurface tunnels,
- which parameters govern liquid flow inside and into the subsurface tunnel,
- which conditions are leading to dryout and flooding of the subsurface tunnel.

The processes at the pores are analyzed and the transfer of the results to realistic surface structures is discussed. Thus, the transition between the boiling modes introduced by Nakayama et al. can be described in further detail. As current models lack the prediction of the boiling mode, a novel modeling approach is suggested in this work and the effects that are required to be accounted for in an exhaustive heat transfer model are given.

3 Numerical Model

The numerical model is based on the work of Kunkelmann and Stephan [70] and Herbert et al. [45]. Most parts of the model are comprehensively described in the theses of Kunkelmann [67] and Batzdorf [11]. Minor modifications are performed to improve stability and convergence and an additional anti-diffusion method is introduced. The model is implemented into the open source toolbox OpenFOAM, established by Weller et al. [132], employing the finite volume method. The solver is based on the Volume-of-fluid method of Hirt and Nichols [47] to capture the liquid-vapor interface and is coupled to a subgrid scale model for heat transfer in the vicinity of the three phase contact line. An interface reconstruction method allows determining the position of the contact line and the temperature gradient at the interface. Calculation of conjugate heat transfer is possible. The model employs the dynamic mesh capabilities of OpenFOAM and is fully parallelized.

3.1 Conservation laws in continuum mechanics

The fluid flow can be described with the balance equations for mass, momentum, and energy. With the assumptions that

- the fluid properties are continuous,
- the fluid flow is incompressible,
- the fluid is Newtonian,
- the work of the pressure and the viscous dissipation can be neglected,

the conservation laws are given in their differential form by Equations (3.1) to (3.3).

$$\nabla \cdot \mathbf{u} = \frac{\dot{\rho}}{\rho} \tag{3.1}$$

$$\rho \left(\frac{\partial \mathbf{u}}{\partial \tau} + (\mathbf{u} \cdot \nabla)\mathbf{u} \right) = \mathbf{f} - \nabla p + \nabla \left(-\frac{2}{3}\mu \nabla \cdot \mathbf{u} \right) + \nabla \cdot \left(\mu \left(\nabla \mathbf{u} + (\nabla \mathbf{u})^{\mathrm{T}} \right) \right) \tag{3.2}$$

$$\rho c \left(\frac{\partial T}{\partial \tau} + \mathbf{u} \cdot \nabla T \right) - \nabla \cdot (k \nabla T) = \dot{h} \tag{3.3}$$

The right hand side in Equation (3.1) and (3.3) account for mass and energy sources due to evaporation, which are modeled as described in Section 3.3. The force **f** in Equation (3.2) accounts for gravity and surface tension. Surface tension and contact angle treatment is discussed in Section 3.2. In the solid region, the energy equation simplifies to Equation (3.4).

$$\frac{\partial \left(\rho c T \right)}{\partial \tau} = \nabla \cdot (k \nabla T) \tag{3.4}$$

For multiphase flow, conservation of mass has to be fulfilled for each phase. The VOF method of Hirt and Nichols [47] uses an indicator variable F to identify liquid and vapor regions. In OpenFOAM, Equation (3.5) is solved with the MULES scheme for the transport of the VOF variable.

$$\frac{\partial F}{\partial \tau} + \nabla \cdot (\mathbf{u} F) + \nabla \cdot \left(\mathbf{u}_{\mathrm{r}} F (1 - F) \right) = \frac{\dot{\rho}}{\rho} F \tag{3.5}$$

The VOF variable F is bounded between zero and one, giving the volume fraction of liquid in a numerical cell. In order to prevent numerical diffusion of the field, a compression term acting at the interface is employed in OpenFOAM. The compression parameter $\mathbf{u}_\mathrm{r}$ in Equation (3.5) scales with the flow velocity and an user set parameter and points normal towards the interface. On the right hand side of Equation (3.5), the source term accounts for phase change.

The physical properties of the fluid are given by linear averaging of the liquid property χ_l and the vapor property χ_v as shown in Equation (3.6).

$$\chi = F\chi_\mathrm{l} + (1-F)\,\chi_\mathrm{v} \tag{3.6}$$

The fluid properties are assumed to be constant and independent of the local fluid temperature.

The conservation equations are discretized with the finite volume method employing the libraries of OpenFOAM. As the flow is assumed to be incompressible, energy and momentum equation are solved separately. The momentum equation is solved with the PISO algorithm [50].

3.2 Capturing of the interface

As mentioned before, the liquid-vapor interface is captured by the Volume-of-fluid (VOF) method. In OpenFOAM, the VOF Equation (3.5) is solved explicitly with a flux limiter, to keep the field bounded. With the VOF method in OpenFOAM, there is no sharp interface but the interface is located within the cells with $0 < F < 1$. In order to be able to obtain an exact position of the contact line and the interface, Kunkelmann and Stephan [70] implemented a geometric interface reconstruction, which is also employed in this work. Figure 3.1 illustrates the steps of the reconstruction.

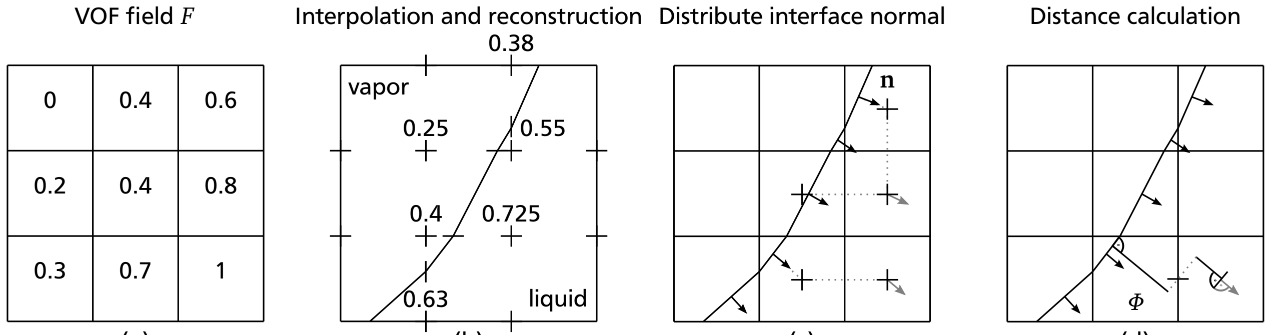

(a) (b) (c) (d)

Figure 3.1: Interface reconstruction method

To reconstruct the interface

- the VOF variable F is interpolated from the cell centers to the cell points (Figure 3.1 (b)),
- the point with the value $F = 0.5$ is located on the edges of the cells by interpolation,
- the interface is piecewise approximated with planes through those points,
- the interface normal $\mathbf{n}$ and interface area A_int are calculated within each cell,
- the interface normal and area of the interface in the cell are distributed away from the interface and the distance field Φ is calculated (Figure 3.1 (c) and (d)),
- the normal $\mathbf{n}$ on the boundaries is corrected to account for the contact angle boundary condition,
- the curvature of the interface is calculated and smoothed.

The reconstructed interface is continuous, but opposed to interface reconstruction methods like SLIC or PLIC not mass conserving. Therefore, it cannot be used to reset the VOF field and prevent numerical diffusion. It has turned out to be beneficial to employ the interface normal from the reconstruction instead of the gradient of the VOF field for the orientation of the compression vector $\mathbf{u}_r$ in Equation (3.5) and for curvature calculation. In order to do so, the information needs to be distributed from the cells containing the reconstructed interface to all cells with field values $0 < F < 1$.

To be able to calculate the gradient of the temperature field close to the interface, the distance of the neighboring cell centers in normal direction to the reconstructed interface is required. The calculation is performed together with the distribution of the interface normal, as illustrated in Figure 3.1 (d). First, the normal distance of the interface to the face centers of the cell is determined. From there the distance of the next cell center is calculated with the interface normal that was distributed to the face center.

At the boundary the interface normal needs to be corrected to account for contact angle or symmetry boundary conditions. On wall boundaries, the boundary value of the VOF variable is adjusted such that the gradient of the VOF field matches the contact angle at the boundary. This requires the VOF variable to be unbounded on the wall, which is without consequence as long as the flux caused by the product of curvature with the gradient of the VOF field is enforced to be zero on the wall.

To make sure that the capillary pressure is influenced correctly by the applied contact angle at the wall, it is beneficial to delete the normal of the interface in the first cell layer next to the boundary before the normal is distributed to neighboring cells. This can lead to problems if the contact angle is very small or only a thin layer of liquid exists at the wall. In this case, the interface normal is not pointing in normal direction of the interface anymore, which can lead to strong diffusion of the VOF field and an inaccurate calculation of the distance field. Therefore, close to contact angle boundary conditions, two sets of interface normals are created and employed for different purposes as illustrated in Figure 3.2.

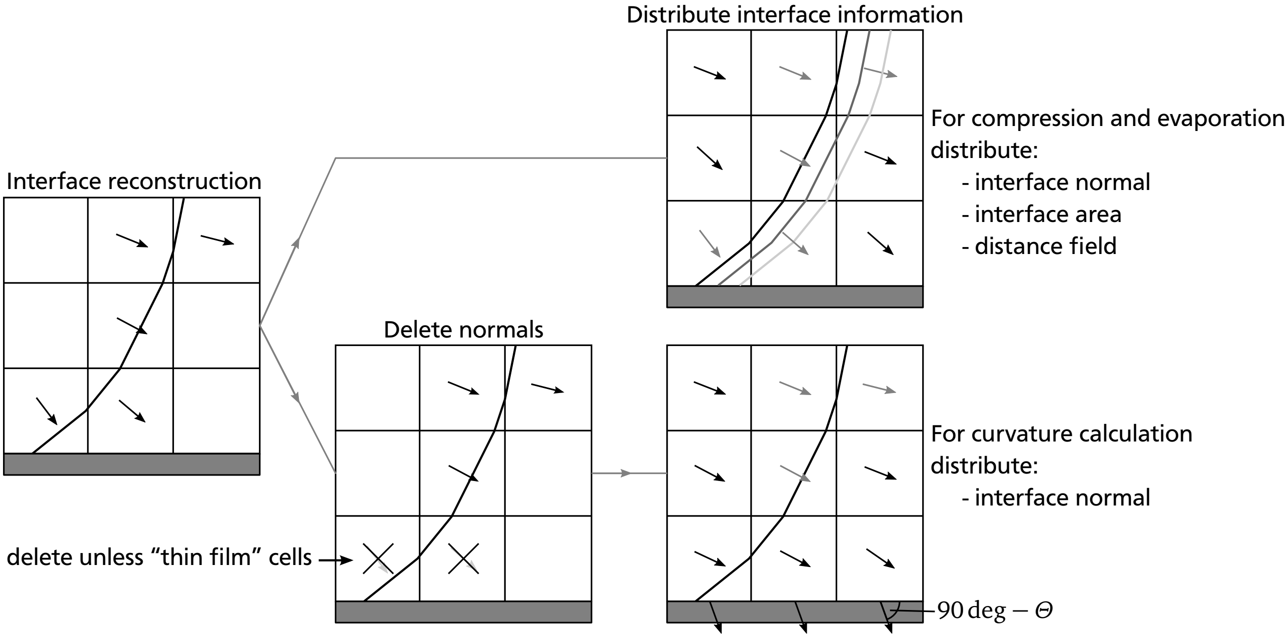

Figure 3.2: Boundary treatment with interface reconstruction

The interface normals are distributed and employed without alterations for the compression of the liquid-vapor interface and for calculation of the distance field, which is required to determine the evaporation rate. For calculation of curvature, the interface normals in the first cell layer at the wall are deleted before the interface normals are distributed. In order to calculate the curvature, the normals are interpolated to the cell faces. On the wall faces, the interface normals are corrected according to the contact angle boundary condition. The curvature of the interface is then calculated by taking the divergence $\kappa = \nabla \cdot \mathbf{n}$

of the interface normal vector field **n**. To reduce spurious currents at the interface, the curvature is smoothed first, then spread, and then smoothed again. With the curvature κ, the surface tension force is calculated according to the method of Brackbill et al. [15].

If the liquid-vapor interface lies within the first cell layer at the wall for several cells, as illustrated in Figure 3.3, and the interface normal is deleted, the information of the interface orientation is lost.

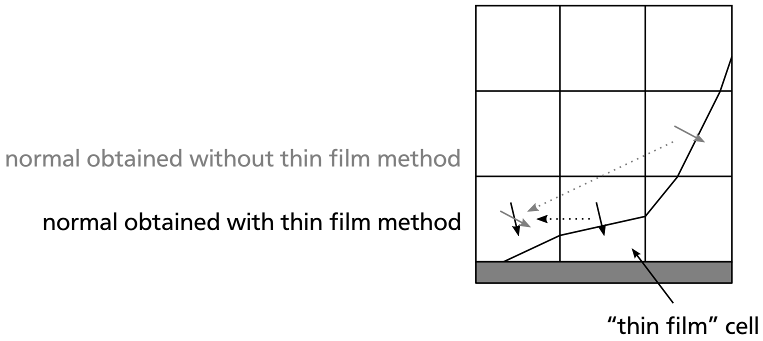

Figure 3.3: Thin film correction

Instead, the cells obtain the interface normal from a piece of interface which can be several cells away and can have quite a different orientation. In this case, the curvature is calculated based on the difference between contact angle and interface normal of the cell further away from the contact line. In order to be able to include the interface orientation of such cells while keeping the influence of contact angle on the capillary pressure high, so called "thin film" cells are defined. Within a "thin film" cell, the interface normal is not deleted. A cell is defined as "thin film" cell if all the following conditions apply:

- one face of the cell lies on a wall boundary
- the cell contains a piece of interface
- no contact line is detected on the wall face of the cell
- all neighboring boundary cells contain a piece of reconstructed interface

With this method it is possible to perform calculations with small contact angles and a strongly curved interface on rather coarse grids.

3.3 Modeling of evaporation

To account for phase change, modeling of the source terms in the conservation equations is required. Based on the work of Hardt and Wondra [44] and Kunkelmann and Stephan [70], Batzdorf et al. [12] presented the implicit formulation of the phase change model which employed in this work. With the implicit formulation, temperature undershots below saturation temperature can be prevented, which the explicit method of Kunkelmann and Stephan suffers from.

In the evaporation model, the liquid-vapor interface is assumed to be at saturation temperature and the heat flow towards the interface is taken from the local temperature gradient. For an accurate calculation of the temperature gradient, the distance and the temperature value from the cells adjacent to the interface cells are employed. The source terms are then calculated in the cells the temperature for calculating the gradient is taken from. In summary, the following steps are performed:

- distribution of the interface area to the cells on the liquid and the vapor side
- calculation of the temperature gradient based on the distance field
- calculation of mass and enthalpy sources and sinks with the distributed interface area
- smearing of the mass source term field

- rescaling the source field to obtain the correct evaporation rate

The interface area is required to be transferred to neighboring cells until a cell without liquid-vapor interface is reached. The area A_{int} of the interface in each cell is copied to both, the liquid region and the vapor region to obtain $A_{\mathrm{int,l}}$ and $A_{\mathrm{int,v}}$ while assuring that for the integral over the computational domain Ω the relation $\iiint A_{\mathrm{int}}\,\mathrm{d}\Omega = \iiint A_{\mathrm{int,l}}\,\mathrm{d}\Omega = \iiint A_{\mathrm{int,v}}\,\mathrm{d}\Omega$ holds true. To prevent conductive heat transfer across the interface, the conductivity at the cell faces of the cells containing the original interface is set to zero.

The source terms for mass $\dot{\rho}$ and enthalpy $\dot{h}$ are given by Equation (3.7) and Equation (3.8) respectively. The mass source $\dot{\rho}_{\mathrm{cl}}$, originating from evaporation at the three phase contact line, is added directly to the mass source term in the cell containing the contact line.

$$\dot{\rho} = \left(A_{\mathrm{int,l}} + A_{\mathrm{int,v}}\right) \frac{k\left(T_{\mathrm{cell}} - T_{\mathrm{sat}}\right)}{V_{\mathrm{cell}}|\Phi|\Delta h_{\mathrm{v}}} + \dot{\rho}_{\mathrm{cl}} \tag{3.7}$$

$$\dot{h} = \dot{\rho}\Delta h_{\mathrm{v}} \tag{3.8}$$

The smearing of the mass sources is performed according to the method of Hardt and Wondra [44], as large local mass sources can lead to problems when solving the conservation equations. To distribute the source term field, the diffusion equation (3.9) is solved, where an appropriate length scale $\Delta\Psi$ is usually on the order of a couple cell sizes and $\psi_0 = \dot{\rho}$. The local error caused by the smearing of the source field was given by Hardt and Wondra to be on the order of $\Delta\Psi\kappa/2$.

$$\nabla^2\psi = \frac{1}{(\Delta\Psi)^2}\left(\psi - \psi_0\right) \tag{3.9}$$

The field ψ is rescaled such that the integral over ψ in the liquid region equals the integral over ψ in the vapor region and the integral over ψ_0. For the evaporating case, mass sinks are set in the liquid region and sources in the vapor region according to the distribution of ψ. Hardt and Wondra show that with this method it is also possible to depict the pressure recoil at the interface, which is caused by the required acceleration of the molecules when they move from the region of high density on the liquid side to the region of low density on the vapor side of the interface.

If the local density $\rho = F\rho_{\mathrm{l}} + (1-F)\rho_{\mathrm{v}}$ is employed on the right hand side of the continuity equation (3.1) for $\dot{\rho}/\rho$, no mass sources can be set in the interface region without changing the evaporating mass. This can be avoided by employing either the liquid density ρ_{l} or the vapor density ρ_{v}, depending on which side of the interface the sources are located. The same applies to Equation (3.5), where additionally the value of F in the term $F\dot{\rho}/\rho$ has to be set to one or zero depending on the location of the source.

3.4 Evaporation in the vicinity of the three phase contact line

In pool boiling, processes occurring at the foot of the bubble can have a strong influence on the heat transfer and bubble dynamics. Two major effects are discussed in literature, which are the evaporation in the vicinity of the apparent three phase contact line and the formation of a liquid microlayer with a thickness of several micrometers below the bubble [58]. Sielaff and Stephan [110] observed that a liquid microlayer is more likely to form with a receding contact line and a large spreading rate of the vapor, while evaporation in the vicinity of the three phase contact line occurs with low contact line velocities or an advancing contact line. Within this work, contact lines are either pinned or the velocities are very small. Therefore, it is assumed that an apparent three phase contact line forms where the liquid-vapor interface approaches the wall. Close to the contact line, a thin liquid film results in a low thermal resistance leading to a high heat flux. The concept of evaporating thin films in the vicinity of the three phase contact line was introduced by Wayner et al. [126]. During pool boiling up to 30 % of the heat can be transferred in this region [116].

The processes occurring in the vicinity of the three phase contact line typically cannot be resolved in a boiling simulation. In the following, the region in which the apparent contact angle is formed is named the microzone. Figure 3.4 shows a sketch of the microzone.

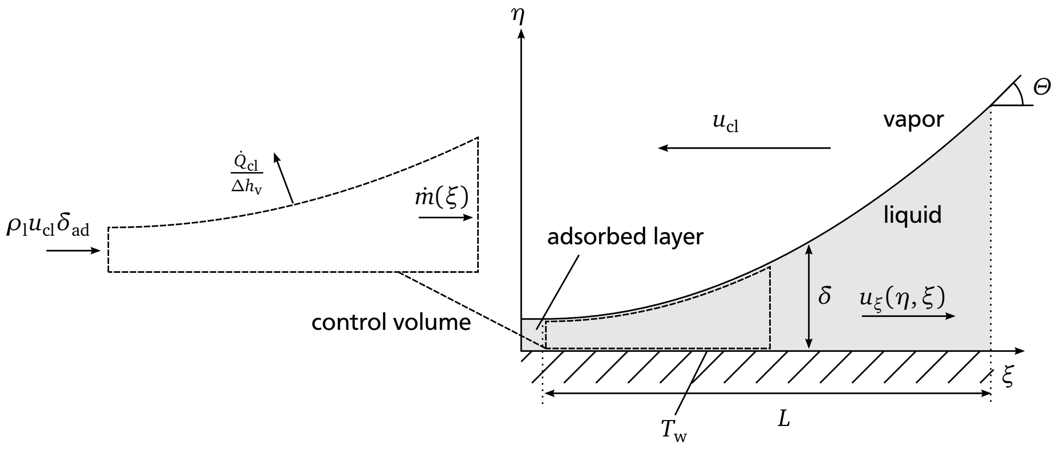

Figure 3.4: Microzone region with control volume

Below the vapor, an adsorbed layer of fluid molecules is located, which is hindered from evaporation by Van-der-Waals forces acting between solid and fluid molecules. From there on, at the apparent three phase contact line, the slope of the liquid-vapor interface rapidly increases and attains the macroscopic contact angle Θ.

The model employed for evaporation in the microzone was derived by Stephan and Busse [115] and extended by Herbert et al. [45] for a moving contact line.

To simplify the governing equations in the microzone, first, a dimensional analysis of the processes is performed, leading to the conclusions that

- the liquid layer is thin and Reynolds number is small (lubrication approximation),
- the wall temperature within the microzone is uniform,
- heat transfer is one-dimensional.

Furthermore, due to the small thermal inertia of the system, the microzone is taken to be at steady state.

Pressure difference at the liquid-vapor interface

The difference between the pressure of the vapor p_{v} and the pressure of the liquid p_{l} in the microzone can be calculated as in Equation (3.10). The difference is caused by the curvature of the interface κ and the difference in momentum resulting from the different molecule velocities $u_{\mathrm{n,l}}$ and $u_{\mathrm{n,v}}$ normal to the interface.

$$\Delta p_{\mathrm{v,l}} = p_{\mathrm{v}} - p_{\mathrm{l}} \left(\eta = \delta \right) = \sigma \kappa + \rho_{\mathrm{l}} u_{\mathrm{n,l}}^2 - \rho_{\mathrm{v}} u_{\mathrm{n,v}}^2 \tag{3.10}$$

For two dimensions, the curvature κ can be expressed as a function of the first and second derivative of the film thickness δ as shown in Equation (3.11).

$$\kappa = \frac{\delta''}{\left(1+\delta'^2\right)^{1.5}} \tag{3.11}$$

Molecularkinetic thermal resistance at the interface

On molecular level, the temperature of the liquid-vapor interface T_{int} needs to be above the local equilibrium temperature T_{sat} for phase change to occur. The required temperature difference can be calculated with a thermal resistance R_{int}, defined in Equation (3.12).

$$R_{\mathrm{int}} = \frac{T_{\mathrm{int}} - T_{\mathrm{sat}}}{q_{\mathrm{int}}} \tag{3.12}$$

This thermal resistance is very small and can be neglected with the thermal boundary layer that is typically obtained at the liquid-vapor interface in the bulk fluid. But with the thickness of the liquid film in the microzone approaching the thickness of the adsorbed layer, the molecularkinetic thermal resistance can be of the same order as the thermal resistance of the liquid film. Under the assumptions that

- the vapor is at saturation temperature,
- the vapor can be treated as ideal gas,
- the vapor density is much lower than the liquid density,
- the vapor consists of a single component,
- the velocity of the vapor molecules is much lower than the local speed of sound,

Schrage [106] analyzed the net mass flux at the liquid-vapor interface from which Equation (3.13) can be deduced.

$$R_{\mathrm{int}} = \frac{2-f}{2f}\,\frac{T_{\mathrm{sat}}\sqrt{2\pi R_{\mathrm{gas}} T_{\mathrm{sat}}}}{\Delta h_{\mathrm{v}}^2 \rho_{\mathrm{v}}} \tag{3.13}$$

The evaporation coefficient f is in the range of 0 to 1. The influence of f on the results is discussed in Section 3.4. In this work, the ideal gas constant is obtained from the ideal gas law $R_{\mathrm{gas}} = p_{\mathrm{sat}}/(\rho_{\mathrm{v}} T_{\mathrm{sat}})$.

Balance study

Within the microzone, conservation of mass, momentum, and energy applies. One of the major assumptions for the microzone region is that the liquid film thickness is small compared to the length of the microzone $\delta \ll L$. With the thickness of the liquid film being small, the flow can be assumed to be creeping with $Re \rightarrow 0$. Furthermore, the mechanical and thermal inertia within the microzone are very small compared to the inertia of the surroundings so the equations can be solved for a system in steady state. Heat and fluid flow is modeled in a reference frame moving with the velocity of the contact line u_{cl}. Consequently, the momentum equation in ξ-direction is given by Equation (3.14)

$$\frac{\partial p_{\mathrm{l}}}{\partial \xi} = \rho_{\mathrm{l}} \nu_{\mathrm{l}} \frac{\partial^2 u_\xi}{\partial \eta^2} \tag{3.14}$$

and the momentum equation in η-direction by Equation (3.15).

$$\frac{\partial p_{\mathrm{l}}}{\partial \eta} = \frac{\partial}{\partial \eta}\left(\frac{A}{\eta^3}\right) \tag{3.15}$$

Applying a mass balance for the control volume shown in Figure 3.4, Equation (3.16) is obtained.

$$0 = \dot{m}(\xi) + \frac{\dot{Q}_{\mathrm{cl}}}{\Delta h_{\mathrm{v}}} - \rho_{\mathrm{l}} u_{\mathrm{cl}} \delta_{\mathrm{ad}} \tag{3.16}$$

In there, the assumption is employed that the change in kinetic energy is small compared to the enthalpy of evaporation and that the vapor temperature is constant [19]. $\dot{Q}_{\mathrm{cl}}$ is the integrated heat flow from $\xi = 0$ to ξ. The mass flow $\dot{m}(\xi)$ is given by Equation (3.17).

$$\dot{m}(\xi) = \int_0^{\delta} \rho_{\mathrm{l}} u_{\xi} \, \mathrm{d}\eta \tag{3.17}$$

Integration of the momentum equation (3.15) in η leads to Equation (3.18) for the liquid pressure.

$$p_{\mathrm{l}}(\xi, \eta) = \frac{A}{\eta^3} + C(\xi, \eta) \tag{3.18}$$

With the boundary condition $p_{\mathrm{l}}(\eta = \delta)$ given by Equation (3.10), this results in Equation (3.19).

$$p_{\mathrm{l}}(\xi, \eta) = p_{\mathrm{v}}(\xi) - \Delta p_{\mathrm{v,l}} - \frac{A}{\delta^3} + \frac{A}{\eta^3} \tag{3.19}$$

The definition of an augmented capillary pressure p_{cap}, given by Equation (3.20), simplifies the equations in the following.

$$p_{\mathrm{cap}} = \Delta p_{\mathrm{v,l}} + \frac{A}{\delta^3} \tag{3.20}$$

A is the so-called dispersion constant. Technically, assuming a constant value for the dispersion constant is only valid up to a distance of about 5 nm of the molecules to the wall. For larger distances, the term predicts an adhesion pressure which is too large, but with rising film thickness δ the value of term $\sigma\kappa$ becomes much larger than the value of A/δ^3. Therefore, this modeling error is insignificant. The dispersion constant for a fluid interacting through vacuum with a solid was given by Israelachvili [49] as in Equation (3.21).

$$A = \sqrt{A_{\mathrm{ss}} A_{\mathrm{ff}}} \tag{3.21}$$

In there, A_{ss} is the dispersion constant of the solid interacting with solid molecules and A_{ff} the dispersion constant of the fluid interacting with fluid molecules. In this work, the dispersion constants are selected to be $A_{\mathrm{ff}} = 4/(6\pi) \cdot 10^{-20}$ and $A_{\mathrm{ss}} = 40/(6\pi) \cdot 10^{-20}$, resulting in $A \approx 13/(6\pi) \cdot 10^{-20}$. The influence of the dispersion constant on the results is discussed in Section 3.4.

Taking the derivative in ξ of Equation (3.19) one obtains Equation (3.22), where the term $\mathrm{d}p_{\mathrm{v}}/\mathrm{d}\xi$ can be neglected, as it is much smaller than the variation of the augmented capillary pressure in ξ-direction.

$$\frac{\partial p_{\mathrm{l}}}{\partial \xi} = \frac{\mathrm{d}p_{\mathrm{v}}}{\mathrm{d}\xi} - \frac{\mathrm{d}p_{\mathrm{cap}}}{\mathrm{d}\xi} \tag{3.22}$$

Integrating the momentum equation (3.14) in ξ-direction twice leads to Equation (3.23) for the velocity.

$$u_\xi = \frac{1}{\nu_l \rho_l} \frac{\partial p_l}{\partial \xi} \frac{\eta^2}{2} + C_1 \eta + C_2 \tag{3.23}$$

With the boundary conditions $u_\xi(\eta = 0) = u_{cl}$ and $(\partial u_\xi / \partial \eta)\big|_{\eta=\delta} = 0$, the constants C_1 and C_2 can be eliminated and Equation (3.24) is obtained.

$$u_\xi = -\frac{1}{\nu_l \rho_l} \left(\left(\frac{\mathrm{d}p_{cap}}{\mathrm{d}\xi} \right) \left(\frac{\eta^2}{2} - \eta\delta \right) \right) + u_{cl} \tag{3.24}$$

The formulation for the velocity u_ξ can be integrated in Equation (3.17) and together with Equation (3.16) Equation (3.25) is obtained for the augmented capillary pressure.

$$\frac{\mathrm{d}p_{cap}}{\mathrm{d}\xi} = -\frac{3\,\nu_l}{\delta^3 \Delta h_v} \left(\dot{Q}_{cl} + \rho_l \Delta h_v u_{cl} (\delta - \delta_{ad}) \right) \tag{3.25}$$

With heat transfer being one-dimensional, the heat flux at the wall is given by Equation (3.26).

$$q_{cl} = \frac{k_l}{\delta} \left(T_w - T_{int} \right) \tag{3.26}$$

The heat flux at the liquid-vapor interface can be calculated with the interfacial thermal resistance as shown in Equation (3.27). The term in brackets accounts for the increase of equilibrium temperature due to the pressure jump across the interface and the adhesion pressure.

$$q_{int} = \frac{T_{int} - T_{sat}\left(1 + \frac{p_{cap}}{\Delta h_v \rho_l}\right)}{R_{int}} \tag{3.27}$$

The energy balance in the microzone gives $\dot{Q}_{cl} = \dot{Q}_{int}$ and with the difference between wall and interface area this results in Equation (3.28).

$$q_{cl} = q_{int} \sqrt{1 + \delta'^2} \tag{3.28}$$

Combining Equations (3.26), (3.27), and (3.28), the temperature at the interface T_{int} and the heat flux at the interface q_{int} can be eliminated and Equation (3.29) for the heat flux at the wall is obtained.

$$q_{cl} = \frac{\mathrm{d}\dot{Q}_{cl}}{\mathrm{d}\xi} = \frac{T_w - T_{sat}\left(1 + \frac{p_{cap}}{\Delta h_v \rho_l}\right)}{\frac{\delta}{k_l} + \frac{R_{int}}{\sqrt{1+\delta'^2}}} \tag{3.29}$$

System of equations and solution procedure

The full rearranged system of equations (3.30) is given below.

$$
\begin{aligned}
\frac{\mathrm{d}\delta}{\mathrm{d}\xi} &= \delta' \\
\frac{\mathrm{d}\delta'}{\mathrm{d}\xi} &= \frac{\left(1+\delta'^2\right)^{1.5}}{\sigma}\left(p_{\mathrm{cap}} - \frac{A}{\delta^3} + \frac{1}{\Delta h_{\mathrm{v}}^2}\left(\frac{T_{\mathrm{w}} - T_{\mathrm{sat}}\left(1+\frac{p_{\mathrm{cap}}}{\Delta h_{\mathrm{v}}\rho_{\mathrm{l}}}\right)}{\sqrt{1+\delta'^2}\,\frac{\delta}{k_{\mathrm{l}}} + R_{\mathrm{int}}}\right)^2\left(\frac{1}{\rho_{\mathrm{v}}} - \frac{1}{\rho_{\mathrm{l}}}\right)\right) \\
\frac{\mathrm{d}p_{\mathrm{cap}}}{\mathrm{d}\xi} &= -\frac{3\,\nu_{\mathrm{l}}}{\delta^3\Delta h_{\mathrm{v}}}\left(\dot{Q}_{\mathrm{cl}} + \rho_{\mathrm{l}}\Delta h_{\mathrm{v}} u_{\mathrm{cl}}(\delta - \delta_{\mathrm{ad}})\right) \\
\frac{\mathrm{d}\dot{Q}_{\mathrm{cl}}}{\mathrm{d}\xi} &= \frac{T_{\mathrm{w}} - T_{\mathrm{sat}}\left(1+\frac{p_{\mathrm{cap}}}{\Delta h_{\mathrm{v}}\rho_{\mathrm{l}}}\right)}{\frac{\delta}{k_{\mathrm{l}}} + \frac{R_{\mathrm{int}}}{\sqrt{1+\delta'^2}}}
\end{aligned}
\qquad (3.30)
$$

The boundaries of the contact line region are the adsorbed film at $\xi = 0$ and the macro region at $\xi = \xi_{\mathrm{end}}$. At the adsorbed film, the thickness of the liquid film is given by $\delta_{\mathrm{ad}} = \left(A/p_{\mathrm{cap}}(\xi = 0)\right)^{1/3}$. The augmented capillary pressure can be calculated with the condition $q_{\mathrm{cl}} = 0$ from Equation (3.29) to be $p_{\mathrm{cap}}(\xi = 0) = \left(T_{\mathrm{w}}/T_{\mathrm{sat}} - 1\right)\Delta h_{\mathrm{v}}\rho_{\mathrm{l}}$.

The system of equations is solved employing a shooting method. Technically, both, the gradient of the film thickness δ' and the integrated heat flow $\dot{Q}_{\mathrm{cl}}$, are zero at the adsorbed film. In order to not obtain the trivial solution, the film thickness as well as the integrated heat flow are perturbed at the beginning of the microzone. As the magnitude of the variables in SI units is spanning over several orders, the system of equations is solved in non-dimensional form to reduce errors.

The integration of the equations is performed along ξ until the curvature of the liquid-vapor interface is small and the thermal resistance of the liquid film determines the evaporation rate. In order to be able to couple the solution of the equations with the flow solver, the integration is performed up to a fixed value of $\xi_{\mathrm{end}} = 0.5\,\mu\mathrm{m}$, where this is the case for all parameter combinations employed in this work.

The system of equations is solved for a set of wall superheats and contact line velocities. The resulting heat flow, contact angle, and liquid film thickness are curve fitted to be employed in the CFD simulation.

Sensitivity of the solution on input parameters

The microzone model requires the input of fluid properties which are difficult to obtain or can only be estimated. Furthermore, the artificial perturbation at the beginning of the microzone to not obtain the trivial solution can have an effect on the overall solution as well. To evaluate the potential error introduced by the uncertainty of the input parameters, a small sensitivity study is performed. The reference solution is given by the solution of the microzone model for a steady contact line with a wall superheat of $\Delta T = 1\,\mathrm{K}$ and fluid properties of R134a at $T_{\mathrm{sat}} = 20\,^{\circ}\mathrm{C}$. Fluid properties are given in Appendix A. The results for a variation of the dispersion constant A and the evaporation coefficient f are given in Table 3.1. As the microzone region is taken to be 2D, the heat flow $\dot{Q}_{\mathrm{cl}}$ is given in W/m(contact line) here. The influence of the evaporation coefficient on the heat transfer in the microzone region and contact angle is rather strong. Marek and Straub [82] point out that generally the coefficient is higher for dynamically renewing surfaces, as they appear for example in a jet, than for a quasi-static surface like that of a meniscus. Furthermore, values are lower for water than for non-polar substances. For most

Table 3.1: Sensitivity of model results on evaporation coefficient f and dispersion constant A

f	A in 10^{-21} J	$\dot{Q}_{\mathrm{cl}}$ in W/m	$\delta\left(\xi_{\mathrm{end}}\right)$ in 10^{-7} m	Θ in deg
0.2	6.9	0.54	0.89	13.47
0.4	6.9	0.76	1.14	16.01
0.6	6.9	0.89	1.29	17.40
0.8	6.9	0.98	1.41	18.51
1	6.9	1.05	1.51	19.43
1	0.69	0.86	1.88	22.01
1	3.45	0.98	1.64	20.32
1	6.9	1.05	1.51	19.43
1	13.8	1.14	1.35	18.42
1	69	1.47	0.89	14.79

systems, the exact evaporation coefficient is unknown. If contact angle and surface temperature data is available from the experiment, f can be adjusted such that the experimentally determined contact angle is obtained. In this work, the value is set to $f = 0.8$. The sensitivity of the overall results of the CFD simulation on the evaporation coefficient is studied in Section 4.1.5.

The sensitivity of the model results on the dispersion constant is considerably lower than on the evaporation coefficient. Dividing the value for A in half has about the same effect as decreasing the evaporation coefficient by 0.2. As long as the order of magnitude of A is predicted correctly, the error should be below the error introduced through the uncertainty of f.

The initial film thickness for the integration needs to be larger than the thickness of the adsorbed film $\delta(\xi = 0) > \delta_{\mathrm{ad}}$. The influence of the initial film thickness is given in Table 3.2.

Table 3.2: Sensitivity of model results on initial film thickness $\delta\,(\xi = 0)$

$\delta\,(\xi = 0)$	$\dot{Q}_{\mathrm{cl}}$ in W/m	$\delta\left(\xi_{\mathrm{end}}\right)$ in 10^{-7} m	Θ in deg
$1.0001\,\delta_{\mathrm{ad}}$	1.01	1.26	19.08
$1.001\,\delta_{\mathrm{ad}}$	1.03	1.38	19.16
$1.01\,\delta_{\mathrm{ad}}$	1.05	1.51	19.43
$1.1\,\delta_{\mathrm{ad}}$	1.10	1.74	20.46
$2\,\delta_{\mathrm{ad}}$	2.99	3.30	34.01

As long as the initial film thickness is well below $1.1\,\delta_{\mathrm{ad}}$, the influence on the results is small. In this work an initial film thickness of $1.01\,\delta_{\mathrm{ad}}$ is employed.

3.5 Conjugate heat transfer and coupling of the subgrid scale model

Conjugate heat transfer is simulated by looping over the solution of the temperature equation in the liquid and the solid region and adapting the boundary conditions for each loop. If a three phase contact line exists at the fluid-solid interface, the microzone model is coupled to the flow solver by adjusting the boundary conditions in the temperature equation in the fluid and the solid for each loop. The procedure is illustrated in Figure 3.5.

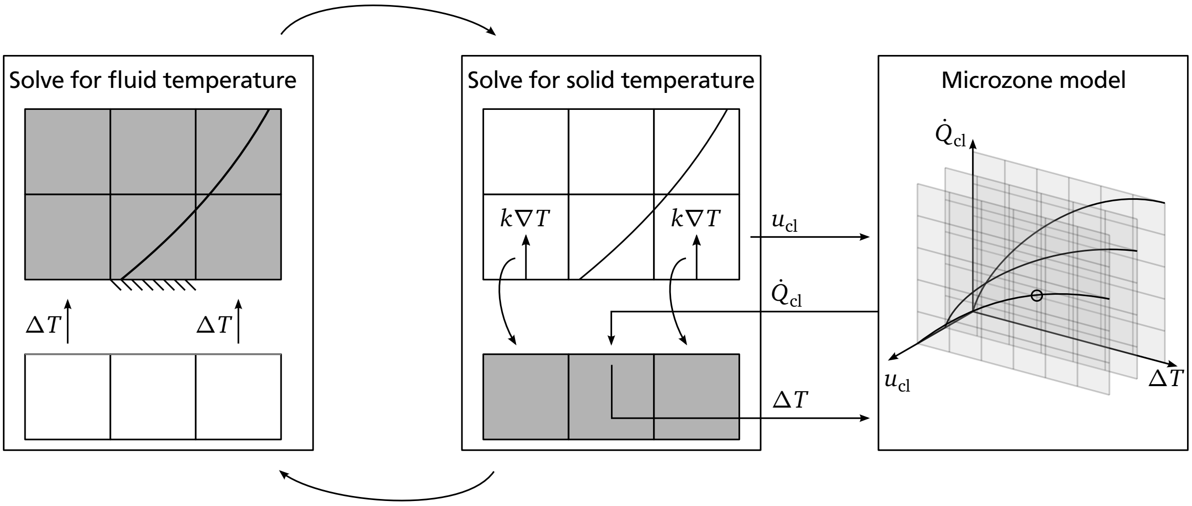

Figure 3.5: Calculation of conjugate heat transfer with three phase contact line

The position, length, and velocity of the contact line can be taken from the reconstructed interface. First, the temperature in the fluid region is solved for with a fixed temperature boundary condition at the fluid-solid interface. Additionally, the cell containing the contact line is taken to be adiabatic towards the wall. The wall superheat at this adiabatic face together with the contact line velocity are employed to obtain the heat transfer calculated by the microzone model. To solve for the temperature in the solid region, the temperature gradient at the boundary in the fluid region is calculated. With this, the heat flux can be calculated and set as boundary condition on the solid side. For the face in the solid region matching the face with the contact line in the fluid region, the heat flux is taken directly from the contact line model. The solution of the temperature equation in the solid gives the wall superheat at the fluid-solid interface, which is used to update the boundary condition in the fluid region.

For the cell with the contact line in the fluid region, several heat flows across the faces have to be considered. The cell and the treatment of the heat flow is depicted in Figure 3.6.

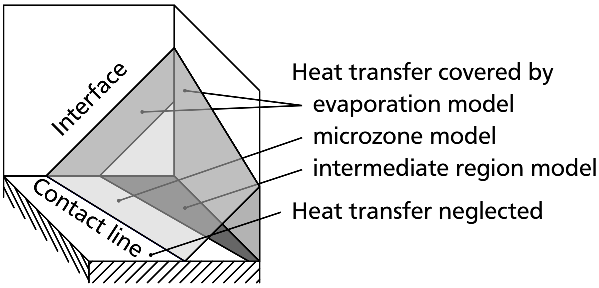

Figure 3.6: Heat transfer towards the interface in the cell containing the contact line

Heat which is transferred parallel to the wall towards the interface from neighboring cells is accounted for by the evaporation model. The heat transferred to the interface normal to wall is calculated in the microzone model, but only up to a distance of 0.5µm from the reconstructed contact line. This leaves an area depicted in Figure 3.6 as “intermediate region”, from which heat transfer towards the interface needs to be calculated as well and added to the heat transfer through the microzone region.

As the thermal conductivity in the vapor is low compared to the conductivity in the liquid, heat transfer on the vapor side of the liquid-vapor interface is neglected in this cell. In the intermediate region, the interface is assumed to be a plane starting at the end of the microzone region. The plane is calculated with the height of the liquid film at the end of the microzone region and an inclination angle given by the contact angle. For this plane, heat flux is given by Equation (3.31), where the thermal resistance of the interface R_{int} is usually much smaller than δ/k_{l}. In the intermediate region, influence of recoil and adhesion pressure as well as curvature on the equilibrium temperature are neglected.

$$q = \frac{T_{\mathrm{w}} - T_{\mathrm{sat}}}{\frac{\delta}{k_{\mathrm{l}}} + \frac{R_{\mathrm{int}}}{\cos\Theta}} \tag{3.31}$$

In the flow solver, the integrated heat flux given by the integral of Equation (3.31) over the intermediate region is required. By splitting the integral, an analytical solution for each linear segment of the boundary of the intermediate region can be calculated and the summation gives the required heat flow value. For the case that the interface passes through an additional cell at the boundary before extending further into the domain, the “intermediate region” calculation is extended to the cell next to the cell containing the contact line. Details on this procedure are given in [11].

3.6 Treatment of numerical diffusion

Under some circumstances, flow patterns together with small contact angles and capillary driven flows can lead to an increase in numerical diffusion, which cannot be handled by the compression term in the VOF equation. Especially at sharp corners, when a pinned contact line is supposed to move around the corner in order to satisfy the contact angle boundary condition, pieces of the VOF field making up the liquid can detach from the liquid and move with the vapor stream. Figure 3.7 shows the undesired movement of liquid at the corner on a coarse grid.

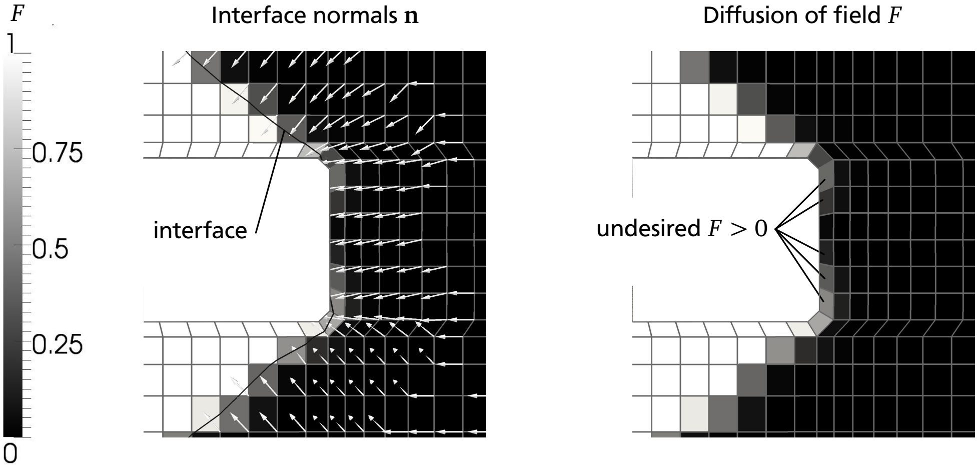

Figure 3.7: Diffusion of the VOF field at a corner of the wall boundary

Due to the interface position at the corner, the interface normals point in normal direction to the wall and the compression cannot push the liquid back towards the fluid region. Usually the flow is not affected much by such detachments as the removed liquid mass is very small. But if such a detached liquid field hits a wall, calculation of heat transfer can be strongly altered as an additional contact line might be created leading to a high local heat transfer coefficient. Therefore, a new method is implemented moving the detached liquid field back to the original liquid-vapor interface, without affecting the movement of the interface. The method is robust, fast, and global mass and energy conserving. The interface region is discretized in small overlapping volumes, in which the algorithm is applied. Within these operation ranges, fluid mass and enthalpy is conserved. The procedure is illustrated for a two-dimensional problem in Figure 3.8, the extension to three dimensions is straight forward. In the illustration, the removal of liquid from vapor cells is depicted. In the numerical model, the algorithm is applied in the same manner to also remove vapor from liquid cells.

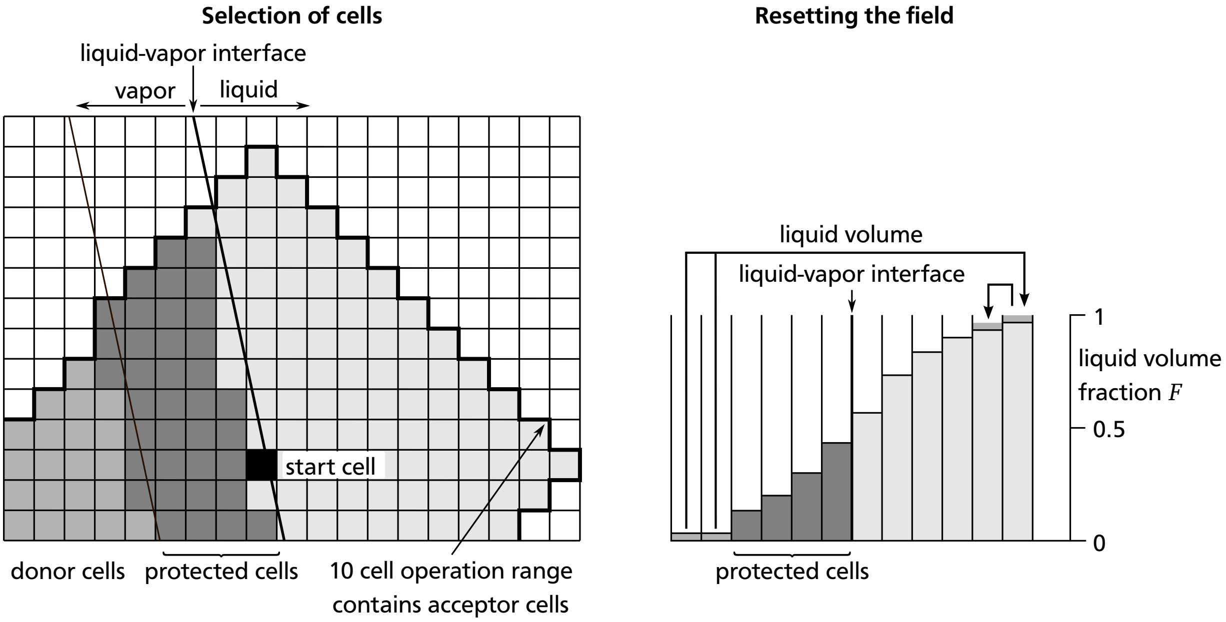

Figure 3.8: Illustration of anti-diffusion method

The algorithm starts at a random interface cell. From this cell, neighboring cells up to a distance of ten cells are selected to form the operation range. In the vapor region, cells up to a distance of four times the cell size from the interface are protected, which means that no liquid mass is removed from those cells. For cells being in the vapor region and not protected, the liquid volume and the removed enthalpy is integrated according to Equation (3.32) and Equation (3.33).

$$V_\mathrm{l} = \sum_{\text{donor cells}} V_\mathrm{cell} F \tag{3.32}$$

$$H_\mathrm{l} = \sum_{\text{donor cells}} V_\mathrm{cell} F \left(\rho_\mathrm{l} c_\mathrm{l} - \rho_\mathrm{v} c_\mathrm{v}\right) T \tag{3.33}$$

Starting with the cell being the furthest away from the liquid-vapor interface, the liquid volume is then moved to the liquid side. Cell by cell, the volume fraction of the cells at the liquid side is increased to $F = 1$ and the added liquid volume subtracted from V_l until the vapor volume of the next cell exceeds the remaining liquid volume $V_\mathrm{l,res}$. In this case, the increase of F is given by Equation (3.34).

$$F_\mathrm{new} = F_\mathrm{old} + \frac{V_\mathrm{l,res}}{V_\mathrm{cell}} \tag{3.34}$$

By removing liquid volume fraction F from vapor cells, additional vapor volume is created. The same amount of vapor is removed from liquid cells, once F is increased there. The same procedure is repeated, detecting vapor in liquid cells outside a protected band of cells and moving the vapor to the vapor side.

In order to conserve enthalpy, the temperature of the cells with liquid being added is altered as given in Equation (3.35).

$$T_\mathrm{new} = \frac{F_\mathrm{new} - F_\mathrm{old}}{F_\mathrm{new}\left(\rho_\mathrm{l} c_\mathrm{l} - \rho_\mathrm{v} c_\mathrm{v}\right) + \rho_\mathrm{v} c_\mathrm{v}} \frac{H_\mathrm{l}}{V_\mathrm{l}} + \frac{F_\mathrm{old}\left(\rho_\mathrm{l} c_\mathrm{l} - \rho_\mathrm{v} c_\mathrm{v}\right) + \rho_\mathrm{v} c_\mathrm{v}}{F_\mathrm{new}\left(\rho_\mathrm{l} c_\mathrm{l} - \rho_\mathrm{v} c_\mathrm{v}\right) + \rho_\mathrm{v} c_\mathrm{v}} T_\mathrm{old} \tag{3.35}$$

The temperature of the cells on the vapor side is kept constant. Correcting the temperature in those cells to conserve enthalpy could drastically increase the temperature there, as the thermal capacity strongly decreases with the removal of liquid volume fraction.

Every third cell of the liquid-vapor interface is selected as start cell to form an operation range. By this, the operation ranges overlap, ensuring that the liquid from the vapor cells is moved as far into the liquid range as possible.

Due to the protected area, which is introduced to allow a sufficiently smooth transition of F from liquid to vapor cells, it is possible that small droplets are created, which detach from the bulk fluid. This is the case if the diffusing fields carry enough volume fraction to actually create a reconstructed liquid-vapor interface. Nevertheless, the occurrence of such droplets is strongly reduced.

3.7 Validation

The original solver by Kunkelmann and Stephan was validated with the sucking interface problem, spherical bubble growth, and an evaporating meniscus in a capillary groove. Furthermore, experiments with single bubbles were compared with numerical simulations and the data are in good agreement. Herbert et al. [45] compared numerical simulations of droplet impingement with experiments and found an excellent agreement concerning heat transfer and droplet dynamics. The implicit formulation of the evaporation model is validated in [11].

In this work, the solver is applied to evaporating capillary flows in subsurface tunnels and cavities. Therefore, the ability of the solver to capture capillary driven flows in principle is validated with the experimental results for a capillary rise of Yamamoto et al. [140]. The properties of the fluid and of the tube are given in Table 3.3.

Table 3.3: Properties of fluids and capillary tube

Fluid	Liquid	Gas	Tube	
Density ρ	$1115\,\mathrm{kg/m^3}$	$1.205\,\mathrm{kg/m^3}$	Radius R_t	$0.57 \cdot 10^{-3}\,\mathrm{m}$
Dynamic viscosity μ	$2.081 \cdot 10^{-2}\,\mathrm{Pa\,s}$	$1.822 \cdot 10^{-5}\,\mathrm{Pa\,s}$	Initial height	$5 \cdot 10^{-3}\,\mathrm{m}$
Surface tension σ	$4.86 \cdot 10^{-2}\,\mathrm{N/m}$		Contact angle Θ	72.3 deg

The initial height of the liquid column in the tube is the height of the fluid reservoir surrounding the tube. This value is required to correctly incorporate viscous flow in the tube. Simulations are performed on an axisymmetric grid with two mesh resolutions, as well as a three dimensional grid with half a tube modeled. With the coarse mesh, cell sizes are approximately $\Delta x \approx 59\,\mu\mathrm{m}$. With the fine mesh, the resolution is doubled. Table 3.4 gives the final height of the liquid column for the different meshes.

Table 3.4: Mesh convergence in 2D and 3D

Mesh	2D coarse	2D fine	3D coarse	3D fine
Final height	$3.612 \cdot 10^{-3}\,\mathrm{m}$	$3.635 \cdot 10^{-3}\,\mathrm{m}$	$3.725 \cdot 10^{-3}\,\mathrm{m}$	$3.717 \cdot 10^{-3}\,\mathrm{m}$

In two dimensions as well as in three dimensions, the difference in rising height for the two meshes is below the size of one cell. With the 3D mesh, the liquid rises slightly higher than with the 2D mesh at the same mesh resolution.

The static contact angle provided in Table 3.3 is employed in the simulation. In the experiment a dynamic contact angle is observed during the capillary rise such that differences in the dynamics can be expected. Therefore, the solution of the analytical description of a capillary rise with static contact angle by Bosanquet [14] is given as well. The evolution of the height y_l of the liquid column is given by Bosanquet as in Equation (3.36).

$$\pi R_\mathrm{t}^2 \rho_\mathrm{l} \left(y_\mathrm{l} \ddot{y}_\mathrm{l} + \dot{y}_\mathrm{l}^2 + g y_\mathrm{l} \right) + 8\pi \mu_\mathrm{l} y_\mathrm{l} \dot{y}_\mathrm{l} = 2\pi R_\mathrm{t} \sigma \cos\Theta \tag{3.36}$$

The equation is solved taking into account the gas column located above the liquid column in the tube as well. Figure 3.9 shows the evolution of the height of the liquid column with the CFD results of the fine meshes.

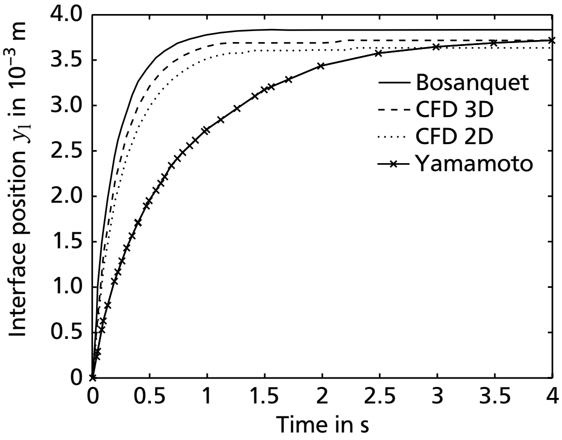

Figure 3.9: Capillary rise in circular tube

Compared to the solution of Equation (3.36), the rise of the liquid column is slightly slower and the final rising height is lower with the CFD. The simulation in three dimensions performs slightly better than the simulation in two dimensions. In the experiment, the capillary rise is much slower due to the dynamic contact angle. Evidently, for a dynamic movement of the liquid driven by capillary forces, the largest error comes from not considering the dynamic contact angle and not from numerical difficulties.

In the numerical simulations of boiling from subsurface tunnels, contact angles and solid structures are smaller than in the reference case of Yamamoto et al. [140]. How well the solver is able to predict the pressure jump with a small contact angle in a complex capillary structure is discussed in Section 5.1.3.

4 Numerical Simulations of Boiling from Single Reentrant Cavities

In this chapter, setup, procedure, and results of numerical simulations at single reentrant cavities are presented. The common characteristic of those geometries is a single cavity in a horizontal boiling surface, which is connected with the liquid pool through a pore of smaller dimension than the cavity. Such surfaces were tested as boiling surfaces for chip cooling and are also in use for creating specific nucleation sites for single bubble experiments. The aim of the simulations is to study processes occurring within the cavities and their effect on bubble dynamics and heat transfer. Especially, it is of interest if similar processes occurring with subsurface tunnels can be observed with single reentrant cavities.

4.1 Setup and procedure

Setup and procedure together with some of the results presented below were published earlier in [34] and [35]. The studies are extended here and evaluated combining the earlier presented with the recently obtained results.

4.1.1 Geometries

Simulations are performed with three main classes of geometries depicted in Figure 4.1.

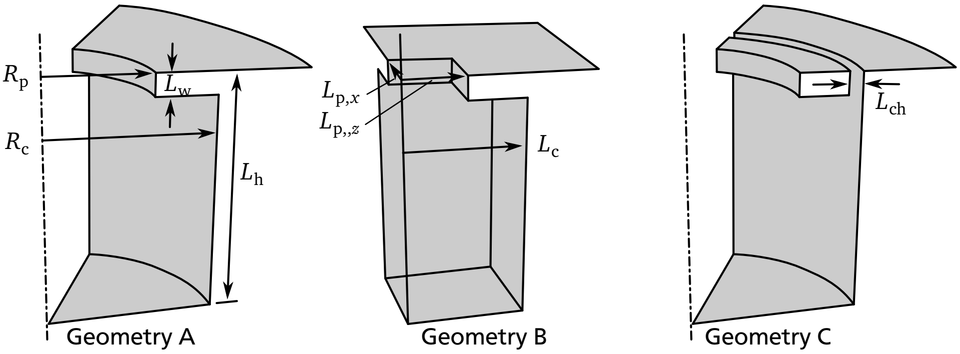

Figure 4.1: Classes of geometries

The dimensions are chosen such that they are similar to those that can be found for subsurface tunnels. Table 4.1 gives the combinations of geometric parameters for the cavities.

Geometry A is a basic 2D axisymmetric reentrant cavity with a circular pore and circular cavity. The pore radius and cavity radius are varied, wall thickness and cavity depth are fixed. Geometry B consists of a square cavity with a square or rectangular pore. Only the shape of the pore and the depth of the cavity was varied for this case. With the experiences from the simulations with Geometry A and B, Geometry C is created, which is a circular reentrant cavity with an additional thin channel connecting the liquid pool with the inside of the cavity. As the geometry is 2D axisymmetric, a piece of wall is hanging

Table 4.1: Geometric parameters, all dimensions given in 10^{-6} m

	Identifier	Pore size	Cavity size	L_h	L_w	L_ch
Geometry A	$R_{100}R_{\mathrm{c}150}$	$R_\mathrm{p} = 100$	$R_\mathrm{c} = 150$	500	30	-
	$R_{500}R_{\mathrm{c}550}$	$R_\mathrm{p} = 500$	$R_\mathrm{c} = 550$	500	30	-
Geometry B	$L_{71}H_{600}$	$L_{\mathrm{p},x} = L_{\mathrm{p},z} = 71$	$L_\mathrm{c} = 140$	600	30	-
	$L_{130}H_{200}$	$L_{\mathrm{p},x} = 130\ L_{\mathrm{p},z} = 38.67$	$L_\mathrm{c} = 140$	200	30	-
	$L_{130}H_{400}$	$L_{\mathrm{p},x} = 130\ L_{\mathrm{p},z} = 38.67$	$L_\mathrm{c} = 140$	400	30	-
	$L_{130}H_{600}$	$L_{\mathrm{p},x} = 130\ L_{\mathrm{p},z} = 38.67$	$L_\mathrm{c} = 140$	600	30	-
Geometry C	$R_{25}R_{\mathrm{c}150}L_{\mathrm{ch}10}$	$R_\mathrm{p} = 25$	$R_\mathrm{c} = 150$	500	30	10
	$R_{50}R_{\mathrm{c}150}L_{\mathrm{ch}10}$	$R_\mathrm{p} = 50$	$R_\mathrm{c} = 150$	500	30	10
	$R_{75}R_{\mathrm{c}150}L_{\mathrm{ch}10}$	$R_\mathrm{p} = 75$	$R_\mathrm{c} = 150$	500	30	10
	$R_{100}R_{\mathrm{c}150}L_{\mathrm{ch}5}$	$R_\mathrm{p} = 100$	$R_\mathrm{c} = 150$	500	30	5
	$R_{100}R_{\mathrm{c}150}L_{\mathrm{ch}10}$	$R_\mathrm{p} = 100$	$R_\mathrm{c} = 150$	500	30	10
	$R_{100}R_{\mathrm{c}150}L_{\mathrm{ch}40}$	$R_\mathrm{p} = 100$	$R_\mathrm{c} = 150$	500	30	40
	$R_{100}R_{\mathrm{c}150}H_{300}$	$R_\mathrm{p} = 100$	$R_\mathrm{c} = 150$	300	30	10
	$R_{125}R_{\mathrm{c}150}L_{\mathrm{ch}10}$	$R_\mathrm{p} = 125$	$R_\mathrm{c} = 150$	500	30	10
	$R_{100}R_{\mathrm{c}200}L_{\mathrm{ch}10}$	$R_\mathrm{p} = 100$	$R_\mathrm{c} = 200$	500	30	10
	$R_{100}R_{\mathrm{c}300}L_{\mathrm{ch}10}$	$R_\mathrm{p} = 100$	$R_\mathrm{c} = 300$	500	30	10

freely implying that such a geometry cannot exist in reality. Nevertheless, boiling at this surface shows some interesting characteristics enhancing the understanding of boiling processes occurring at reentrant surfaces and it is possible to imagine very similar surfaces which actually could be build in theory. As the effects observed with this geometry are similar to the effects observed with 3D geometries, the influence of geometric properties and sensitivity of the simulation on input parameters can be studied with reduced computational effort. In addition to the pore radius, cavity radius and depth, the channel width L_ch is varied in this case. With this geometry, conjugate heat transfer is calculated. The fluid and the solid domain are not perfectly matching. In order for heat transfer to the corner of the pore being possible, the thin channel in the fluid region is not considered in the solid region (see Figure 4.2).

4.1.2 Computational domain and boundary conditions

The computational domain together with the boundary conditions is shown in Figure 4.2. The wall at the circular cavity as well as the square cavity is set to an uniform fixed temperature. For the case of the circular cavity with the channel and the coupled solid region, a heat flux boundary condition is applied at the bottom of the solid. In order to keep the heat flow to the domain constant with changing cavity radius, the size of the patch with the heat flux boundary condition is kept constant for all cavity sizes. For the case of the square cavity, next to the section with the fixed temperature an adiabatic wall is set to increase the size of the fluid domain without increasing the heat input. As the size of the patches with heat flowing into the domain is rather arbitrarily set, a quantitative comparison with experimental data is difficult concerning heat transfer coefficient or bubble frequency.

During the simulations, before the bubble reaches the upper boundary, it is removed from the flow field to prevent large spurious velocities and a disturbance of the growth of the next bubble.

In the simulations, fluid properties are those of saturated R134a as given in Appendix A. Solid properties are those of pure copper. All properties are taken from VDI Heat atlas [38][39].

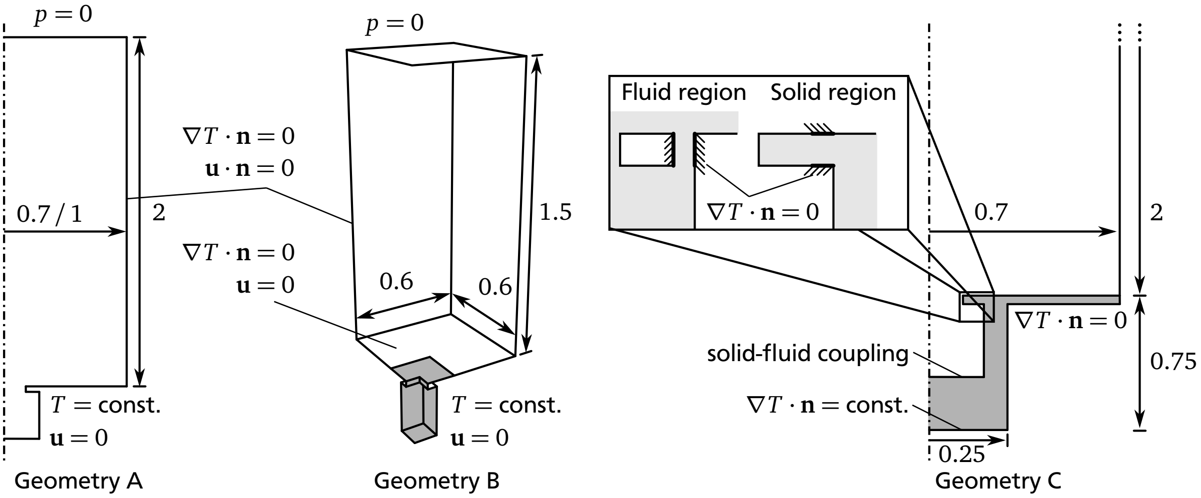

Figure 4.2: Computational domain and boundary conditions, dimensions given in 10^{-3} m

4.1.3 Discretization of the computational domain

The computational domain is discretized with a varying mesh resolution and hexahedral cells only. Figure 4.3 shows the computational domain together with the approximate cell size at different locations.

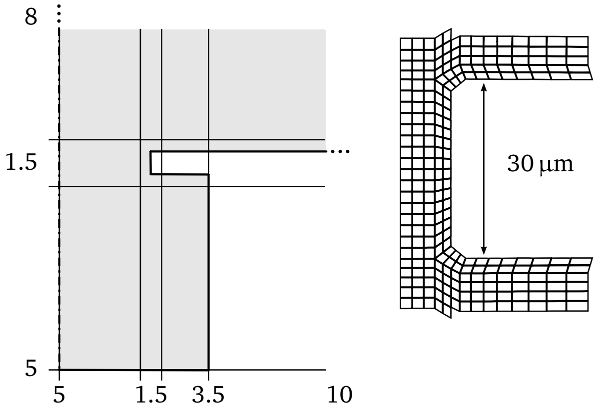

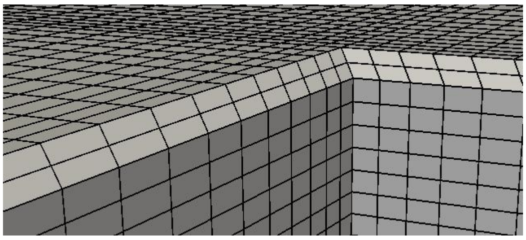

Figure 4.3: Discretization of computational domain, approximate cell sizes in 10^{-6} m

Figure 4.4: Medium mesh resolution at the corner of the pore in 3D

High mesh quality is important for the VOF solver and for curvature calculation. Special care needs to be taken about the mesh at the corners of the pore. In Figure 4.3, the mesh at the corner for the 2D axisymmetric and in Figure 4.4 for the 3D mesh (medium resolution) is shown. A small chamfer allows a smooth movement of the three phase contact line around the corner and assures that all the cells having a point on the wall also have a face on the wall. A grid convergence study was performed for the case $R_{100}R_{\mathrm{c}150}L_{\mathrm{ch}10}$ at $q = 120\,\mathrm{kW/m^2}$. Table 4.2 shows the wall superheat and bubble departure diameter for three meshes with "medium mesh" having the resolution employed for all the simulations on 2D axisymmetric grids, "coarse mesh" having approximately double the cell sizes, and "fine mesh" having half the cell sizes. Due to the complex interrelation between wall temperature, heat transfer, and contact angle, which is mainly caused by the microzone model and the coupling between solid and fluid region, no clear trend can be observed, neither for wall superheat nor for bubble departure diameter. But in fact, even the simulation on the coarse mesh is able to depict all the characteristics in heat transfer and fluid

Table 4.2: Grid convergence for case $R_{100}R_{c150}L_{ch10}$ at $q = 120\,\mathrm{kW/m^2}$

Resolution	Mesh size	Average wall superheat in K	Bubble departure diameter in 10^{-3} m
coarse	11 771	7.16	0.921
medium	43 154	7.23	0.945
fine	151 769	7.22	0.983

flow that can be observed on the fine mesh. Wall superheat is changing by 0.14 % between the medium and the fine mesh. This is less than the criteria for having reached steady state, which is introduced in the next section. Bubble departure diameter is the most sensitive parameter observed and is changing by 4 %, which is considerably more than the wall superheat but acceptable. It should be noted that the presented bubble diameter is an average value, the individual values vary by $0.003 \cdot 10^{-3}$ m in the simulation.

For the square cavity, an extremely thin liquid film develops in the corner of the pore, which is very difficult to resolve. Consequently, differences between the fine mesh and the medium mesh are larger than in the 2D case. Therefore, simulations are performed on the fine mesh. Figure 4.5 shows the liquid volume fraction inside the cavity as a function of time for the case $L_{130}H_{200}$ with 2 K wall superheat with three mesh resolutions and Figure 4.6 the liquid volume fraction for case $L_{130}H_{400}$.

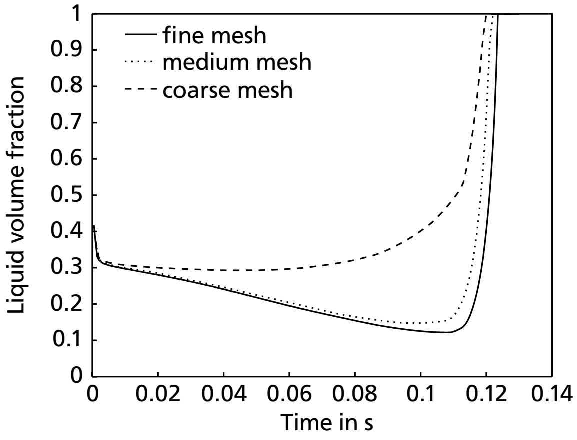

Figure 4.5: Mesh convergence with case $L_{130}H_{200}$

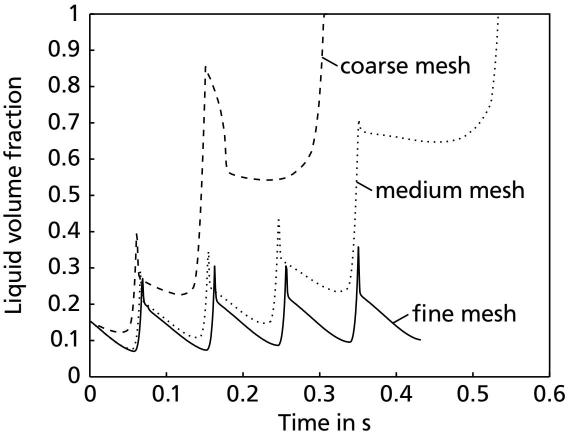

Figure 4.6: Mesh convergence with case $L_{130}H_{400}$

The mesh study shows that with increasing resolution the flow into the cavity decreases. Because of the dependence of liquid flow to the cavity on mesh resolution, only a more qualitative analysis of the results is given for the 3D single cavity cases.

4.1.4 Initial conditions and simulation procedure

Initially, a bubble nucleus is set into the cavity and a thermal boundary layer is set at the wall. The initial thermal boundary layer has a thickness of 300 µm and a linear temperature profile. The circular cavity cases as well as the square cavity with square pore are initialized with vapor filling the cavity up to 200 µm below the outer surface. Square cavities with rectangular pores initially are filled with vapor up to 100 µm below the outer surface.

For all simulations with the circular cavity with additional channel, simulation time is chosen such that a quasi-steady state is reached and consequently results being independent of the initial conditions. Figure 4.7 shows a typical evolution of the average wall superheat.

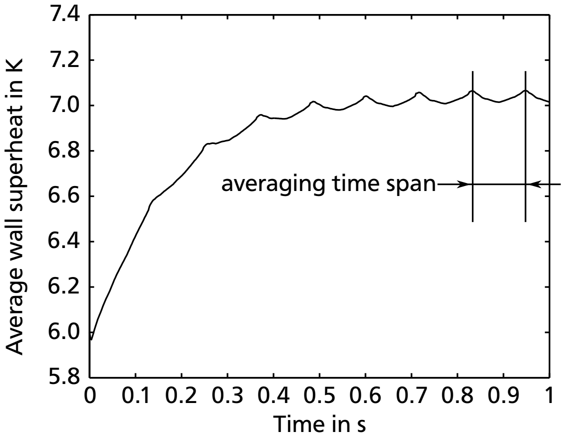

Figure 4.7: Evolution of wall superheat with time and averaging time span

Quantities for evaluation of the results are always averaged over the last bubble cycle, with wall superheat changing less than 0.5 % between the two temperature peaks.

4.1.5 Influence of selected setup properties on the results

The heat flux boundary condition allows the temperature at the fluid-solid interface to be nonuniform and vary with time. The influence of this effect on the flow field and overall simulation results compared to a fixed temperature boundary condition depends on fluid properties, solid properties, and heat flow. In order to determine the influence of the boundary condition on the results of the numerical simulations in this work, the average wall temperature is taken from the simulation with a heat flux of 120 kW/m^2 and set as fixed temperature boundary condition for a simulation with the same geometry. The resulting evaporation rates for a full bubble and cavity (360 deg) are given in Table 4.3, showing a deviation of less than 0.5 %.

Table 4.3: Evaporation rates for geometry $R_{100}R_{\mathrm{c}150}L_{\mathrm{ch}10}$

Boundary condition	Heat flux in kW/m^2	Wall superheat in K	Evaporation rate in 10^{-7} kg/s
Fixed heat flux	120	7.23 (average)	1.267
Fixed temperature	-	7.23	1.273

In this work, wall superheats are rather low due to the general working conditions of such kind of surfaces and the solid has a high thermal conductivity. As the influence of the boundary condition in this case is negligible, computational expensive calculations with 3D geometries are performed with fixed temperature boundary conditions.

As was presented in Section 3.4 the movement of the three phase contact line can be considered in the microzone model and has an influence on contact angle and heat transfer. For the simulations in this work, large portions of the three phase contact line are pinned at corners of the geometry or are moving rather slow. For the case presented in Table 4.3, the difference in average wall superheat between a case considering the movement of the contact line in the modeling equations and a case neglecting it, is about

0.3 %. As including the movement of the contact line introduces an additional source of error, e.g. due to small jumps in the contact line position at a corner due to spurious currents, it is neglected in all the simulations presented in the following.

The area treated in the microzone model is set up to 0.5 μm away from the three phase contact line. The remaining part of the fluid-solid interface in the cell is treated with the transition model as discussed in Section 3.5. Increasing the size of the area treated by the microzone model up to 1 μm away from the three phase contact line and thus decreasing the size of the area treated by the transition model results in a change in average wall superheat by 0.004 %, which is absolutely insignificant considering that the temperature values are obtained with an averaging procedure.

The evaporation coefficient f has a strong influence on the contact angle and evaporation rate in the microzone, as shown in Section 3.4. For low surface tension fluids such as R134a, f is usually much larger than for high surface tension fluids such as water. The effect on the overall simulation is depicted in Table 4.4.

Table 4.4: Influence of evaporation coefficient f for geometry $R_{100}R_{c150}L_{ch10}$ at $q = 120\,\mathrm{kW/m^2}$

Evaporation coefficient f	Average wall superheat in K	Contact angle in deg	$\dot{Q}_{cl}/\dot{Q}$
0.6	7.34	32.3	0.393
0.8	7.23	34.2	0.420
1	7.11	35.8	0.440

It is obvious that the choice of f affects the final results, especially for cases with a large portion of heat $\dot{Q}_{cl}/\dot{Q}$ going through the microzone region. For the simulations in this work, the evaporation coefficient is set to $f = 0.8$. Even though f strongly influences the results of the microzone model, increasing the value to unity results in a decrease of the wall superheat of only 1.7 % in the simulation. The evaporation coefficient in a generic experiment or industrial application depends on the purity of the fluid and thus care has to be taken when transferring results from numerical simulations to real systems.

The size of the domain can influence bubble growth, departure, and rise. As this work aims at studying the processes inside and close to the cavity, the domain is chosen to be rather small in order to decrease computational effort. The effect on the overall results is tested for the geometry $R_{100}R_{c150}L_{ch10}$, by doubling the size of the domain and adding an adiabatic wall section. The results are presented in Table 4.5.

Table 4.5: Influence of domain size for $R_{100}R_{c150}L_{ch10}$ at $q = 120\,\mathrm{kW/m^2}$

Radius of domain in 10^{-3} m	Average wall superheat in K	Bubble departure diameter in 10^{-3} m
0.7	7.23	0.945
1.4	6.82	0.937

As can be taken from the results, the wall superheat is approximately 6 % lower for the larger domain size. By adding an adiabatic wall section it is easier for cold liquid to disturb the thermal boundary layer and flow to the wall. Due to the high temperature of the thermal boundary layer in the selected simulation case, this results in a distinct change in wall superheat. Like the size of the diabatic wall section, the adiabatic wall section and the size of the heat flux boundary in the solid are chosen arbitrarily, comparisons can only be drawn between CFD simulations with the same setup and care has to be taken when comparing results with experiments.

4.2 Results for circular cavity

From the initialization, every simulation starts with a liquid film in the corner of the cavity. Simulations with circular reentrant cavities always lead to dryout or flooding of the cavity in this work. Figure 4.8 shows the bubble departure process for a dry cavity and a cavity with a liquid film in the upper corner.

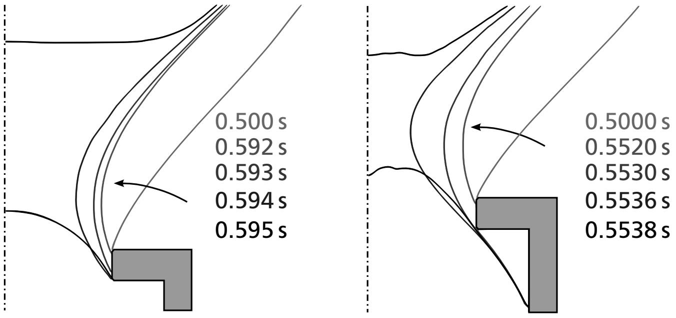

Figure 4.8: Bubble departure without (left) and with (right) liquid film for $R_{100}R_{c150}$

With the dry cavity, the three phase contact line moves into the pore, where it pins at the lower corner of the pore. Necking occurs above the pore and the bubble is released. For a circular reentrant cavity having two corners with right angles at the pore, the three phase contact line cannot run across the second corner, meaning that if the cavity is dry it will stay dry. If a liquid film is located inside the cavity which extends to the pore, the three phase contact line of the bubble foot can connect with the three phase contact line of the liquid film and flow from the pool to the liquid film is possible. In practice, for most conditions the liquid film evaporates during bubble growth to some extend and the three phase contact line moves away from the pore.

For a large pore radius or shallow cavity, the initial conditions determine whether there is flooding or dryout of the cavity. Figure 4.9 shows flooding of the cavity right after initialization, flooding at the first bubble departure, and dryout of the cavity. The horizontal line is the initial liquid-vapor interface with liquid above and vapor below the line. The only difference in the numerical simulations is the initial amount of liquid inside the cavity.

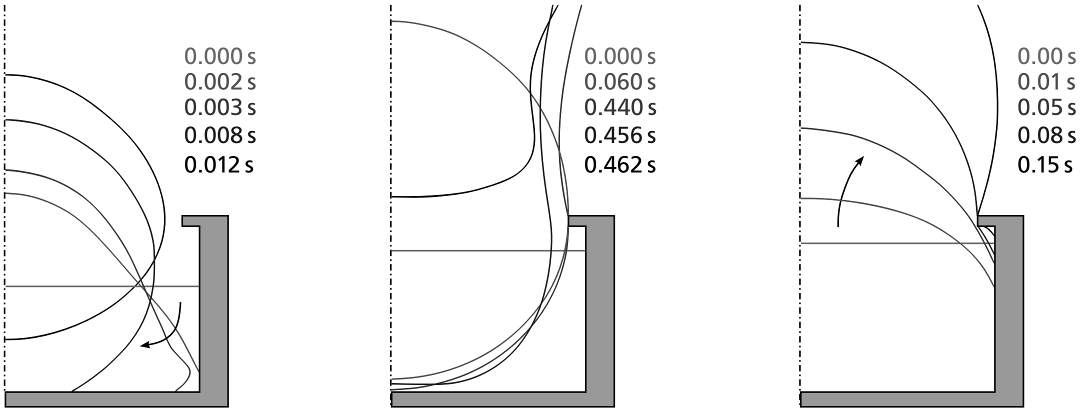

Figure 4.9: Influence of initial conditions for geometry $R_{500}R_{c550}$

Once the three phase contact line reaches the bottom of the cavity, it rapidly moves towards the symmetry axis. In this case, the bubble either leaves the cavity without vapor staying inside or, if the bubble touches the pore during its rise, some part of the bubble stays inside. If not all of the vapor leaves the cavity right at the beginning, it is very likely that this happens at the first bubble departure. For the case that the amount of liquid in the cavity for initialization is small enough or the cavity is deep enough, dryout occurs as observed for the geometry $R_{100}R_{c150}$.

In order to determine the influence of liquid films inside the cavity on heat transfer, simulations are performed with geometry $R_{100}R_{c150}$ with a dry cavity, with a liquid film artificially set into the upper corner of the cavity, and with a liquid film set into the upper and the lower corner of the cavity. Table 4.6 shows the influence of the liquid films on heat transfer for those three cases.

Table 4.6: Heat transfer for single circular cavity at 2 K wall superheat

	Heat flow in 10^{-3} W	$\dot{Q}_{\mathrm{cl}}/\dot{Q}$
Dry cavity	3.28	0.395
Liquid in upper corner of cavity	7.87	0.473
Liquid in upper and lower corner	12.8	0.482

It is apparent that liquid film evaporation inside the cavity strongly enhances heat transfer. The heat transferred through each liquid film is larger than the total heat transfer with a dry cavity. With two liquid films, almost half of the total heat is transferred within a distance of 0.5 µm from the contact line.

In several models, the removal of the thermal boundary layer with bubble departure is considered to account for transient conduction in this region. Mikic and Rohsenow [88] state that for a circular area twice the size of the bubble departure diameter, the thermal boundary layer is affected. Figure 4.10 shows the isothermal lines in steps of 0.2 K shortly before and after bubble departure for geometry $R_{100}R_{c150}$ with extended domain.

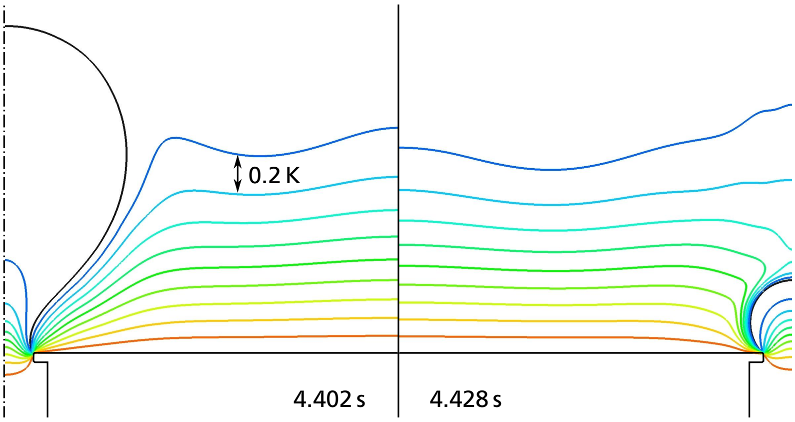

Figure 4.10: Thermal boundary layer before and after bubble departure

As can be taken from the isothermal lines, the thermal boundary layer is hardly affected by bubble departure for the parameters given. As the bubble foot is pinned at the pore, liquid flow is reduced close to the wall compared to bubble growth on a plain surface. Figure 4.11 shows the thermal energy in the superheated thermal boundary layer in terms of the latent heat removed by one departing bubble $\left(\int \rho_{\mathrm{l}} c_{\mathrm{l}} \left(T - T_{\mathrm{sat}}\right) \mathrm{d}V_{\mathrm{th}}\right) / \left(\Delta h_{\mathrm{v}} \rho_{\mathrm{v}} V_{\mathrm{b,dep}}\right)$. The energy is calculated up to a thickness of 0.5 mm and between a radius of the departure radius and twice the departure radius. The thermal energy in the boundary layer is hardly fluctuating during bubble departure. For boiling from a single pore with the given parameters, the assumption of Mikic and Rohsenow is obviously not applying. It should be noted that for boiling from several pores arranged closely together, a convective flow is created due to the rising bubbles which can lead to a considerable removal of sensible heat. For single cavities, free convection also removes heat outside the area influenced by the bubble.

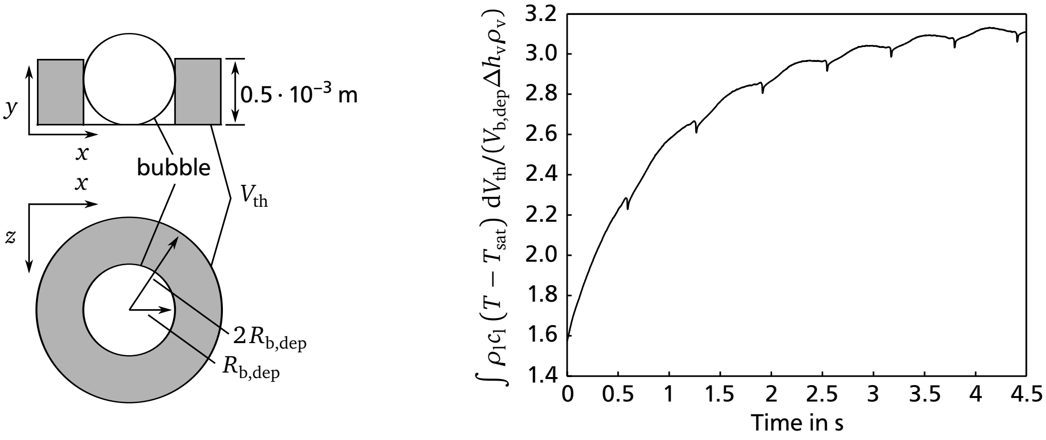

Figure 4.11: Variation of thermal energy in the thermal boundary layer

4.3 Results for square cavity

Having an additional corner in the pore and in the cavity, liquid can spread also in vertical direction. Figure 4.12 shows the liquid-vapor interface for geometry $L_{71}H_{600}$.

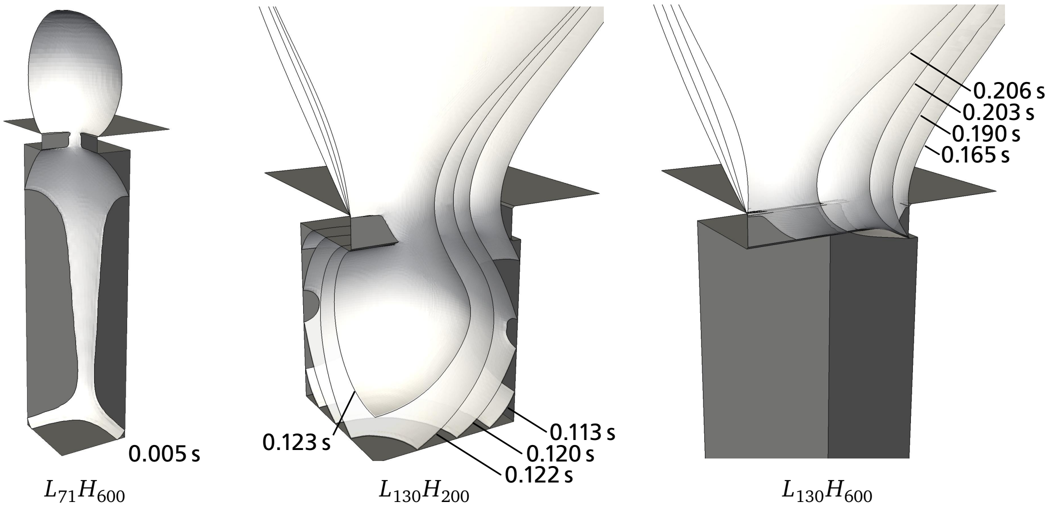

Figure 4.12: Liquid film in square cavity, flooding, and dryout of cavity

A thin liquid film is located in the corners of the geometry and also connects the liquid in the cavity with the liquid pool, allowing liquid flow into the cavity. Furthermore, the additional thin film area inside the cavity strongly increases heat transfer. At 2 K wall superheat, 0.0128 W of heat are transferred with geometry $R_{100}R_{c150}$ (for full 360 degrees) and two liquid films placed inside, while 0.0243 W of heat are transferred with geometry $L_{71}H_{600}$ before dryout.

During bubble growth, liquid is flowing into the cavity through the thin film in the corner of the pore. The amount of liquid flowing into the cavity depends on the driving pressure difference and flow resistance. For a given fluid, the pressure difference between liquid pool and film is determined by the geometry, the amount of liquid in the cavity, contact angle, and the size of the bubble. The flow resistance in this case is a function of the thickness of the thin film in the corner of the pore. During bubble growth more liquid evaporates inside the cavity than is flowing into the cavity, while during bubble departure a large amount of liquid can flow into the cavity.

For most of the tested geometries, either dryout or flooding of the cavity occurred after a few bubble cycles. In Figure 4.12 the flooding of geometry $L_{130}H_{200}$ and dryout of geometry $L_{130}H_{600}$ is depicted. Due to the strong dependence of the flow resistance on the thickness of the liquid film, almost no more liquid is flowing into the cavity once it is dry. If the cavity is already filled to a large fraction with liquid, the flow resistance is low and larger amounts of liquid can flow to into the cavity. The pressure jump across the liquid-vapor interface of the liquid film in the cavity first decreases with increasing film volume, but then increases again once the liquid film completely covers the side walls of the cavity.

For the simulated geometries, Figure 4.13 gives the evolution of the liquid volume fraction inside the cavity.

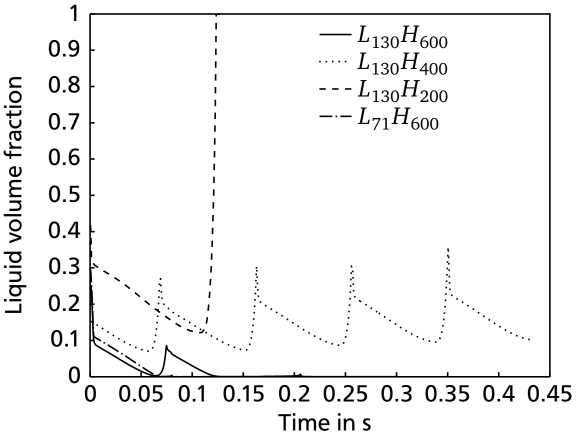

Figure 4.13: Liquid volume fraction inside square cavity

During bubble departure, liquid film thickness increases and consequently flow resistance decreases. Therefore, the flow rate of liquid flowing into the cavity is largest during departure. A shallow cavity leads to flooding while a deep cavity leads to dryout. This is caused by the stronger curvature of the liquid-vapor interface in the shallow cavity, which results in a larger driving pressure difference for the flow between pool and film. Geometry $L_{130}H_{200}$ is filled with liquid during the first bubble cycle. For the time simulated, geometry $L_{130}H_{400}$ is neither flooded nor dries out, but the slight increase in volume fraction with time suggests that flooding might occur with more time given. For geometry $L_{130}H_{600}$ it takes two bubble cycles for dryout, while the cavity with geometry $L_{71}H_{600}$ immediately becomes dry. With the square pore, the flow resistance between liquid pool and liquid film is larger than with the rectangular pore and dryout occurs earlier.

The simulations show that with a single square cavity, obtaining a stable suction evaporation mode is extremely difficult due to the strong dependence of flow resistance between liquid pool and liquid film on the liquid volume fraction in the cavity.

4.4 Results for circular cavity with additional connection to the pool

The additional channel connecting the cavity with the pool allows liquid flow to or from the cavity to be substantial not only during bubble departure but also during bubble growth. Furthermore, the cavity is not prone to flooding as long as the liquid film is not reaching the bottom of the cavity. Consequently, the liquid film volume in the upper corner is pulsating with the frequency of bubble departure. The pressure inside the liquid film is determined by the pressure of the vapor in the cavity and the pressure jump across the liquid-vapor interface of the film. Bubble size determines the pressure of the vapor and liquid volume in the cavity determines the pressure jump across the liquid-vapor interface. Shortly after bubble departure with the next bubble being small, the pressure inside the vapor phase is high and liquid is pushed out of the film into the pool until curvature of bubble and liquid film are approximately equal. With the bubble growing, pressure of the vapor decreases and liquid flows from the pool into the film. Shortly before bubble departure, pressure is lowest and the liquid film reaches its maximal size. As the channel is located right in the corner of the cavity, a complete dryout can only occur if the evaporation rate is larger than liquid flow through the channel, which is not observed for the heat fluxes studied.

Figure 4.14 shows two different bubble departure mechanisms which are observed, as well as the condition leading to flooding of the cavity. The given times match the time axis in Figure 4.15 which is not starting at initialization.

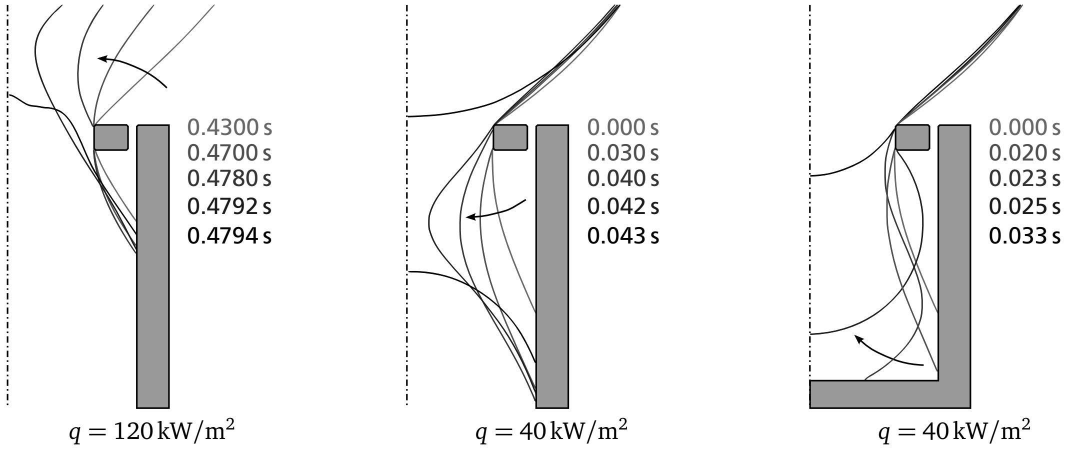

Figure 4.14: Bubble departure with geometry $R_{100}R_{\mathrm{c}150}L_{\mathrm{ch}10}$ (left and center) and $R_{100}R_{\mathrm{c}150}H_{300}$ (right)

If the liquid film has not reached the corner of the pore yet, departure of the bubble is almost the same as observed for a dry cavity. The three phase contact line moves into the pore, pins at the lower corner of the pore and the liquid-vapor interface contracts until the bubble is released. If liquid is flowing into the liquid film during bubble growth and departure, this process can proceed very fast as vapor is pushed into the bubble not only because of evaporation but also because of the increase of liquid volume inside the cavity.

With liquid flowing into the film during bubble growth, the film can reach a point where it cannot hold the liquid anymore with the given cavity dimensions. In this case, the liquid film extends upwards through the pore towards the bubble foot and the rotational axis, or reaches the bottom of the cavity. Figure 4.14 illustrates this behavior with geometry $R_{100}R_{\mathrm{c}150}L_{\mathrm{ch}10}$ and a heat flux of $q = 40\,\mathrm{kW/m^2}$. If the cavity is not deep enough and the liquid film reaches the bottom of the cavity, flooding is observed as for the cavity without channel in Figure 4.9. With the bubble departure being induced by the liquid film growing through the pore to the bubble foot, the bubble frequency increases.

The amplitude of the fluctuations of the liquid volume inside the cavity as well as the average volume of liquid is influenced by the geometry and the heat flux. Figure 4.15 shows the fraction of liquid inside the cavity for a variation of heat flux and a variation of channel width. An increase of heat flux leads to a decrease of liquid volume inside the cavity and a decrease in the amplitude of the liquid volume fluctuations. With increasing heat flux, the surface temperature increases and consequently the contact angle increases. Furthermore, as evaporation rates are higher in this case, more liquid has to flow through the thin channel, increasing the pressure drop. Bubble frequency increases with the evaporation rate.

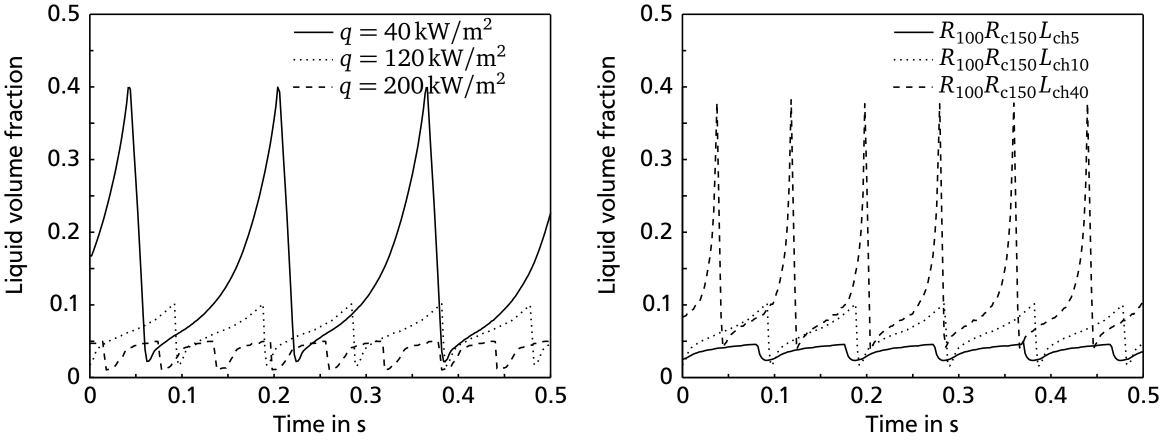

(a) $R_{100}R_{c150}L_{ch10}$ (b) $q = 120\,\mathrm{kW/m^2}$

Figure 4.15: Liquid volume fraction in cavity

Increasing the channel width also increases the amplitude of the fluctuations and the amount of liquid inside the cavity, as flow resistance between pool and liquid film decreases. While the frequency is the same for geometry $R_{100}R_{c150}L_{ch5}$ and $R_{100}R_{c150}L_{ch10}$, geometry $R_{100}R_{c150}L_{ch40}$ shows a slight increase. The reason for this behavior is the induced bubble departure by the liquid film extending upwards through the pore as described before.

Obvious is the striking similarity between the influence of the channel width and the heat flux. The effect of increasing the channel width is the same as decreasing the heat flux except for the change in bubble cycle time with changing heat flux. In fact, as shown in [34], heat flux and flow resistance through the channel can be combined in one characteristic parameter determining the amount of liquid located inside the cavity.

The effect of pore radius on liquid flow into the cavity is shown in Figure 4.16 for a low and a high heat flux.

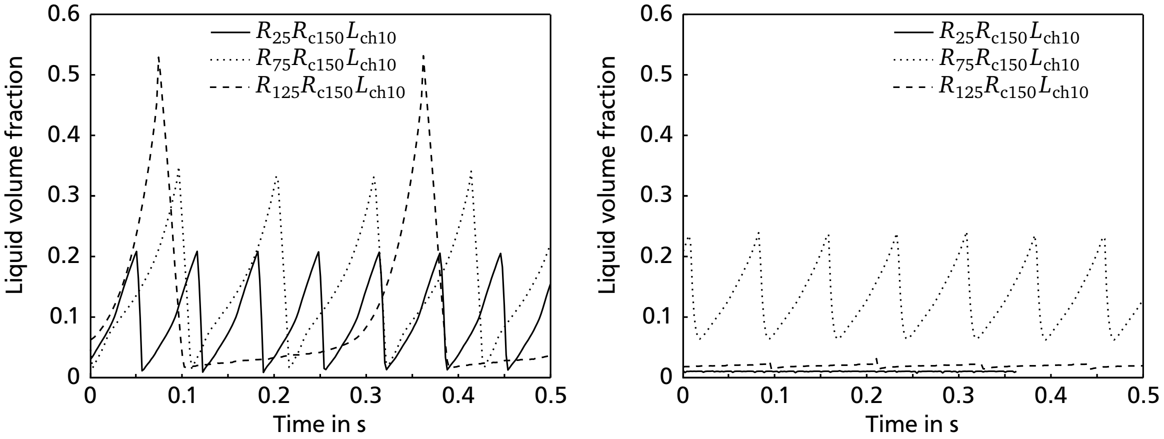

(a) $q = 40\,\mathrm{kW/m^2}$ (b) $q = 120\,\mathrm{kW/m^2}$

Figure 4.16: Liquid volume fraction in cavity for different pore sizes

With the low heat flux, liquid volume increases inside the cavity with pore radius. This is the expected result, as bubble departure diameter increases with pore radius. With larger bubbles, the pressure of the vapor is lower and consequently the driving pressure difference between liquid pool and film increases.

For the high heat flux, liquid films stay very small for geometries $R_{25}R_{\mathrm{c}150}L_{\mathrm{ch}10}$ and $R_{125}R_{\mathrm{c}150}L_{\mathrm{ch}10}$, while the average amount of liquid in the cavity only slightly decreases for geometry $R_{75}R_{\mathrm{c}150}L_{\mathrm{ch}10}$ compared with the low heat flux. With geometry $R_{25}R_{\mathrm{c}150}L_{\mathrm{ch}10}$, bubbles are smallest and wall superheat is highest and the resulting large contact angle keeps the liquid film in the corner. For both, $R_{125}R_{\mathrm{c}150}L_{\mathrm{ch}10}$ and $R_{75}R_{\mathrm{c}150}L_{\mathrm{ch}10}$, the liquid film pins at the pore as depicted in Figure 4.17 and only the lower contact line moves up and down. As the volume between the corner of the pore and wall of the cavity is much larger for the smaller pore size, liquid film volume and volume fluctuations are larger in this case, too.

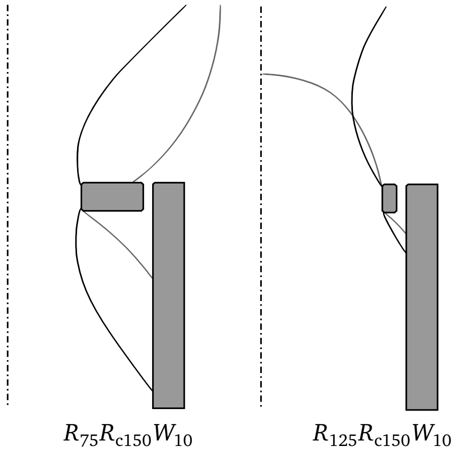

Figure 4.17: Minimal and maximal size of liquid film at $q = 120\,\mathrm{kW/m^2}$

In order to evaluate the heat transfer performance, a heat transfer coefficient is calculated based on the average temperature of the solid-fluid interface and the area of the patch with the heat flux boundary condition of the solid region. Figure 4.18 shows the heat transfer coefficient as a function of heat flux. It should be kept in mind that the absolute value of the heat transfer depends on the size of the computational domain.

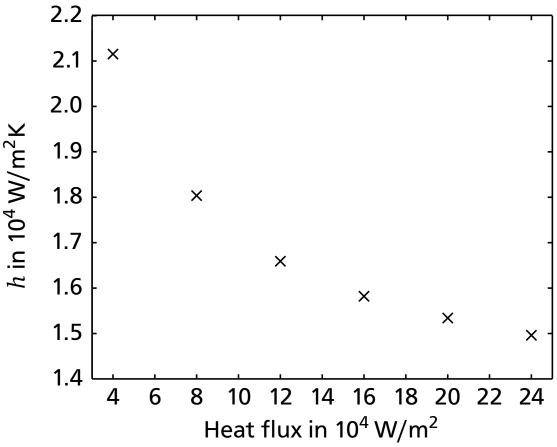

Figure 4.18: Heat transfer coefficient versus heat flux for geometry $R_{100}R_{\mathrm{c}150}L_{\mathrm{ch}10}$

The heat transfer coefficient is decreasing with increasing heat flux. The reason for this behavior can be found in the characteristic of the heat transfer in the microzone region. As can already be taken from Table 4.6 the three phase contact line plays an important role in heat transfer for boiling from reentrant cavities. The liquid film inside the cavity as well as the mostly pinned contact line at the bubble foot increase the total length of the contact line drastically compared to boiling processes at plain surfaces. The thermal resistance of the microzone region increases with wall superheat, as the contact angle increases. With heat transfer being dominated by the heat flowing through this area, the heat transfer coefficient consequently decreases with increasing heat flux.

The strong influence of the microzone region also becomes evident when looking at the heat transfer coefficient as a function of total contact line length, shown in Figure 4.19.

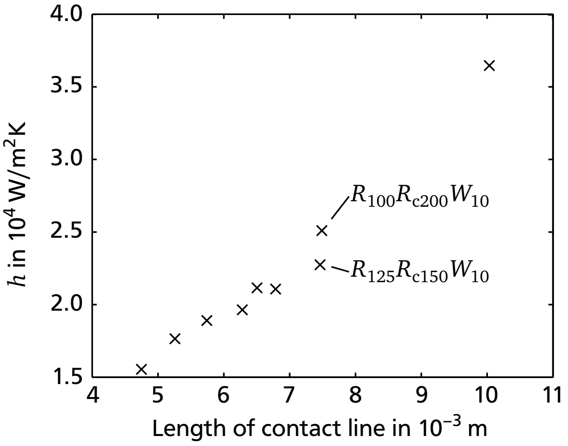

Figure 4.19: Heat transfer coefficient versus length of contact line at $q = 40\,\mathrm{kW/m^2}$

For a fixed heat flux of $q = 40\,\mathrm{kW/m^2}$, there is an almost linear relation between heat transfer coefficient and total contact line length. The difference in heat transfer coefficient for the two cases $R_{125}R_{c150}L_{ch10}$ and $R_{100}R_{c200}L_{ch10}$ is due to a difference in wetted area. As the pore is smaller and the cavity width is larger, the liquid film is larger for the case $R_{100}R_{c200}L_{ch10}$. With increasing heat flux, convective heat transfer at the bubble foot and inside the channel increases and the dependence of heat transfer coefficient on contact line length decreases.

5 Numerical Simulations of Boiling from Subsurface Tunnels with Two Pores

In this chapter, setup, procedure, and results of numerical simulations of boiling from a subsurface tunnel connected through two pores to a liquid pool are presented. The geometry is similar to structures that can be found on tubes with subsurface tunnels but the assumption of symmetry limits the comparability with real structures. Interaction between fluid flow at the two pores and influence of pore and tunnel geometry on the boiling mode is studied and heat transfer characteristics are evaluated.

5.1 Setup and procedure

In the following, the setup of the simulations with geometries with two pores is described and the simulation procedure is discussed. Two pores allow the simulation of bubble growth and flow into the tunnel at the same time, while symmetry planes can be employed to keep the number of cells manageable. In general, the cases are designed to keep the number of parameters small in order to be able to identify the influence of process parameters on heat and fluid flow.

5.1.1 Geometries

Figure 5.1 shows the geometry of the surfaces studied, dimensions are given in Table 5.1.

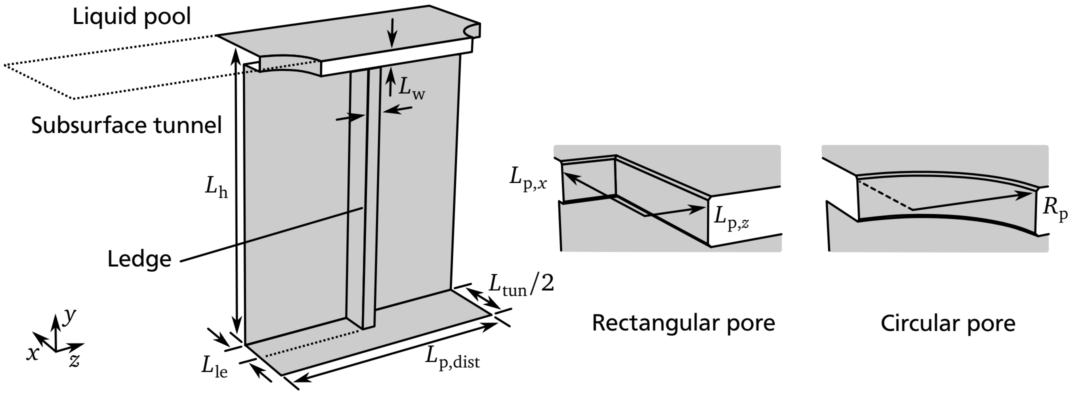

Figure 5.1: Geometry of subsurface tunnel and pores

A reference geometry is defined and the changes in dimensions with other geometries are highlighted in the table. The geometry consists of a short piece of subsurface tunnel connected through two pores with the liquid pool. Inside the tunnel, a solid ledge is introduced allowing the liquid film to spread from the upper to the lower corner inside the tunnel. Experimental observations show that with some high performance structures liquid films also are present in the lower corners. The pore shape and size are varied as well as the depth of the tunnel and the size of the ledge. For one geometry, pores with different sizes are employed, while otherwise pore shapes and sizes of the two pores are identical.

Table 5.1: Geometric parameters, all dimensions given in 10^{-6} m

Identifier	Pore size 1	Pore size 2	L_h	L_le
$L_{39}L_{39}$ (reference case)	$L_{\mathrm{p},x} = 130$, $L_{\mathrm{p},z} = 38.67$	$L_{\mathrm{p},x} = 130$, $L_{\mathrm{p},z} = 38.67$	600	60
$L_{39}L_{39}H_{400}$	$L_{\mathrm{p},x} = 130$, $L_{\mathrm{p},z} = 38.67$	$L_{\mathrm{p},x} = 130$, $L_{\mathrm{p},z} = 38.67$	400	60
$L_{39}L_{39}S_{30}$	$L_{\mathrm{p},x} = 130$, $L_{\mathrm{p},z} = 38.67$	$L_{\mathrm{p},x} = 130$, $L_{\mathrm{p},z} = 38.67$	600	30
$L_{39}L_{19}$	$L_{\mathrm{p},x} = 130$, $L_{\mathrm{p},z} = 38.67$	$L_{\mathrm{p},x} = 130$, $L_{\mathrm{p},z} = 19.335$	600	60
$L_{19}L_{19}$	$L_{\mathrm{p},x} = 130$, $L_{\mathrm{p},z} = 19.335$	$L_{\mathrm{p},x} = 130$, $L_{\mathrm{p},z} = 19.335$	600	60
$L_{130}L_{130}$	$L_{\mathrm{p},x} = 38.67$, $L_{\mathrm{p},z} = 130$	$L_{\mathrm{p},x} = 38.67$, $L_{\mathrm{p},z} = 130$	600	60
$R_{80}R_{80}$	$R_\mathrm{p} = 80$	$R_\mathrm{p} = 80$	600	60

The dimensions are chosen based on the values found in literature for subsurface tunnels and are adapted such that the suction evaporation mode is obtained with the selected geometry and wall superheat. Circular and rectangular pore geometries are studied. The open area of a pore with $L_{\mathrm{p},x} = 130\,\mu\mathrm{m}$ and $L_{\mathrm{p},z} = 38.67\,\mu\mathrm{m}$ is equal to the area of a pore with radius $R_\mathrm{p} = 80\,\mu\mathrm{m}$. The pore distance is always set to $L_\mathrm{p,dist} = 500\,\mu\mathrm{m}$, the thickness of the solid walls to $L_\mathrm{w} = 30\,\mu\mathrm{m}$, and the width of the tunnel to $L_\mathrm{tun} = 280\,\mu\mathrm{m}$. The depth of the tunnel is varied until the suction evaporation mode is obtained for the rectangular pore shapes and finally set to $L_\mathrm{h} = 600\,\mu\mathrm{m}$, except for geometry $L_{39}L_{39}H_{400}$.

5.1.2 Computational domain and boundary conditions

The computational domain and boundary conditions are similar to those employed for the single square cavity. The computational domain is depicted in Figure 5.2.

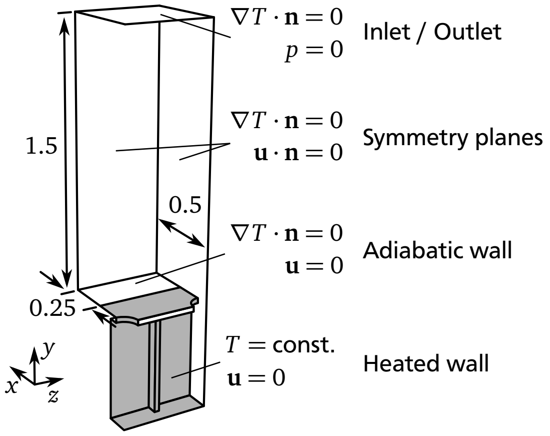

Figure 5.2: Computational domain and boundary conditions, dimensions given in 10^{-3} m

Each of the two pores is cut by two symmetry planes. The symmetry planes at the pores limit the maximal bubble radius that can be simulated to approximately $L_\mathrm{p,dist}$. Consequently, the computational domain also extends $500\,\mu\mathrm{m}$ in x-direction normal to the symmetry plane of the subsurface tunnel. Another symmetry plane is set at the boundary limiting the domain in x-direction. From the outer surface of the geometry, the computational domain extends $1\,500\,\mu\mathrm{m}$ upwards, giving enough space for bubble departure and a short rise period before it is deleted from the domain. At the top end of the domain a fixed pressure boundary condition is set. With the symmetry planes being this close to the departing bubble, it is likely that bubble rise is affected by the boundary conditions. As mostly the processes occurring inside the tunnel and at the pores are of interest, this is accepted in favor of a decrease in computational effort.

The simulations with single reentrant cavities only show minimal differences between calculations with fixed wall temperature and those with the conjugate heat transfer being simulated. Therefore, in order to reduce the computational effort, a fixed temperature boundary condition is selected at the solid wall in the tunnel and on half of the outer solid wall. The solid wall on the outside with a distance of more than 250 µm from the symmetry plane of the tunnel is set adiabatic. This split of the wall boundary condition is performed to reproduce a distance of 500 µm between neighboring subsurface tunnels in terms of heat transfer.

With a fixed wall temperature, the contact angle of the liquid-vapor interface with the solid wall is fixed to the value given by the microzone model for the given wall superheat. Simulations are performed with a wall superheat of 1 K and 2 K, leading to the contact angles given in Table 5.2.

Table 5.2: Wall superheat and contact angle

Wall superheat in K	Contact angle in deg	Calculated geometries	
1	18.52	$L_{39}L_{39}$, $L_{39}L_{39}S_{30}$, $L_{39}L_{19}$, $L_{19}L_{19}$	$R_{80}R_{80}$, $L_{39}L_{39}H_{400}$
2	23.05	$L_{39}L_{39}$, $L_{39}L_{39}S_{30}$, $L_{39}L_{19}$, $L_{19}L_{19}$	$L_{130}L_{130}$

Fluid properties are those of saturated R134a at a saturation temperature of 20 °C and given in Appendix A.

5.1.3 Discretization of the computational domain

The computational domain is discretized in hexahedral cells, with varying resolution at different locations of the domain. Simulations are performed with three different mesh resolutions, “coarse”, “medium”, “fine”, to assess the influence of the mesh on the solution. For the highest resolution, only a local adaptive mesh refinement is performed in the vicinity of the liquid-vapor interface. The medium mesh has double the resolution of the coarse mesh. The mesh at the pore together with liquid-vapor interface and the refined cells of the finest mesh is shown in Figure 5.3.

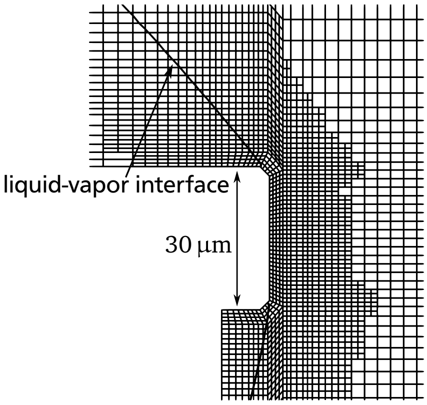

Figure 5.3: Dynamic mesh refinement at the liquid-vapor interface

The refinement of the mesh is performed up to a distance of 20 µm from the reconstructed liquid-vapor interface. The mesh is updated every 20 time steps to follow the interface. At all sharp corners of the geometry a chamfer is modeled to allow the contact line to move across the corner.

The size of the meshes is given in Table 5.3. Due to the dynamic mesh, the size of the fine mesh varies strongly. For the coarse and the medium mesh, the size varies with pore dimension and tunnel geometry.

Table 5.3: Size of meshes

Resolution	coarse	medium	fine
Mesh Size	400 000 – 500 000	$2.15 \cdot 10^6 - 2.33 \cdot 10^6$	$2.8 \cdot 10^6 - 4.0 \cdot 10^6$

Like with the single cavities, a grading is employed to allow a smooth transition between the different cell sizes. The spatial resolution of the mesh is increased where the highest gradients are expected. In wall normal direction, the size of the cells at the pore is approximately 3 µm, 1.5 µm, and 0.75 µm for the coarse, medium, and fine mesh. In the middle of the tunnel at the symmetry plane, the cells can be up to three times the size of the cells at the pore.

For all geometries and wall temperatures, simulations are performed on the coarse, medium, and fine mesh. This simulation procedure is described in the next section. Consequently, mesh convergence can be evaluated for each case individually. Obtaining mesh convergence is difficult for the given problems. There is capillary driven liquid flow through thin films in the corners of the pores, strongly curved liquid-vapor interfaces inside and outside of the tunnel, and high vapor flow velocities from the tunnel to the bubble. At the highest resolution, cells locally are already very small reaching the length scale of the subgrid scale model and leading to timesteps around $1 \cdot 10^{-7}$ s. With further refinement, calculation time of one bubble cycle would be several months, even on a high performance computer, and the size of the mesh would rule out pre- and postprocessing on a typical desktop machine. Furthermore, it would be questionable if the solution actually would improve as the curvature calculation is not necessarily mesh converging as was shown by Raessi et al. [100] and will also be shown below. On the other side, simulations on the coarse and also on the medium mesh suffer from numerical diffusion of the VOF field in some locations (see Section 3.6 for the treatment). If due to diffusion the three phase contact line on the coarse and medium mesh extends and additional liquid drops appear inside the tunnel on the solid wall, the heat transfer increases. Therefore, no clear trend of the heat transfer with mesh refinement might be observed and it might appear that the heat transfer is changing significantly with mesh resolution, even though the rather small temperature gradients can easily be resolved on the medium and fine mesh. Actually, at the chosen wall superheat, a much finer mesh is required for capturing the hydrodynamic effects than for calculating heat transfer correctly. Table 5.4 shows the mesh convergence of heat transfer and the amount of liquid located inside the tunnel.

The change in the average heat flow between the fine and the medium mesh is between 1.1 % and 6.7 %. The bubble departure diameter only shows minor differences. The relative difference in liquid volume fraction increases with decreasing film volume. With decreasing volume, fewer cells are located inside the liquid film. Therefore, the accuracy of the calculation of flow and pressure gradients inside the film decreases. For the case with the smallest liquid films here, the difference in liquid volume fraction between the medium and fine mesh is about 7 %. The minimal amount of liquid in the tunnel during one bubble cycle first increases with mesh resolution and then decreases again. This behavior can be explained by the characteristic of curvature calculation as explained in the following.

As was mentioned earlier, curvature calculation is not necessarily mesh converging, and it has been shown that VOF methods can have difficulties to correctly incorporate the effect of contact angle [140]. In order to estimate the size of the error in pressure jump across the liquid-vapor interface, a case with a steady liquid film in the tunnel is simulated and compared with the solution of SURFACE EVOLVER [16].

Table 5.4: Grid convergence for different cases

Geometry, wall superheat	Resolution	Average heat flow in 10^{-3} W	Bubble departure diameter in 10^{-3} m	Minimal liquid volume fraction in tunnel
$L_{39}L_{39}$, 1 K	coarse	6.84	0.763	0.127
	medium	6.68	0.791	0.133
	fine	6.26	0.796	0.131
$L_{39}L_{39}$, 2 K	coarse	13.0	0.793	0.107
	medium	11.9	0.853	0.128
	fine	11.6	0.866	0.123
$L_{19}L_{19}$, 1 K	coarse	7.77	0.587	0.038
	medium	7.64	0.611	0.043
	fine	7.55	0.612	0.046

The program Surface Evolver and the solution procedure in there is explained in more detail in Section 6.1.3. Figure 5.4 shows the shape of the liquid-vapor interface and the wall geometry of the case $L_{39}L_{39}$ from the CFD simulation and from Surface Evolver. The surface colored in light gray results from the simulation while the mesh is calculated by Surface Evolver.

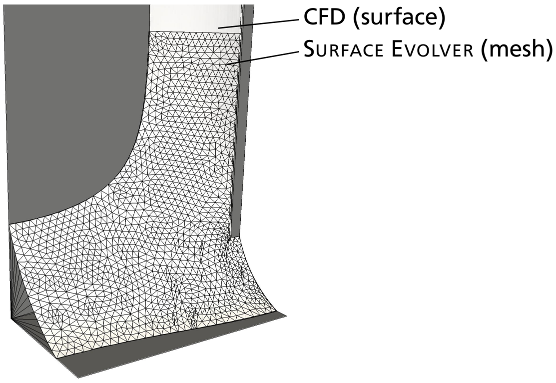

Figure 5.4: Shape of liquid-vapor interface calculated from CFD simulation and from Surface Evolver

The shape of the liquid-vapor interface from the CFD simulation and from Surface Evolver show virtually no difference. The pressure jump calculated from simulation for three different mesh resolutions and calculated from Surface Evolver is given in Table 5.5. As can be taken from the table, the pressure jump is underestimated by up to 9 % by the simulation compared to Surface Evolver. An underestimation of the pressure jump is also observed for the simulation of the capillary rise presented in Section 3.7. Furthermore, the fine mesh is not performing better than the medium mesh or even the coarse mesh. For the volume fraction of 0.34, the liquid film reaches the symmetry plane of the tunnel, which is why the pressure jump increases compared to the smaller liquid volume.

With the results from the grid study, it is believed that the fine mesh resolution potentially is sufficient to resolve the effects governing the process. Considering the sensitivity of the results to geometric properties, as will be shown later, and the restrictions caused by the introduction of symmetry planes, it can be assumed that numerical errors are much smaller than modeling errors resulting from the limitations in representing realistic surface structures or properties.

Table 5.5: Pressure jump at liquid-vapor interface

Contact angle in deg	Liquid volume fraction	Pressure jump in Pa from CFD coarse	medium	fine	Pressure jump in Pa from SURFACE EVOLVER
23.05	0.08	84.4	84.7	82.9	89.5
	0.17	53.3	54.1	53.0	58.2
	0.34	67.3	68.0	67.9	71.3
18.52	0.07	104	104	103	112

5.1.4 Initial conditions and simulation procedure

As with the single cavity, initially a bubble nucleus is set into the tunnel. On the outer surface, a temperature boundary layer is initiated in the fluid. The timestep is adapted during the simulations based on the CFL number. Simulations are performed on the "Lichtenberg" high performance computer at TU Darmstadt. For the highest mesh resolution, 96 processor cores are employed with the calculation of one bubble cycle taking 10 to 20 days. Due to the high computational costs, the procedure depicted in Figure 5.5 is applied to obtain a quasi-steady solution.

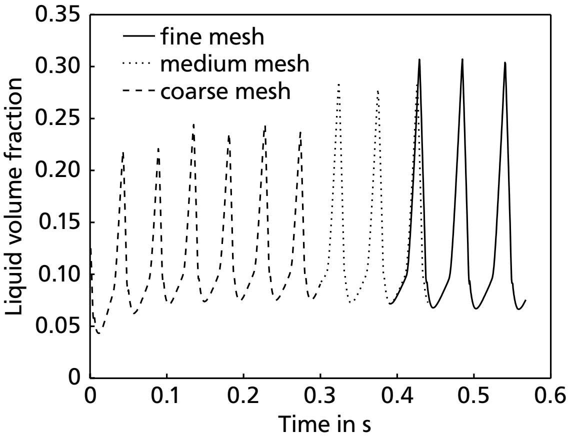

Figure 5.5: Evolution of liquid volume fraction inside tunnel

First, simulations are performed on the coarse mesh until the liquid volume in the tunnel reached a quasi-steady state. By then, the changes in the temperature boundary layer are usually small as well, as it carries only little energy for the selected wall temperatures. The solution on the coarse mesh is used as initial condition for the simulation on the medium mesh, and again a quasi-steady solution is obtained. Finally, approximately two bubble cycles are simulated with the finest mesh. Figure 5.5 shows the development of the liquid volume fraction with this procedure for the case $L_{39}L_{39}S_{30}$ with 1 K wall superheat. In this case, the time intervals of the simulations on the fine mesh and on the medium mesh overlap to illustrate mesh convergence. Again, averaging is performed over the last bubble cycle for the quantities being of interest.

For the cases with flooding of the tunnel being observed, simulations are started with the same initial conditions for all three mesh resolutions. Figure 5.6 shows the evolution of the liquid volume fraction for the case $R_{80}R_{80}$ with 1 K wall superheat, in which flooding occurs.

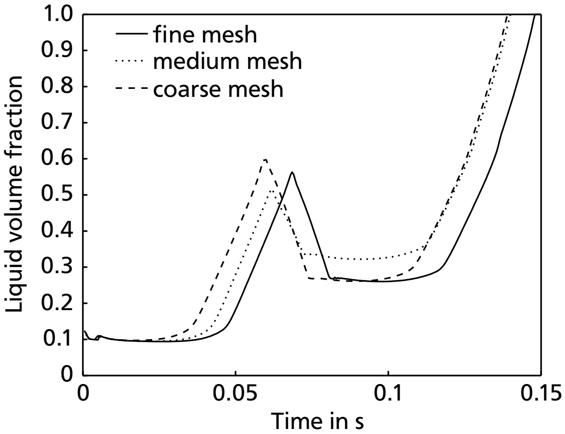

Figure 5.6: Evolution of liquid volume fraction inside tunnel for case with flooding

5.2 Results

In this section, first a description of the hydrodynamics is given. The observed influence of and sensitivity to the geometric properties is described. Afterwards the heat transfer properties are analyzed. In the following the term “active pore” will be used for a pore with a bubble growing at and the term “inactive pore” for a pore without a bubble growing at. The system consisting of liquid pool, liquid film, vapor in the tunnel, and bubble can be regarded as a hydraulic circuit as illustrated in Figure 5.7.

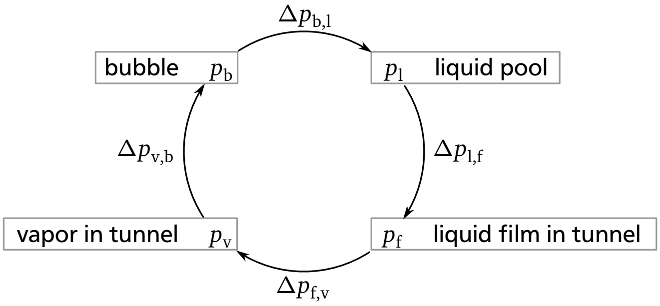

Figure 5.7: Hydraulic circuit

The mesh rule for the pressure differences is given by $0 = \Delta p_{\mathrm{l,f}} + \Delta p_{\mathrm{f,v}} + \Delta p_{\mathrm{v,b}} + \Delta p_{\mathrm{b,l}}$. Several effects occurring with the subsurface tunnel will be explained referring to the pressure differences in Figure 5.7.

Figure 5.8 shows the evolution of the liquid-vapor interface inside the tunnel during bubble growth and departure at one pore for the reference case. During bubble growth at the active pore, liquid is flowing through the inactive pore into the tunnel. With increasing bubble volume, pressure of the vapor in the bubble p_{b} and of the vapor in the tunnel p_{v} decreases and consequently liquid film volume increases. The rate of increase depends on the flow resistance at the pore, the pressure of the vapor p_{v}, and the pressure jump across the liquid-vapor interface in the tunnel $\Delta p_{\mathrm{f,v}}$. The pressure of the vapor is determined by curvature of the bubble and consequently by the bubble volume but also by vapor flow from the tunnel into the bubble. The pressure jump across the liquid-vapor interface $\Delta p_{\mathrm{f,v}}$ is determined by the curvature of the liquid-vapor interface in the tunnel, which depends on contact angle and volume of the liquid film. After departure, the pressure of the vapor suddenly increases because of the smaller bubble size and liquid is flowing from the liquid film located inside the tunnel to the liquid pool until the

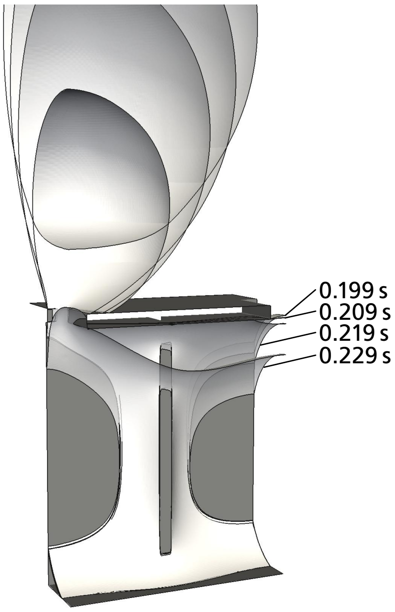

Figure 5.8: Evolution of liquid-vapor interface, case $L_{39}L_{39}$ at 2 K wall superheat

curvature of the liquid-vapor interface in the tunnel balances the pressure difference between vapor in the tunnel and liquid pool $\Delta p_{\mathrm{l,f}}$.

Shortly before bubble departure, the bubble starts to contract at the bubble foot and flow velocity increases. The pore itself acts like a throttle such that the dynamic pressure is dissipated. Consequently, the pressure inside the tunnel is increased compared to the pressure inside the bubble. Figure 5.9 shows the pressure difference between vapor in the tunnel and bubble $\Delta p_{\mathrm{v,b}}$ for the reference case $L_{39}L_{39}$ at 1 K and 2 K wall superheat.

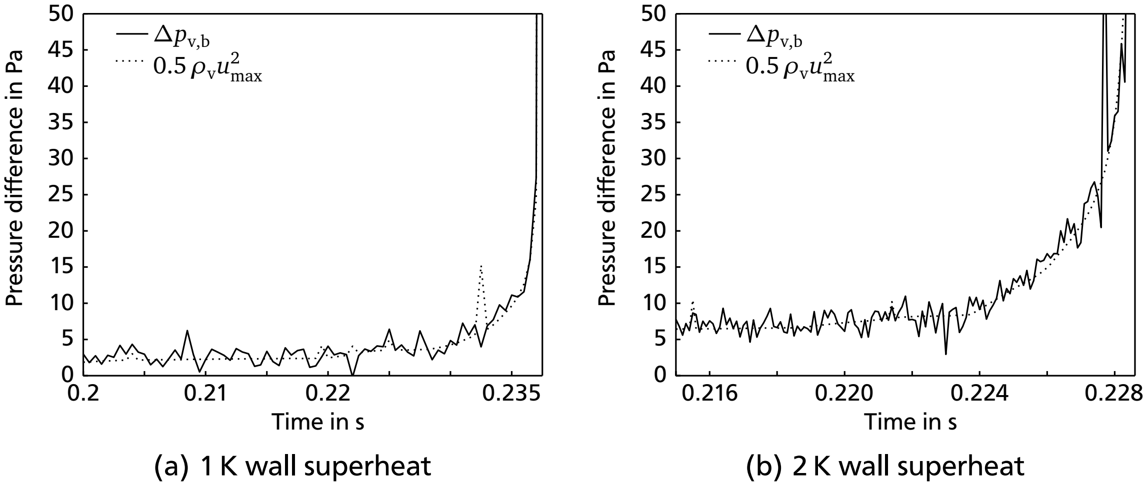

(a) 1 K wall superheat

(b) 2 K wall superheat

Figure 5.9: Pressure difference between vapor in tunnel and bubble

During bubble growth, the pressure difference is for the lower wall superheat $\Delta p_{\mathrm{v,b}} \approx 2\,\mathrm{Pa}$ and for the higher wall superheat $\Delta p_{\mathrm{v,b}} \approx 7\,\mathrm{Pa}$. Right at bubble departure it increases up to $\Delta p_{\mathrm{v,b}} \approx 300\,\mathrm{Pa}$ for both cases. Due to the pressure increase at bubble departure, flow of liquid through the inactive pore actually starts to reverse before bubble departure. Figure 5.9 also gives the dynamic pressure of the flow inside the pore calculated with the maximal flow velocity $p_{\mathrm{dyn}} = 0.5\,\rho_{\mathrm{v}}u_{\mathrm{max}}^2$. By comparing the dynamic pressure and the pressure difference, it becomes obvious that the pressure difference is due to the throttle effect of the pore and not a viscous effect of the vapor flow through the pore. If the pressure loss would be caused by viscous effects, the pressure difference between vapor in the tunnel and bubble $\Delta p_{\mathrm{v,b}}$ would be increased over the dynamic pressure p_{dyn}.

Flow from the pool to the liquid film occurs at the inactive pore through a thin liquid film depicted in Figure 5.10.

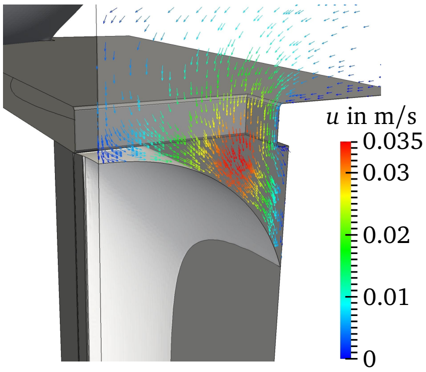

Figure 5.10: Flow through liquid film at inactive pore

The flow resistance depends on the thickness and width of this liquid film. With increasing liquid volume inside the tunnel, the flow resistance consequently decreases because the liquid film thickness increases. The flow resistance is also strongly affected by the shape of the pore. A rectangular pore extending almost completely to the side of the tunnel allows a connection between film and pool also for small amounts of liquid in the tunnel. With corners in the pore, liquid films are also present in the active pore. For the cases studied, liquid flow through the active pore can be neglected during bubble growth compared to the liquid flow at the inactive pore.

As mentioned before, the liquid flow to the tunnel is driven by the pressure difference between liquid pool and film $\Delta p_{\mathrm{l,f}}$. The pressure inside the liquid film is determined by the pressure of the vapor p_{v} and the pressure jump across the liquid-vapor interface $\Delta p_{\mathrm{f,v}}$ in the tunnel. With growing liquid film, the curvature decreases and consequently the pressure difference decreases as well. As shown in Figure 5.8, after reaching a certain volume, the liquid film can reach the symmetry plane of the tunnel. In this case, the curvature of the liquid-vapor interface suddenly increases and is not depending on the film volume anymore. Furthermore, the flow resistance between pool and liquid film is smallest as the pore is completely filled with liquid. Consequently, flow to the liquid film increases until bubble departure or even flooding occurs. If in a case the liquid film is always short from reaching the symmetry plane, a small disturbance might lead to a strong qualitative difference of the boiling process.

In the performed simulations, the pressure difference between vapor inside the bubble and vapor in the tunnel $\Delta p_{\mathrm{v,b}}$ is never high enough to initiate bubble growth at both pores. For pores being of equal shape and size, dynamics after bubble departure determined whether the active pore stayed the same or changed. If the upper part of the tunnel is flooded and the liquid-vapor interface approaches both pores, it is a stochastic process that determines which pore is activated. But also for the case of a small bubble nucleus remaining at the pore, liquid might be flowing fast enough from the liquid film to the pool through the inactive pore such that the bubble is shrinking until the condition is the same at both pores. For the case of the pores being of different size, the bubble always started to grow at the larger pore.

Through the vertical connection of the liquid films, liquid is fed to the lower part of the tunnel. Figure 5.11 shows the evolution of the liquid volume fraction of the upper part of the liquid film and the lower part of the liquid film for the reference case $L_{39}L_{39}$ at 1 K and 2 K wall superheat.

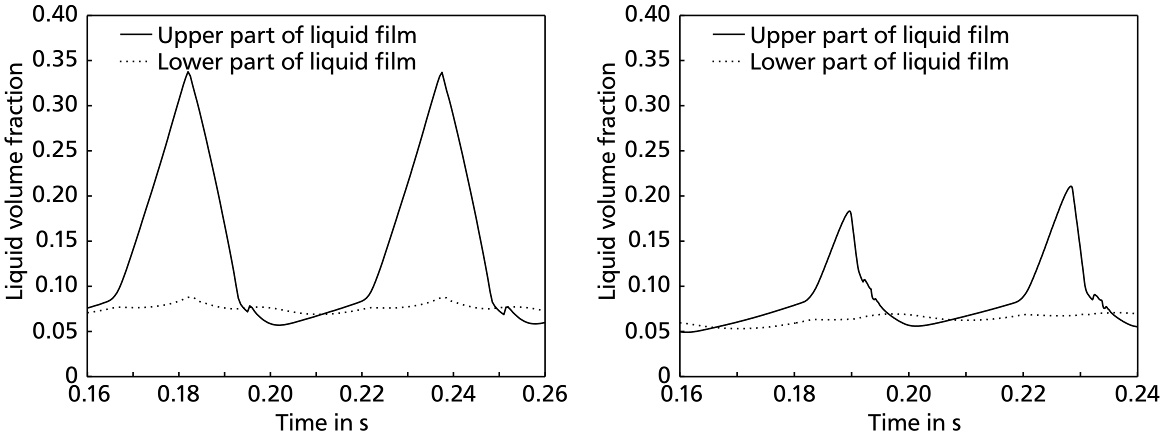

(a) 1 K wall superheat

(b) 2 K wall superheat

Figure 5.11: Volume fraction of upper and lower part of the liquid film, geometry $L_{39}L_{39}$

The fluctuations of the liquid mass inside the tunnel almost exclusively appear in the upper part of the liquid film. Only slight fluctuations can be observed for the liquid volume fraction in the lower part of the tunnel. Furthermore, the amount of liquid in the lower part is reduced compared to the amount of liquid in the upper part.

The larger wall superheat leads to a lower volume of the liquid film compared to the smaller superheat. Increasing the wall superheat leads to an increase of

- contact angle,
- velocity of vapor flowing into the bubble due to an increase in evaporation,
- velocity of liquid flowing from the pool to the tunnel to compensate the evaporative mass flow.

The increasing contact angle decreases the pressure jump across the liquid-vapor interface in the tunnel $\Delta p_{\mathrm{f,v}}$. With vapor velocity, the pressure difference between vapor in the tunnel and the bubble $\Delta p_{\mathrm{v,b}}$ increases. An increase in liquid flow increases the pressure drop between liquid film and pool $\Delta p_{\mathrm{l,f}}$. As a consequence, smaller liquid films are required to increase $\Delta p_{\mathrm{f,v}}$ to counteract these effects in the quasi-steady state. The influence of each of these effects on the process is exemplarily analyzed for the reference case $L_{39}L_{39}$. With a change in tunnel geometry, fluid, heat flux, or pore size, the influence of the single effects will certainly change. The impact of the effects is evaluated through their effect on the pressure.

The reduction of the pressure jump with increasing contact angle is calculated with the help of SURFACE EVOLVER. At a fixed volume fraction of 0.081 the reduction of the pressure jump is $\Delta p_{\mathrm{f,v}}(2\,\mathrm{K}) - \Delta p_{\mathrm{f,v}}(1\,\mathrm{K}) \approx 10\,\mathrm{Pa}$. At a volume fraction of 0.168 the reduction of the pressure jump is $\Delta p_{\mathrm{f,v}}(2\,\mathrm{K}) - \Delta p_{\mathrm{f,v}}(1\,\mathrm{K}) \approx 5\,\mathrm{Pa}$. The increase of the pressure difference between bubble and vapor in the tunnel due to the increase in vapor flow velocity can be taken directly from the CFD simulation. During bubble growth the pressure difference lies at $\Delta p_{\mathrm{v,b}}(2\,\mathrm{K}) - \Delta p_{\mathrm{v,b}}(1\,\mathrm{K}) \approx 5\,\mathrm{Pa}$. For the case $L_{39}L_{39}$, liquid flow to the tunnel is much larger than the evaporating mass flow. As a consequence, an impact of the increase in evaporation of liquid cannot be determined.

For this geometry and wall superheat, the effects of contact angle decrease and vapor velocity increase are about equal. It should be noted that the pressure difference between bubble and vapor in the tunnel scales with the velocity squared such that for smaller pores or larger evaporation rates the influence of this effect will strongly increase. Not accounted for in this analysis is the effect of bubble departure diameter, which will also change with an increase in wall superheat.

In the simulations, it can be observed that the bubble departure diameters not only depend on pore size, shape, and evaporation rate, but also on the volume of the liquid film below the active pore. Bubbles growing above a completely dry tunnel showed significantly larger departure diameters than bubbles growing at a pore, where the pool can connect with the liquid film below the pore. Figure 5.12 shows the bubble departure for the case $L_{19}L_{19}$ at 2 K wall superheat from the left and from the right pore.

Figure 5.12: Bubble departure at pore with film (left) and at dry pore (right), geometry $L_{19}L_{19}$

At the left pore, some liquid is located inside the tunnel and the bubble departs at a diameter of $0.59 \cdot 10^{-3}$ m. The right half of the tunnel is dry and the bubble departs at a diameter of $0.69 \cdot 10^{-3}$ m. As with the single cavity, it is also possible that the liquid film becomes large enough to induce bubble departure.

As was mentioned before, bubble growth has a strong impact on the liquid flow into the tunnel as it determines the pressure of the vapor in the tunnel. If the bubble grows larger, pressure is lower at the end of the bubble cycle than with bubbles departing at small diameters. As a consequence, small bubble departure diameter lead to smaller liquid films in the tunnel. The effect of bubble departure diameter on film growth can be observed by comparing the case $R_{80}R_{80}$ with the reference case $L_{39}L_{39}$ at 1 K wall superheat. Both cases have the same open area between tunnel and pool, but the departure diameter is larger with the circular pore than with the rectangular pore. The evolution of the liquid volume fraction inside the tunnel together with the equivalent diameter of the bubble growing at the pore is depicted in Figure 5.13. For both cases, the liquid film grows with the bubble and after bubble departure about the same amount of liquid is pushed out of the tunnel until the next bubble starts to grow. With the circular pore, the bubble grows larger than with the rectangular pore and consequently the growth phase of the liquid film is longer. After the first bubble cycle the amount of liquid remaining inside the tunnel is so large that during the second bubble cycle the tunnel is flooded.

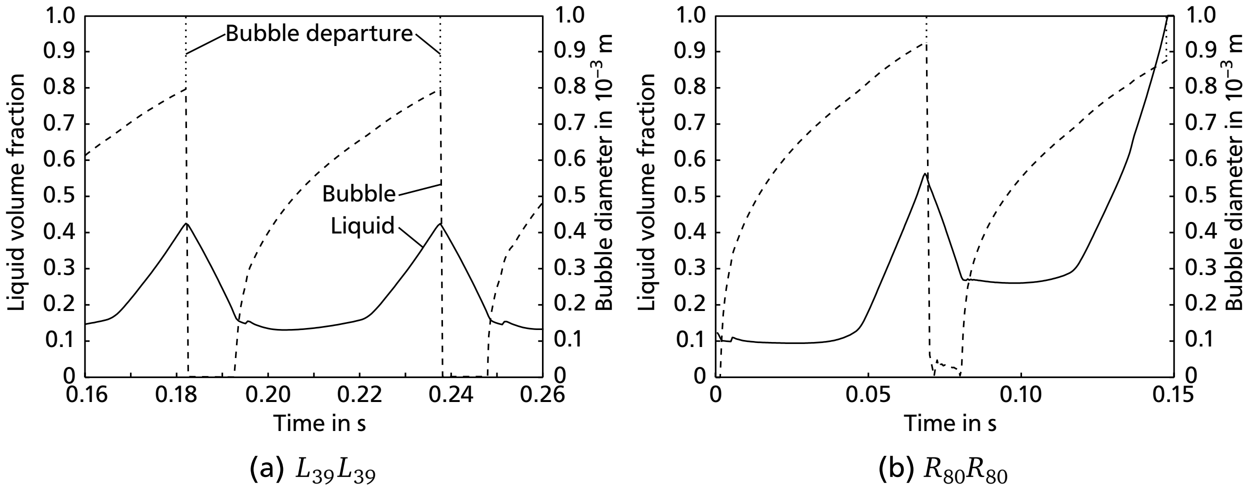

(a) $L_{39}L_{39}$ (b) $R_{80}R_{80}$

Figure 5.13: Liquid volume fraction and bubble diameter

Of course, changing the pore shape also influences the flow resistance for the liquid flowing from the pool to the tunnel, but for the change from the rectangular pore to the circular pore, the flow resistance is assumed to rather increase than decrease for most film volumes.

5.2.1 Influence of geometric properties

As described in the literature review section in Chapter 2, small changes in the geometry of reentrant structured surfaces can have a substantial effect on the heat transfer performance. The size and shape of the tunnel affect the pressure jump across the liquid-vapor interface and the distribution of liquid films inside the tunnel. The pore size and shape influence the flow resistance between the liquid pool and the liquid films in the tunnel, the pressure difference between vapor in the tunnel and bubble, and the bubble departure diameter. In order to study some of the effects potentially leading to the performance change and determine the sensitivity to geometrical changes, slight variations of the geometry are introduced and simulations performed. The geometry changes are visualized in Figure 5.14.

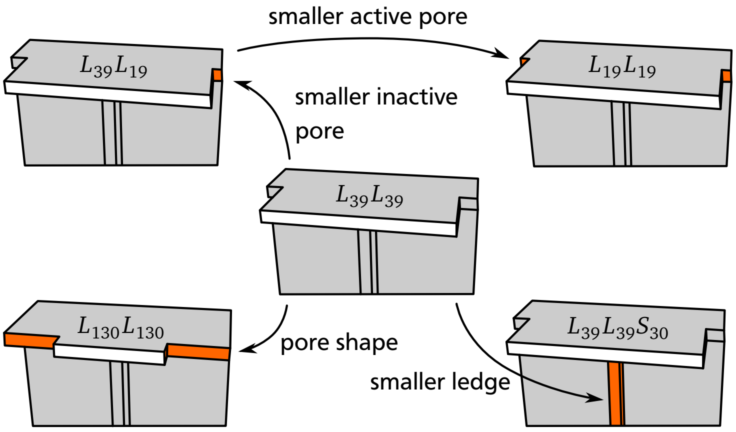

Figure 5.14: Visualization of change of geometries

For the cases studied, the bubble departure diameter together with the minimal and maximal liquid volume fraction during one bubble cycle are given in Table 5.6.

Table 5.6: Liquid volume fraction and bubble departure diameter with changing geometry

Geometry	Wall superheat in K	Volume fraction Minimal	Volume fraction Maximal	Departure diameter in 10^{-3} m
$L_{39}L_{39}$	1	0.131	0.426	0.80
$L_{39}L_{39}S_{30}$ (smaller ledge)	1	0.068	0.311	0.82
$L_{39}L_{19}$ (smaller inactive pore)	1	0.129	0.311	0.83
$L_{19}L_{19}$ (both pores smaller)	1	0.045	0.060	0.61
$L_{39}L_{39}$	2	0.123	0.278	0.87
$L_{39}L_{39}S_{30}$	2	0.042	0.075	0.85
$L_{39}L_{19}$	2	0.076	0.110	0.85
$L_{19}L_{19}$	2	0.006	0.020	0.59 / 0.69
$L_{130}L_{130}$ (different pore shape)	2	0	0	0.84

The variations in the bubble departure diameter are small except for the cases with a smaller active pore $L_{19}L_{19}$. For the case $L_{39}L_{39}$ at 1 K wall superheat, bubble departure is induced by the liquid film growing towards the bubble through the pore. Consequently, the bubble departure diameter is somewhat smaller than for the other two cases with the same active pore size at 1 K wall superheat.

The influence of the shape and size of the inactive pore can be studied by comparing the cases $L_{39}L_{39}$, $L_{39}L_{19}$, and $L_{130}L_{130}$. With $L_{39}L_{19}$ the active pore has the same pore size as $L_{39}L_{39}$, but the inactive pore only has half the open area between pool and tunnel. For $L_{130}L_{130}$, the inactive pore has the same open area and shape, but is not extending towards the wall of the tunnel. Even though the open area is the same for $L_{39}L_{39}$ and $L_{130}L_{130}$, dryout is observed for $L_{130}L_{130}$. Due to the shape of the pore, the connection between liquid film and pool is cut after the liquid film falls below a certain volume and liquid flow into the tunnel during bubble departure is not sufficient to compensate the evaporating liquid mass. With geometry $L_{39}L_{19}$, the liquid film volume is reduced by up to 60 % compared to $L_{39}L_{39}$ for both wall temperatures.

The effect of changing the size of the active pore can be studied by comparing the cases $L_{39}L_{19}$ and $L_{19}L_{19}$. For those two geometries, the inactive pore has the same shape and size. With a smaller active pore size, the liquid film volume strongly decreases inside the tunnel. During bubble growth, it is not reaching the symmetry plane, which explains the even more pronounced difference between the maximal film volumes. The decrease in liquid volume is caused by the decrease of the bubble departure diameter as well as the increase in pressure difference between bubble and vapor in the tunnel due to the smaller vapor flow cross section.

The influence of the size of the solid ledge is evaluated with geometry $L_{39}L_{39}S_{30}$. With decreasing length of the solid ledge, the flow resistance between the upper and the lower liquid film increases and the pressure jump across the liquid-vapor interface decreases. As a consequence, the liquid volume in the tunnel decreases.

The film volume shows the highest sensitivity to the size of the active pore. The effect of changing the size of the inactive pore is smaller than the effect of changing the size of the solid ledge in the tunnel. If the opening to the pool is located only in the middle of the tunnel, the flow resistance changes drastically and dryout occurs. The results show that even rather small changes in geometry can have a substantial effect on the liquid flow into the tunnel.

An additional parameter which is investigated with the case $L_{39}L_{39}H_{400}$, is the depth of the tunnel. By reducing the depth, the curvature of the liquid-vapor interface inside the tunnel increases and the tunnel can hold less liquid. In the simulation, this leads to immediate flooding of the tunnel even at 2 K wall superheat as depicted in Figure 5.15.

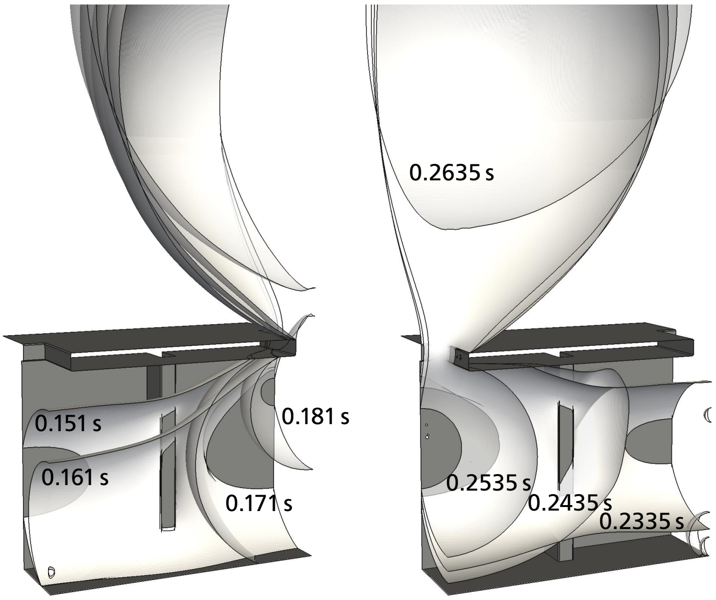

Figure 5.15: First bubble departure and second bubble departure for case with flooding

During bubble growth, the upper and the lower liquid film connect and a vapor tube develops inside the tunnel, which pushes the vapor into the bubble. During the first bubble cycle depicted on the left in Figure 5.15, the bubble exceeds the departure diameter shortly before all of the vapor is removed from the tunnel. Consequently, a vapor nucleus remains inside the tunnel, which starts to grow again. At the second bubble cycle the amount of liquid in the lower part of the film is already increased. During bubble departure the vapor is completely pushed out of the tunnel.

5.2.2 Heat transfer characteristics

With thin liquid films evaporating inside the tunnel, an extremely large heat transfer is observed. The heat transfer coefficients obtained in the suction evaporation mode are given in Table 5.7. Results are presented with two different reference areas for calculating the heat transfer coefficient, the projected or outer area $A_{\mathrm{out}} = 500\,\mu\mathrm{m} \cdot 250\,\mu\mathrm{m} = 0.125\,\mathrm{mm}^2$, which is also usually employed in experiments, as well as the actual area of the wall with the fixed wall temperature boundary condition. For comparison, the heat transfer coefficient for the case with complete dryout is given, too. The observed heat transfer coefficients are on the upper end of the experimentally observed values for tubes with structured surfaces. An interpretation of this observation is given in Chapter 7. By comparing the heat transfer coefficients of the cases $L_{39}L_{39}$, $L_{39}L_{19}$, and $L_{19}L_{19}$, the conclusion can be drawn that thinner films lead to an increase of the heat transfer coefficient.

Unless with geometry $L_{39}L_{19}$, the heat transfer coefficient is slightly decreasing with increasing wall superheat. With an increase in wall superheat, the thickness of the liquid films decreases but the thermal resistance in the vicinity of the three phase contact line increases. Depending on how pronounced the decrease in film volume is, the heat transfer coefficient can increase or decrease. As with the single cavity,

Table 5.7: Heat transfer coefficients

Geometry	Wall superheat in K	h in kW/m^{2}K $A_{\text{ref}} = A_{\text{out}}$	$h_{\Delta T}$ in kW/m^{2}K $A_{\text{ref}} = A_{\Delta T}$	Notes
$L_{39}L_{39}$	1	50	10	
$L_{39}L_{39}S_{30}$	1	53	12	
$L_{39}L_{19}$	1	53	11	
$L_{19}L_{19}$	1	60	12	very thin films
$L_{39}L_{39}$	2	47	10	
$L_{39}L_{39}S_{30}$	2	50	11	
$L_{39}L_{19}$	2	54	11	
$L_{19}L_{19}$	2	38	8	local dryout
$L_{130}L_{130}$	2	5.5	1.1	complete dryout

heat transfer at the three phase contact line plays an important role. The amount of heat transferred within the microzone is between 45 % and 55 % of the total heat transfer.

The heat transfer coefficient with a liquid film being present is about ten times the heat transfer coefficient of the geometry with the dry tunnel. This indicates that evaporation from films inside the tunnel is the most important heat transfer mechanism for the cases studied. The heat transfer coefficient $h_{\Delta T}$ with the actual solid-fluid interface taken as reference area is about five times smaller than the heat transfer coefficient with the projected area taken as reference area. Comparing $h_{\Delta T}$ of the cases with liquid films with h of the geometry with the dry tunnel shows that the increase in heat transfer with a surface with subsurface tunnels is not solely based on an increase in heat transfer area.

For the cases with liquid films located inside the tunnel, sensible heat transfer in the wake of the bubble can be neglected. The heat transfer from the outer wall to the fluid is between 3 % and 7 % of the total heat transfer. It shall be noted that with increasing number of pores, liquid flow velocities on the outer surface will increase and consequently the convective heat transfer as well.

6 Modeling and Analysis of the Interrelation of Important Parameters

From the CFD simulations, the parameters governing the boiling process at the pores can be identified. Due to the immense computational effort, which is required to simulate flow and heat transfer in the subsurface tunnel, the number of parameter combinations that can be investigated is limited. In order to be able to examine a wider parameter range and to improve the understanding of the interrelation of some of the parameters involved, a strongly simplified model is created. Especially conditions leading to dryout and flooding are of interest. The basic idea of the model was presented earlier by the author in [34] and is expanded here further. While in [34] circular cavities with additional channel were studied, the model is applied to subsurface tunnels here.

6.1 Modeling of evaporation and liquid flow

Flow to the tunnel is driven by the pressure difference between the liquid film in the tunnel and the liquid pool. The created model is based on the solution of the Young-Laplace equation to obtain bubble and film shapes and pressures in the vapor and the liquid to calculate the evolution of the film. The model setup is shown in Figure 6.1.

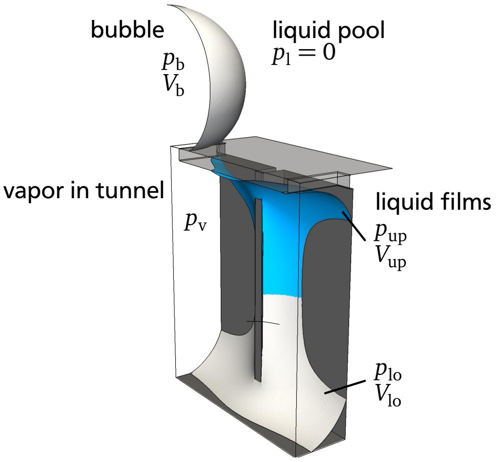

Figure 6.1: Setup for model

The liquid film is split into an upper part and a lower part. Vapor is flowing through the active pore into the growing bubble. Liquid flow to the tunnel through the inactive pore is modeled with a flow resistance $\zeta_{l,up}$.

Heat transfer is not modeled. On real surfaces, the exact heat transfer coefficient is affected by several parameters, while it is generally accepted that it is a requirement to operate in the suction evaporation mode to obtain the highest values for the heat transfer coefficient. As heat transfer is not modeled, the interrelation between contact angle and wall superheat is not incorporated but the contact angle is a free parameter. Furthermore, simplifications regarding flow and bubble growth are introduced.

The main modeling assumptions are that

- liquid inertia can be neglected,
- sensible heat transfer can be neglected,
- all processes are quasi-steady state.

In how far these assumptions apply is discussed in Section 6.1.6.

6.1.1 Bubble growth and liquid flow into the tunnel

Liquid flow into the tunnel is driven by the pressure difference $\Delta p_{\mathrm{l,up}}$ between the liquid pool and the upper liquid film, which is given by Equation (6.1).

$$\begin{aligned} \Delta p_{\mathrm{l,up}} = p_\mathrm{l} - p_\mathrm{up} &= -\Big((p_\mathrm{b} - p_\mathrm{l}) + (p_\mathrm{up} - p_\mathrm{v}) + (p_\mathrm{v} - p_\mathrm{b})\Big) \\ &= -\Big(\Delta p_{\mathrm{b,l}} + \Delta p_{\mathrm{up,v}} + \Delta p_{\mathrm{v,b}}\Big) \end{aligned} \tag{6.1}$$

The pressure difference between the upper liquid film and the lower liquid film is given by Equation (6.2)

$$\Delta p_{\mathrm{up,lo}} = \Delta p_{\mathrm{up,v}} - \Delta p_{\mathrm{lo,v}} \tag{6.2}$$

For each bubble and film volume, the pressure differences $\Delta p_{\mathrm{up,v}}$, $\Delta p_{\mathrm{lo,v}}$, and $\Delta p_{\mathrm{b,l}}$ can be taken from the solution of the Young-Laplace equation. The pressure difference caused by Carnot's shock loss of the dynamic pressure of the vapor flowing at high velocity through the pore, is given by Equation (6.3).

$$\Delta p_{\mathrm{v,b}} = 0.5\,\rho_\mathrm{v} u_{\mathrm{max}}^2 = 2\,\rho_\mathrm{v} \bar{u}^2 = 2\,\rho_\mathrm{v} \left(\frac{\dot{V}_\mathrm{b}}{A_\mathrm{p}}\right)^2 \tag{6.3}$$

In there, the assumption of laminar flow with $u_{\mathrm{max}} = 2\,\bar{u}$ is employed. $\dot{V}_\mathrm{b}$ is the vapor flow rate to the bubble, A_p the open area of the pore, and $\bar{u}$ the average vapor velocity.

The liquid flow through the pore $\dot{V}_\mathrm{p}$ is related to the pressure difference through the flow resistance $\zeta_{\mathrm{l,up}} = \Delta p_{\mathrm{l,up}}/\dot{V}_\mathrm{p}$, with $\dot{V}_\mathrm{p}$ being positive in direction of the liquid pool. Inside the subsurface tunnel, the liquid film is split into two parts, the upper film volume V_{up} connected to the pore and the lower film volume V_{lo} connected only to the upper film volume. Therefore, a flow resistance $\zeta_{\mathrm{up,lo}}$ between the upper and the lower film is required as well. The change in liquid volume of the films can be obtained from the mass balance and is given by Equation (6.4) and (6.5).

$$\dot{V}_{\mathrm{up}} = -\frac{\dot{Q}_\mathrm{f}}{2\,\Delta h_\mathrm{v} \rho_\mathrm{l}} + \frac{\Delta p_{\mathrm{l,up}}}{\zeta_{\mathrm{l,up}}} - \frac{\Delta p_{\mathrm{up,lo}}}{\zeta_{\mathrm{up,lo}}} \tag{6.4}$$

$$\dot{V}_{\mathrm{lo}} = -\frac{\dot{Q}_\mathrm{f}}{2\,\Delta h_\mathrm{v} \rho_\mathrm{l}} + \frac{\Delta p_{\mathrm{up,lo}}}{\zeta_{\mathrm{up,lo}}} \tag{6.5}$$

As given in the simplifying assumptions, the evaporative heat transfer $\dot{Q}_\mathrm{f}$ is the only heat flow considered in the model. The amount of heat transferred at the film is much larger compared to the amount of heat transferred at the bubble foot. Therefore, $\dot{Q}_\mathrm{f}$ is assumed to be approximately equal to the overall evaporation rate. $\dot{Q}_\mathrm{f}$ is split equally between the upper and the lower film. The split of the liquid film into an upper part and a lower part gives a significant improvement over the consideration of only one single liquid film. The introduction of four liquid films by separating the upper and the lower part into a part closer to the active pore and a part closer to the inactive pore gives no further improvement of the results for the calculated geometries.

Assuming the flow into the tunnel is taking place through a thin film at low Reynolds number, the flow resistance ζ can be calculated with the lubrication approximation from the Navier-Stokes equation as given in Equation (6.6) with $C_\zeta = 3$ for a flow with a free surface, film length L, width W, and thickness δ.

$$\zeta = C_\zeta \mu_\mathrm{l} \frac{L}{\delta^3 W} \tag{6.6}$$

Consequently, $\zeta_\mathrm{l,up}$ is a function of the liquid volume in the tunnel and its treatment is discussed in Section 6.1.5. The flow resistance between upper and lower liquid film $\zeta_\mathrm{up,lo}$ is approximated with Equation (6.6) and the dimension of the liquid film in the tunnel as given in Equation (6.7).

$$\zeta_\mathrm{up,lo} = 3\,\mu_l \frac{L_\mathrm{h}/2}{A_\mathrm{f,up,lo}\left(\frac{A_\mathrm{f,up,lo}}{L_\mathrm{f,up,lo}}\right)^2} \tag{6.7}$$

In there, the height of the tunnel L_h, the cross section area of liquid between the upper and the lower film $A_\mathrm{f,up,lo}$, and the length of the line the wetted wall creates at the cross section $L_\mathrm{f,up,lo}$ are employed. Figure 6.2 illustrates $A_\mathrm{f,up,lo}$ as well as $L_\mathrm{f,up,lo}$.

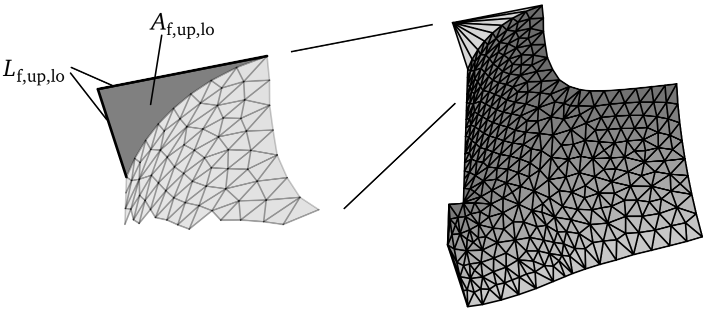

Figure 6.2: Dimensions required for calculating $\zeta_\mathrm{up,lo}$

The volume flow of vapor to the bubble is given by the volume conservation inside the tunnel (6.8).

$$\dot{V}_\mathrm{b} = \frac{\dot{Q}_\mathrm{f}}{\Delta h_\mathrm{v} \rho_\mathrm{v}} + \dot{V}_\mathrm{up} + \dot{V}_\mathrm{lo} \tag{6.8}$$

Once the bubble reaches the maximal volume, its size is reset to the size of the bubble nucleus.

The pressure jump across the liquid-vapor interface at the bubble and at the film is given by the Young-Laplace equation (6.9) for a non-moving interface being in equilibrium. κ_1 and κ_2 are the principal curvatures of the interface.

$$\Delta p = \sigma\left(\kappa_1 + \kappa_2\right) \tag{6.9}$$

6.1.2 Pressure inside the bubble

To obtain the shape of and pressure inside the bubble, Equation (6.9) is parameterized following the approach of Myers and Charpin [92]. The employed coordinate system is given in Figure 6.3. Here, the height h is positive in the direction from the bubble top towards the bubble bottom.

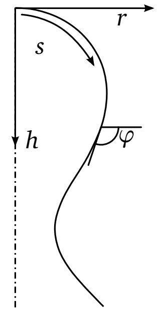

Figure 6.3: Coordinate system for calculation of bubble shape

For an axisymmetric interface, the principal curvatures of a surface can be written as shown in Equation (6.10) (see e.g. Kühnel [71]).

$$\begin{aligned}\kappa_1 &= \frac{1}{\left(r'^2 + h'^2\right)^{3/2}} \left(-r''h' + r'h''\right) \\ \kappa_2 &= \frac{1}{\left(r'^2 + h'^2\right)^{1/2}} \left(\frac{h'}{r}\right)\end{aligned} \tag{6.10}$$

$$r' = \frac{\mathrm{d}r}{\mathrm{d}s} = \cos\varphi \qquad r'' = \frac{\mathrm{d}^2 r}{\mathrm{d}s^2} = -\varphi' \sin\varphi$$

$$h' = \frac{\mathrm{d}h}{\mathrm{d}s} = \sin\varphi \qquad h'' = \frac{\mathrm{d}^2 h}{\mathrm{d}s^2} = \varphi' \cos\varphi \qquad \varphi' = \frac{\mathrm{d}\varphi}{\mathrm{d}s}$$

The pressure difference $\Delta p(h)$ is given by the initial pressure difference Δp_0 at the top of the bubble and the difference in hydrostatic head as shown in Equation (6.11).

$$\Delta p = \Delta p_0 - hg\left(\rho_\mathrm{l} - \rho_\mathrm{v}\right) \tag{6.11}$$

Equation (6.9) together with Equation (6.10) and (6.11) leads to the ordinary differential equation (6.12) describing the bubble shape.

$$\frac{\Delta p_0 - hg\left(\rho_\mathrm{l} - \rho_\mathrm{v}\right)}{\sigma} = \varphi' + \frac{1}{r}\sin\varphi \tag{6.12}$$

The system can be non-dimensionalized with the capillary length $a = \sqrt{\sigma / \left(\left(\rho_\mathrm{l} - \rho_\mathrm{v}\right) g\right)}$, leading to Equation (6.13).

$$\begin{gathered}\Delta p_0^* - h^* = \frac{\mathrm{d}\varphi}{\mathrm{d}s^*} + \frac{\sin\varphi}{r^*} \\ \text{with } \Delta p_0^* = \Delta p_0 \frac{a}{\sigma}, \quad h^* = \frac{h}{a}, \quad s^* = \frac{s}{a}, \quad r^* = \frac{r}{a}\end{gathered} \tag{6.13}$$

The differential equation is solved using a multi-step Adams–Bashford–Moulton method (ode113 in MATLAB). In order to obtain different bubble shapes, the initial value for Δp_0^* is varied. A small value leads to large bubbles and a large value to small bubbles. Bubble growth is calculated individually for each dimensionless pore radius R_p^*. The procedure is illustrated in Figure 6.4. The value for Δp_0^* is

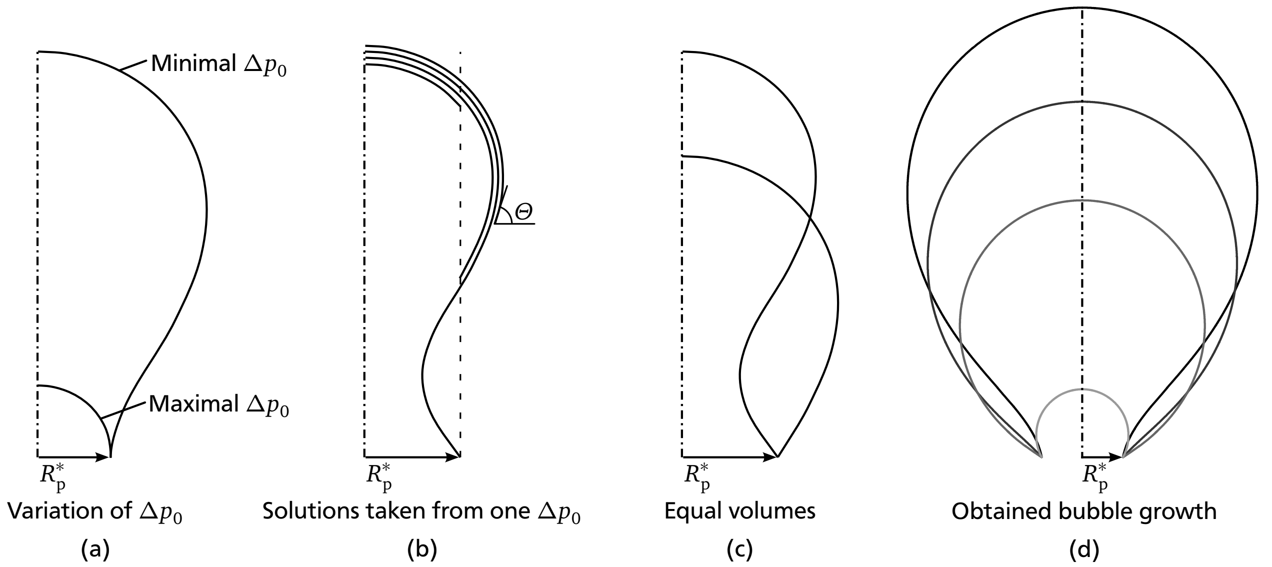

Figure 6.4: Calculation of bubble growth

decreased from the maximal to the minimal Δp_0^* (6.4 (a)). For each solution, the locations where the interface reaches the pore radius, or the contact angle a certain value Θ, are identified (6.4 (b)). From the bubble top to these locations, the bubble volume is saved together with the pressure jump. Afterwards the bubbles are sorted in ascending volume order. Valid solutions are bubbles with the bubble foot having the pore radius and the contact angle being larger than the assigned value Θ, or the bubble foot being larger than the pore radius and the contact angle being equal to Θ. There can exist two solutions of the Young-Laplace equation leading to the same bubble volume (6.4 (c)). For this case, the solution with the smaller surface area is selected, leading to a bubble growth with the interface approaching a contact angle of $\Theta = 90\,\mathrm{deg}$ at the pore from smaller contact angles (6.4 (d)). During bubble departure, some vapor $V_{\mathrm{b,res}}$ remains at the pore. The volume of the remaining bubble is arbitrarily set to the volume of the bubble with the largest pressure difference Δp_0.

With this solution procedure, the departure volume $V_{\mathrm{b,dep}}$ for bubbles growing at a circular pore with radius $R_p^* = R_p/a$ is obtained. The calculated dimensionless volumes are compared with the experimentally determined correlation of Di Bari and Robinson [33]. Figure 6.5 shows the correlation together with the calculated values.

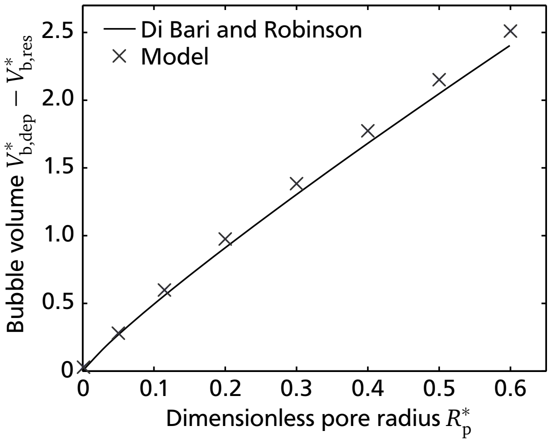

Figure 6.5: Dimensionless bubble departure volumes at circular pores

The resulting departure volumes show a good agreement with the experimental values. It should be noted that the shown correlation is valid for quasi-steady growth only. Bubble growth and pressure differences are calculated for a set of pore radii and contact angles. During calculation of the evolution of the liquid films in the model, the pressure jump at the bubble is calculated for each bubble volume and contact angle, based on an interpolation of the bubble growth results.

With increasing bubble volume, the pressure inside the bubble first increases until the maximal curvature of the liquid-vapor interface is obtained with $\Delta p_{0,\mathrm{max}}$ and afterwards the pressure decreases. Figure 6.6 shows the dimensionless pressure difference $\Delta p^*_{\mathrm{b,l}} = \Delta p_{\mathrm{b,l}}\, a/\sigma$ between bubble and liquid pool over the dimensionless bubble volume for a contact angle of $\Theta = 4\,\mathrm{deg}$ and a contact angle of $\Theta = 46\,\mathrm{deg}$.

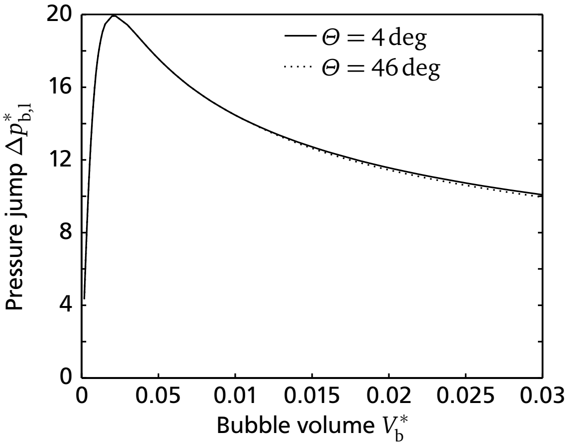

Figure 6.6: Pressure inside bubble with varying contact angle

There is almost no difference in the curves for those two contact angles. The same applies for the bubble departure diameter. This is in agreement with the data of Albadawi et al. [5], which show no difference in bubble departure diameter for contact angles below 60 deg at circular pores.

Figure 6.7 shows the dimensionless pressure difference for three different pore radii.

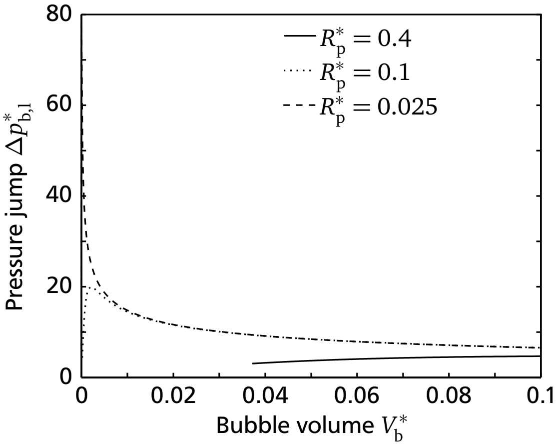

Figure 6.7: Pressure inside bubble with varying pore radius

Once the bubble volume exceeds a certain value, which is approximately given by $V^*_{\mathrm{b}} > 4/3\pi(R^*_{\mathrm{p}})^3$, the pressure curve is very similar to the pressure curves obtained with smaller pore radii and only differ in the bubble departure diameter.

6.1.3 Pressure inside the liquid film

Solving the Young-Laplace equation for the pressure difference across the liquid-vapor interface of the liquid film is not as trivial as for the bubble due to the complex tunnel geometry. In order to find a solution, the software Surface Evolver developed by Brakke [16] is employed. In this software the energy of a surface is minimized. By supplying according formulations for the energy of the liquid-vapor interface, liquid-solid interface, and vapor-solid interface together with boundary and volume constraints, the equilibrium state for a liquid film with given contact angle inside a structure can be calculated. Figure 6.8 shows the different steps in calculating the liquid-vapor interface of a liquid film in the tunnel in Surface Evolver.

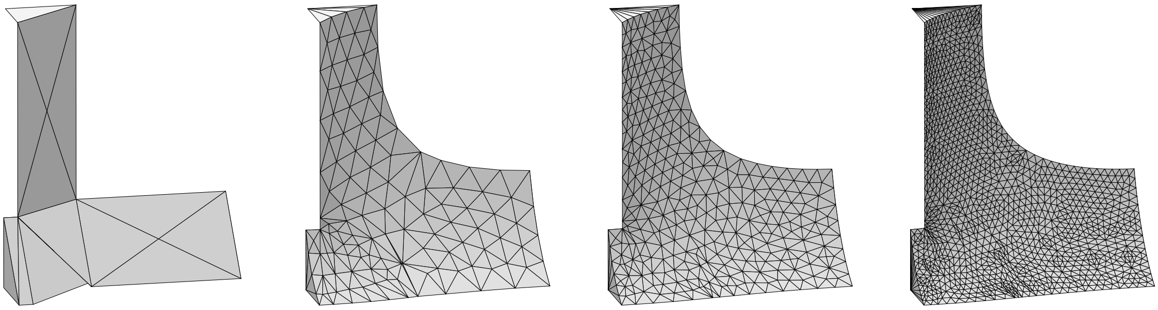

Figure 6.8: Evolution of the liquid film in Surface Evolver

The code that needs to be supplied to the program to obtain this shape is given in Appendix D. From the solution, the liquid volume, pressure difference, as well as geometric properties are known. Again, results are calculated for a set of parameters and an interpolation is performed in the model to obtain the pressure difference with the given film volume.

In the calculation of the film shapes, gravity is neglected due to the assumption of the tunnel being of capillary scale and to be able to employ the results for the upper as well as the lower film. By utilizing the properties of the nondimensional form of the Young-Laplace equation, the liquid properties can be varied without the need to recalculate the dependence of pressure jump on liquid volume and contact angle within Surface Evolver. A recalculation is only necessary if the geometry is not scaled in all dimensions but only single geometric properties are varied.

With growing liquid film inside the structure, the film eventually reaches the symmetry plane in the middle of the tunnel. For this case, a new geometry inside Surface Evolver is required. The growing liquid film reaches the symmetry plane at a certain volume, but due to the change in shape, the shrinking liquid film detaches from the symmetry plane at a smaller volume. This results in a kind of hysteresis of the film pressure within this volume range. For small contact angles, the hysteresis is small or almost vanishing, which is why in the model this hysteresis is not considered. In order to reduce the number of parameters, also the influence of the pore on the film shape is not considered.

6.1.4 Nondimensionalization and full model

The nondimensionalization of the system reduces the number of independent parameters and gives characteristic numbers governing the process. Here, the equations are given for only one liquid film with volume change rate $\dot{V}_\mathrm{f}$ and pressure p_f being modeled such that characteristics of the system are more distinct. The dimensionless form of pressure and the volume change rate is calculated by

$$p^* = p\frac{a}{\sigma},$$
$$\dot{V}_\mathrm{f}^* = \dot{V}_\mathrm{f}\frac{\Delta h_\mathrm{v}\rho_\mathrm{v}}{\dot{Q}_\mathrm{f}}.$$

The full nondimensional model with two liquid films, as it is employed in the calculations, is given in Appendix B.

The dimensionless pressure difference between liquid film and liquid pool $\Delta p_\mathrm{l,f}^*$ can be calculated from Equation (6.14).

$$\Delta p_\mathrm{l,f}^* = -\left(\Delta p_\mathrm{b,l}^* + \Delta p_\mathrm{f,v}^* + \Delta p_\mathrm{v,b}^*\right) \tag{6.14}$$

The pressure differences $\Delta p_\mathrm{b,l}^*$ and $\Delta p_\mathrm{f,v}^*$ are given by Equation (6.15) and (6.16) with the functions $f(\Theta, V^*, \mathrm{geometry})$ being given by the solution of the Young-Laplace equation.

$$\Delta p_\mathrm{b,l}^* = f(\Theta, V_\mathrm{b}^*, \text{pore geometry}) \tag{6.15}$$
$$\Delta p_\mathrm{f,v}^* = f(\Theta, V_\mathrm{f}^*, \text{tunnel geometry}) \tag{6.16}$$

The dimensionless volume change rates, given by Equation (6.4) and (6.5), are written in dimensionless form as in Equation (6.17) and (6.18).

$$\dot{V}_\mathrm{b}^* = 1 + \dot{V}_\mathrm{f}^* \tag{6.17}$$
$$\dot{V}_\mathrm{f}^* = -\rho^* + \frac{\Delta p_\mathrm{l,f}^*}{\dot{Q}^*\zeta^*} \tag{6.18}$$

The dimensionless pressure difference between bubble and vapor in the tunnel is given by Equation (6.19), which results from Equation (6.3).

$$\Delta p_\mathrm{v,b}^* = 2\left(\frac{\dot{V}_\mathrm{b}^*}{A_\mathrm{p}^*}\right)^2 \frac{\left(\dot{Q}^*\right)^2}{N^*} \tag{6.19}$$

The characteristic dimensionless time for one bubble cycle is given by Equation (6.20).

$$\Delta\tau^* = \frac{V_\mathrm{b,dep}^* - V_\mathrm{b,res}^*}{\dot{Q}^*} \tag{6.20}$$

From the equations, the dimensionless parameters governing the system can be extracted and are the

Θ	contact angle,
$N^* = \frac{\mu_\mathrm{l}^2}{\rho_\mathrm{v} a \sigma}$	“viscosity number”,
$\rho^* = \frac{\rho_\mathrm{v}}{\rho_\mathrm{l}}$	density ratio,
$L^* = \frac{L}{a}$	each length of the pore and tunnel geometry,
$A_\mathrm{p}^* = \frac{A_\mathrm{p}}{a^2}$	open pore area,
$\zeta^* = \zeta_\mathrm{l,up}\frac{a^3}{\mu_\mathrm{l}}$	flow resistance,
$\dot{Q}^* = \frac{\dot{Q}_\mathrm{f}\mu_\mathrm{l}}{\Delta h_\mathrm{v}\rho_\mathrm{v} a^2 \sigma}$	heat flow.

The first three parameters represent fluid properties, L^*, A_p^*, and ζ^* depend on geometric properties and $\dot{Q}^*$ is a process parameter. The bubble departure volume $V^*_\mathrm{b,dep}$ can either be taken from the solution of the Young-Laplace equation or be explicitly provided to the system. As at high bubble growth rates, the determination of the bubble departure volume with the Young-Laplace equation is not a valid approach, the bubble departure volume is supplied as a parameter in this work. With the system of equations above, the number of dimensionless parameters could be further reduced by combining $\dot{Q}^*$ and ζ^* and redefining N^*, but for the full system with two films defining $\dot{Q}^*$ and ζ^* separately is more reasonable.

The crossover characteristic observed with reentrant structures is evident in the nondimensional system of equations. Growth of the liquid film is governed by the product of $\dot{Q}^*$ and ζ^*. Consequently, increasing the heat flow has the same effect as increasing the flow resistance in this equation. The pressure difference between vapor in the tunnel and bubble is related to $(\dot{Q}^*/A_\mathrm{p}^*)^2$. Furthermore, in the dimensionless heat flow $\dot{Q}^*$, the product $\rho_\mathrm{v}\Delta h_\mathrm{v}$ appears, confirming its influence on the boiling mode observed in literature.

The flow chart in Figure 6.9 shows the solution procedure for the full model. The model is run until a quasi-steady state condition or flooding or dryout is reached.

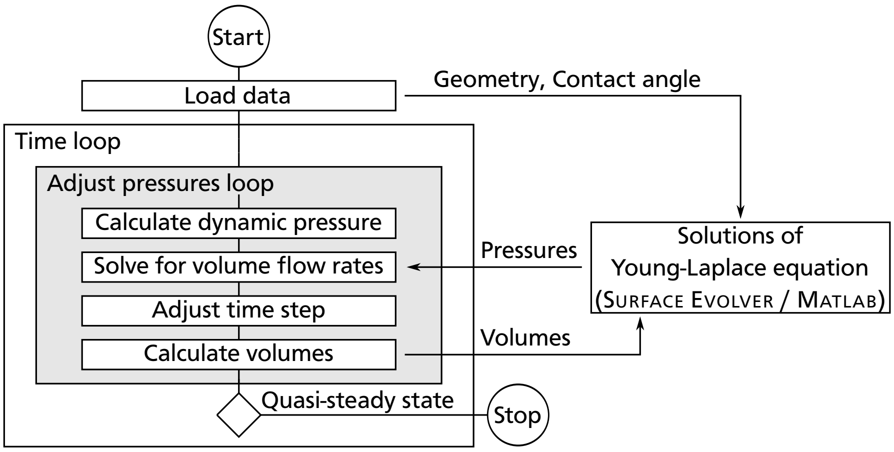

Figure 6.9: Flow chart of full model

6.1.5 Comparison with CFD simulation

The simplified model is compared with the CFD simulations for the reference case $L_{39}L_{39}$ in order to verify the implementation and evaluate its accuracy and applicability. From the simulation results, the heat flow, the bubble departure diameter, and the flow resistance between pool and liquid film are provided as input into the model to allow a comparison.

- The average heat flow is required as it cannot be calculated from the wall superheat in the model.
- The bubble departure volume is adapted to the value observe in the CFD simulation, as no departure volume is calculated in MATLAB for bubbles growing at a rectangular pore. As mentioned before, the pressure plots show a high similarity of the characteristics of the development of the pressure with the bubble volume for different pore radii. The development of the pressure with volume is taken from bubbles growing at a circular pore with radius $R_\mathrm{p} = 75\,\mu\mathrm{m}$, which is the smallest pore with the bubble reaching the departure volume observed in the CFD simulation. Varying the size of the pore up to $R_\mathrm{p} = 150\,\mu\mathrm{m}$ for the pressure data showed no influence on the evolution of the liquid film inside the tunnel. Apparently the influence of the pressure inside the bubble at

the very beginning of bubble growth is small compared to the influence of the bubble departure diameter.

- The flow resistance is adapted until the results fitted best the CFD simulation, which is at a value of $\zeta_{\mathrm{l,up}} = 1 \cdot 10^{10}\,\mathrm{Pa\,s/m^3}$. Afterwards, the influence of $\zeta_{\mathrm{l,up}}$ on the results is studied.

Figure 6.10 shows the evolution of the liquid volume fraction of the lower part of the film $V_{\mathrm{lo}}/V_{\mathrm{tun}}$ and the upper part of the film $V_{\mathrm{up}}/V_{\mathrm{tun}}$ in comparison with the results of the CFD simulation. The sensitivity of the overall liquid volume fraction in the tunnel on the flow resistance $\zeta_{\mathrm{l,up}}$ is presented in Figure 6.11.

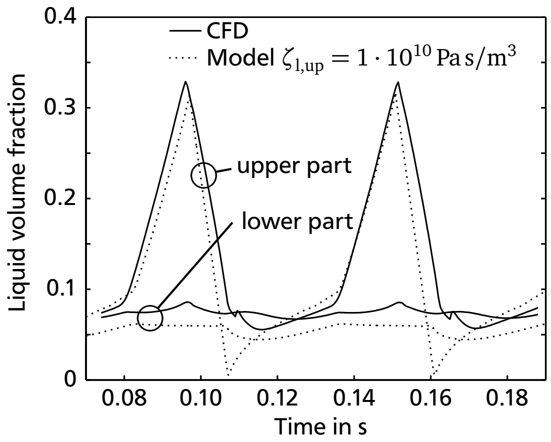

Figure 6.10: Comparison CFD with model

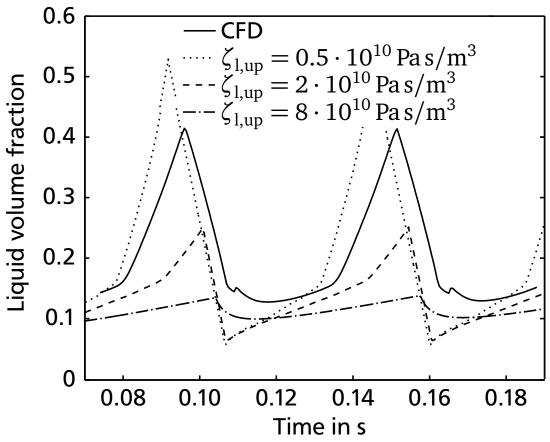

Figure 6.11: Influence of flow resistance $\zeta_{\mathrm{l,up}}$

The comparison shows that the model can capture the steadiness of the lower film, while the amount of liquid in the lower film part is somewhat smaller than in the CFD simulation. During bubble growth and departure, the evolution of the upper liquid film is equal for the model and the simulation, but more liquid is pushed out of the tunnel with the model at the beginning of bubble growth. The explanation for this behavior is a change in flow resistance with the decrease in liquid volume, which is not captured by the model.

Figure 6.11 shows that taking double or half the value for $\zeta_{\mathrm{l,up}}$ changes the maximal film volume inside the tunnel, but hardly affects the minimal film volume during one bubble cycle. As can be taken from Figure 6.10, the minimal film volume is determined by the amount of liquid in the lower part of the tunnel, as the liquid in the upper part is almost completely pushed out of the tunnel. At a value of $\zeta_{\mathrm{l,up}} = 8 \cdot 10^{10}\,\mathrm{Pa\,s/m^3}$, the upper part of the liquid film is not completely pushed out anymore. Comparing the results with the CFD simulation, it becomes obvious how the flow resistance changes in the simulation. While the inflow of liquid at the higher volume fraction is best modeled with $\zeta_{\mathrm{l,up}} = 1 \cdot 10^{10}\,\mathrm{Pa\,s/m^3}$, a value of $\zeta_{\mathrm{l,up}} = 8 \cdot 10^{10}\,\mathrm{Pa\,s/m^3}$ at the low volume fractions is more appropriate.

By estimating the flow resistance $\zeta_{\mathrm{l,up}}$ from liquid volume and geometric properties, this effect could be incorporated, but the model would lose much of its generality and additional parameters would be required to be studied. For each pore shape and size, individual functions $\zeta_{\mathrm{l,up}} = f(V_{\mathrm{up}})$ would have to be obtained. As will be shown in the parametric study, the fluctuations of the liquid volume are much lower for most parameters than for the case for which the comparison with the CFD simulation is drawn. For surfaces with more than one active pore they probably vanish almost completely. Therefore, a constant value for $\zeta_{\mathrm{l,up}}$ is employed in the parameter variations.

6.1.6 Evaluation of the assumptions and limits of the model

Modeling of liquid flow and bubble growth is based on assumptions that limit the application range of the model. The pressure jump across the liquid-vapor interface at the bubble is solely determined based on the Young-Laplace equation, sensible heat transfer is neglected, and an uniform heat flux is assumed. From analysis of the results of the CFD simulations it is known that these are valid assumptions for the parameter range examined in the simulations. It is obvious that these assumptions become more inaccurate with increasing heat flux.

By neglecting liquid inertia, additional forces at the bubble like the drag of the bubble in the liquid, inertia of the liquid surrounding the bubble, or lift forces of bubbles departing beforehand and in the surrounding are not included in calculating the pressure jump across the liquid-vapor interface. Klausner et al. [63], Zeng et al. [143], as well as Ramaswamy et al. [103] analyzed forces acting on a growing bubble. From their approach, the dynamic effects of bubble growth on the pressure of the surrounding liquid can be summarized as shown in Equation (6.21).

$$\Delta p_{\mathrm{dyn}} = \rho_{\mathrm{l}} \left(C_1 \dot{R}^2 + C_2 \ddot{R} R \right) \tag{6.21}$$

Δp_{dyn} is the pressure difference between the liquid at the liquid-vapor interface of the bubble and the liquid at rest in the pool. Just like $\Delta p_{\mathrm{v,b}}$, Δp_{dyn} would be added to the pressure difference $\Delta p_{\mathrm{l,f}}$ between liquid film and pool. R is the bubble radius at an instance of time. Following the reasoning presented in Appendix C, Equation (6.21) can be rewritten in nondimensional form as given in Equation (6.22).

$$\Delta p^*_{\mathrm{dyn}} = C^* \left(\frac{\dot{V}^*_{\mathrm{b}}}{\pi (R^*)^2} \right)^2 \frac{\left(\dot{Q}^*\right)^2}{\rho^* N^*} \tag{6.22}$$

The factor C^* depends on bubble shape, empirical factors introduced in the force models, and the relation between growth velocity and acceleration. Depending on which effects are considered and which bubble shape is provided, the obtained value ranges from $C^* = -0.125$ to $C^* = 2$, assuming a constant bubble growth rate $\dot{V}^*_{\mathrm{b}}$. Dividing $\Delta p^*_{\mathrm{dyn}}$ by $\Delta p^*_{\mathrm{v,b}}$, which the model accounts for, gives relation (6.23).

$$\frac{\Delta p^*_{\mathrm{dyn}}}{\Delta p^*_{\mathrm{v,b}}} = \frac{C^*}{2\rho^*} \left(\frac{A^*_{\mathrm{p}}}{\pi (R^*)^2} \right)^2 \tag{6.23}$$

It is apparent that $\Delta p^*_{\mathrm{dyn}}$ is of the same form as $\Delta p^*_{\mathrm{v,b}}$ and increases or decreases with heat flow just as $\Delta p^*_{\mathrm{v,b}}$ does. With $\pi(R^*)^2$ being the projected area of the bubble, Equation (6.23) shows that the influence of the dynamic forces is highest at the beginning of bubble growth. Due to the constant vapor flow rate, the time the bubble has a small radius is much shorter than the time the bubble has a large radius, but still, $\Delta p^*_{\mathrm{dyn}}$ can be as large as or even larger than $\Delta p^*_{\mathrm{v,b}}$ depending on the value of ρ^* and C^*.

Therefore, it should be reasonable to conclude that once $\Delta p^*_{\mathrm{v,b}}$ starts to dominate the pressure difference between liquid film and pool (compare Equation (6.14)), $\Delta p^*_{\mathrm{dyn}}$ has a substantial effect on the pressure difference as well. As the pressure differences $\Delta p^*_{\mathrm{dyn}}$ and $\Delta p^*_{\mathrm{v,b}}$ are of the same form, the parameter A^*_{p} can be taken to control the influence of dynamic forces in general. Under the assumption that $\Delta p^*_{\mathrm{dyn}}$ can be treated as an average additional pressure difference between liquid and bubble and C^* is constant, the qualitative change of the behavior of the system should not be altered by the additional forces. Instead, A^*_{p} can only be converted back to the dimensioned cross section of the pore if C^* is known.

Liquid inertia is also neglected for the flow of the liquid through the pore and inside the tunnel. The highest liquid flow velocity is obtained in the pore between the liquid pool and the tunnel. The Reynolds number for the liquid flow through the pore can be approximated as shown in Equation (6.24). The derivation is shown in Appendix C.

$$Re_{\mathrm{p}} = \frac{\dot{Q}^*}{N^* R_{\mathrm{p}}^*} \tag{6.24}$$

As long as the Reynolds number is well below unity, inertia effects are small. This is the case for all parameter combinations studied in this work.

In the model, sensible heat transfer from the outer surface is assumed to be negligible. The numerical simulations show that this holds true as long as only a single bubble grows in the computational domain. On tubular surfaces, several bubbles depart and rise along the surface. In the study of Chien and Webb [25], the ratio of sensible heat transfer to total heat transfer was estimated to range from 0.38 to 0.65 at low heat fluxes and 0.8 to 0.9 at the highest heat flux. Nakayama et al. [93] observed ratios of 0.1 at low heat flux and a ratio of 0.75 at a high heat flux. Chen et al. [22] calculated the ratio of sensible heat transfer to lie between 0.35 and 0.65. From the data found in literature it can be concluded that sensible heat transfer cannot be neglected when calculating heat transfer coefficients on real surfaces. In order to compare the results of the model calculated with the dimensionless heat flux $\dot{Q}^*$ with experimental results at the same heat flux, the external heat flux needs to be calculated.

To determine the evaporation rate of the liquid film in the tunnel, the heat transfer rate is split equally between the lower part of the tunnel and the upper part of the tunnel. This implies the assumption that the wall superheat is approximately constant and the heat transfer coefficient of the upper film is equal to the coefficient of the lower film. Depending on heat transfer coefficient h and thermal conductivity of the wall k_{s}, the temperature difference in the wall ΔT_{h} in relation to the wall superheat ΔT can be estimated. Given the most conservative assumption that all the heat needs to be conducted through the wall of the tunnel to the outer surface, the relation of temperature differences can be approximated according to Equation (6.25).

$$\frac{\Delta T_{\mathrm{h}}}{\Delta T} = \frac{h L_{\mathrm{h}}}{k_{\mathrm{s}}} \frac{A_{\mathrm{out}}}{A_{\mathrm{h}}} \tag{6.25}$$

The area A_{out} is the outer (projected) surface area of the structure, A_{h} is the cross section area of the solid connecting the bottom of the tunnel with the top of the tunnel. Table 6.1 gives some estimated wall temperature differences calculated with values found in literature.

Table 6.1: Approximated temperature difference in the solid

Reference	Wall material	h in kW/m^{2}K	$\frac{A_{\mathrm{h}}}{A_{\mathrm{out}}}$	L_{H} in 10^{-6} m	$\frac{\Delta T_{\mathrm{h}}}{\Delta T}$
Chien and Webb [28]	copper $k_{\mathrm{s}} = 401\,\mathrm{W/mK}$ [39]	15	0.48	600	0.047
Chen et al. [23]	steel $k_{\mathrm{s}} \approx 55\,\mathrm{W/mK}$ [39]	30	0.41	700	0.93

From the table it can be concluded that for a steel tube the temperature difference across the tunnel height can be as large as the wall superheat. For a copper surface, the temperature difference is negligible for the heat transfer coefficients obtained.

Considering the error introduced through neglecting the sensible heat transfer and the rather rough modeling of the flow resistance between upper and lower liquid film, the error resulting from the assumption of a constant wall superheat is probably insignificant if a copper wall is presumed.

The assumption of the processes being quasi-steady state should be fulfilled if the fluctuation of the wall superheat is small during one bubble cycle. In the numerical simulation, the heat flux is steady except during bubble departure where it fluctuates by about 7 % for geometry $L_{39}L_{39}$ at 2 K wall superheat. The time slot for this fluctuation is $\Delta\tau \approx 5\,\mathrm{ms}$. From Equation (6.26) the temperature fluctuation $\Delta(\Delta T)$ resulting from this heat flux fluctuation can be estimated.

$$\Delta q A_{\mathrm{out}} \Delta\tau = A_{\mathrm{h}} L_{\mathrm{h}} \rho_{\mathrm{s}} c_{\mathrm{s}} \Delta\left(\Delta T\right) \tag{6.26}$$

For solid properties of copper, the resulting temperature fluctuation is $\Delta(\Delta T) \approx 0.03\,\mathrm{K}$, which is small compared to the wall superheat.

Even though the model is not able to capture all the dynamic effects observed in the CFD and in experiments, comparing the model results with the numerical simulations gives valuable hints on important processes. The model can be used to extract general interrelations between geometric properties and the flow from and to the tunnel for low heat fluxes, with a much lower computational effort.

6.2 Parametric study for subsurface tunnel with two pores

The results of the parametric study are presented in nondimensional form. Variations of single parameters are performed based on the setup of the case $L_{39}L_{39}$. Figure 6.12 shows the minimal and maximal film volume observed during one bubble cycle for varying heat flux with the geometry and settings of the CFD simulation with $L_{39}L_{39}$. The dimensionless numbers for this case are given in Table 6.2.

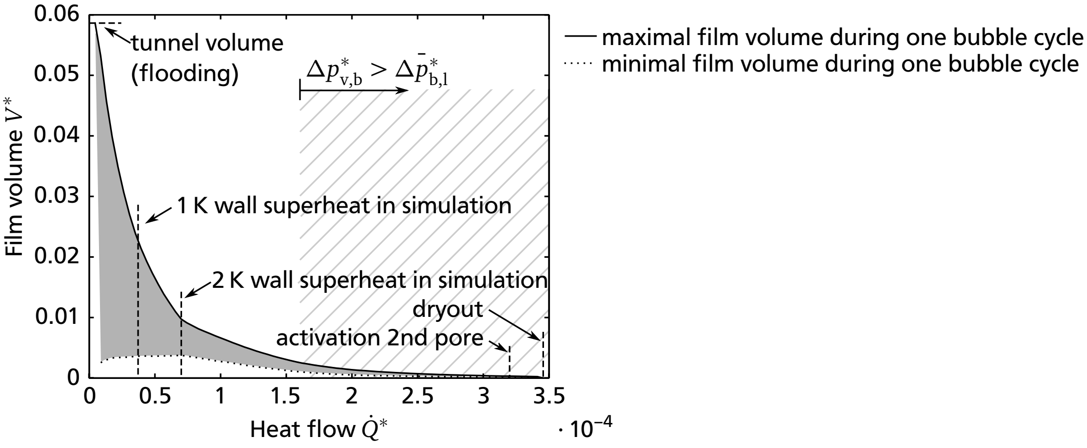

Figure 6.12: Liquid film volume, settings of $L_{39}L_{39}$

Table 6.2: Dimensionless numbers for reference case

N^*_{ref}	ρ^*_{ref}	Θ_{ref}	$A^*_{\mathrm{p,ref}}$	ζ^*_{ref}	$V^*_{\mathrm{b,dep,ref}}$	$L^*_{\mathrm{h,ref}}$	$L^*_{\mathrm{tun,ref}}$
$2.00 \cdot 10^{-4}$	$2.27 \cdot 10^{-2}$	18.51 deg	$2.65 \cdot 10^{-2}$	$3.18 \cdot 10^{4}$	$4.0 \cdot 10^{-1}$	$6.54 \cdot 10^{-1}$	$3.21 \cdot 10^{-1}$

In the graph the dimensionless heat flow obtained in the CFD at 1 K wall superheat as well as at 2 K wall superheat are marked. Furthermore, the point of flooding and dryout of the tunnel are given. At approximately $\dot{Q}^* = 1.6 \cdot 10^{-4}$ the pressure difference $\Delta p^*_{\mathrm{v,b}}$ between vapor in the bubble and vapor in the tunnel becomes larger than the average pressure jump at the liquid-vapor interface of the bubble

$\Delta \bar{p}^*_{\mathrm{b,l}}$. From there on, dynamic forces most likely prevail and, as was demonstrated in Section 6.1.6, the uncertainty in the model increases. To illustrate this, the area beyond this point is shaded. At a heat flow of $\dot{Q}^* = 3.2 \cdot 10^{-4}$ the pressure difference $\Delta p^*_{\mathrm{v,b}}$ is larger than the difference between the maximal value for the pressure jump across the liquid-vapor interface at the bubble and the pressure jump at bubble departure $\Delta p^*_{\mathrm{b,l,max}} - \Delta p^*_{\mathrm{b,l,dep}}$. Therefore, at this point the second pore is activated at latest. With a geometry with only two pores this certainly leads to dryout, as ζ^* increases drastically. The dryout based on the assumption that the flow resistance is constant appears only shortly after the activation of the second pore.

As observed in the CFD simulation, the volume fluctuations are large at low heat flow and become small at a large heat flow. With small $\dot{Q}^*$ the timescale for bubble growth is much larger than the time scale for flow to the liquid film. Therefore, the liquid film curvature follows closely the bubble curvature and large amounts of liquid get sucked in or pushed out. For the case that the tunnel is large enough for the curvature of the liquid film to obtain the curvature of the bubble at departure, no flooding can occur even at low heat flows.

Figure 6.12 is the result for a flow resistance of $\zeta^* = \zeta^*_{\mathrm{ref}} = 3.18 \cdot 10^4$, which is the equivalent value of $\zeta_{\mathrm{l,up}} = 1 \cdot 10^{10}\,\mathrm{Pa\,s/m^3}$ in dimensioned form. Figure 6.13 shows the results for varying ζ^* and Figure 6.14 for varying Θ. According to the microzone model for R134a at $T_{\mathrm{sat}} = 20\,^\circ\mathrm{C}$ the contact angle $\Theta = 10\,\mathrm{deg}$ is obtained with a wall superheat of $\Delta T = 0.2\,\mathrm{K}$ and the contact angle $\Theta = 30\,\mathrm{deg}$ with a wall superheat of $\Delta T = 4.7\,\mathrm{K}$.

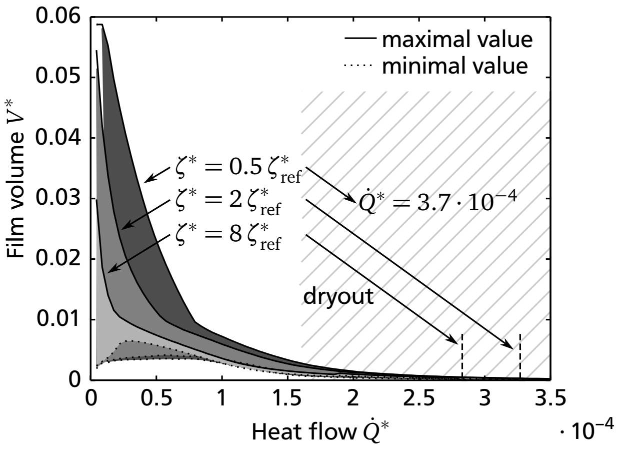

Figure 6.13: Variation of ζ^*

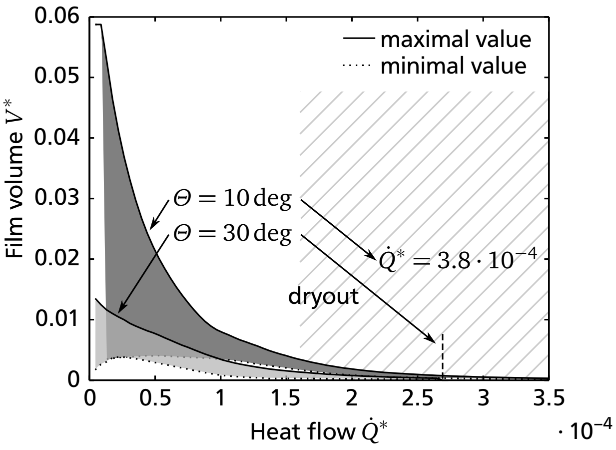

Figure 6.14: Variation of Θ

As shown before, the fluctuation of the liquid volume of the film in the tunnel decreases with increasing flow resistance. At low heat flows the maximal film volume decreases and the minimal film volume increases. Furthermore, dryout occurs earlier with larger flow resistance. For $\zeta^* = 8\,\zeta^*_{\mathrm{ref}}$ dryout occurs before the second pore would be activated, as observed in the CFD simulation for $L_{130}L_{130}$ or partially for $L_{19}L_{19}$.

Increasing the contact angle Θ also decreases the fluctuations and leads to an earlier dryout. Opposed to increasing ζ^*, both, the maximal and the minimal film volume decreases with an increase in Θ. For the larger contact angle, flooding of the tunnel is not possible as the liquid-vapor interface inside the tunnel can obtain the same curvature as the bubble during departure. It shall be noted that, depending on the heat transfer characteristics of the surface, changing the heat flow would also change the contact angle. But as the heat transfer coefficient can increase strongly at low heat fluxes, the change in contact angle might be small, justifying the separation of the influence of contact angle and heat flow here.

Increasing or decreasing the size of the active pore A_p^* increases or decreases the influence of dynamic effects and can change the bubble departure diameter. Figure 6.15 and Figure 6.16 show the influence of those effects on the evolution of the liquid volume separately. In Figure 6.15, the shaded area needs to be adapted according to the value of A_p^*.

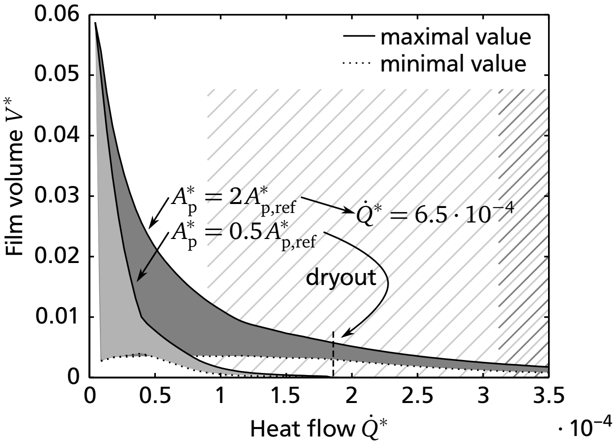

Figure 6.15: Variation of A_p^*

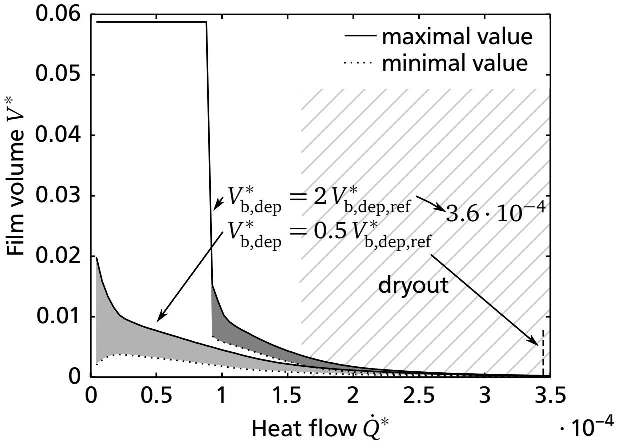

Figure 6.16: Variation of $V_\mathrm{b,dep}^*$

Figure 6.15 shows a strong dependence of the point of dryout on the size of the active pore. Flooding is not affected by this parameter. It appears like the graph is compressed to smaller values of $\dot{Q}^*$ with smaller active pore area A_p^*. Increasing the bubble departure volume $V_\mathrm{b,dep}^*$ leads to flooding of the tunnel at larger values of $\dot{Q}^*$, while the point of dryout is only slightly affected. A decrease of $V_\mathrm{b,dep}^*$ reduces the fluctuations of the liquid mass at low values of $\dot{Q}^*$ and prevents flooding.

The height and width of the tunnel affect the maximal liquid volume the tunnel can hold as well as the pressure inside the liquid film. Results for a variation of tunnel height L_h^* and tunnel width L_tun^* are shown in Figure 6.17 and Figure 6.18, respectively.

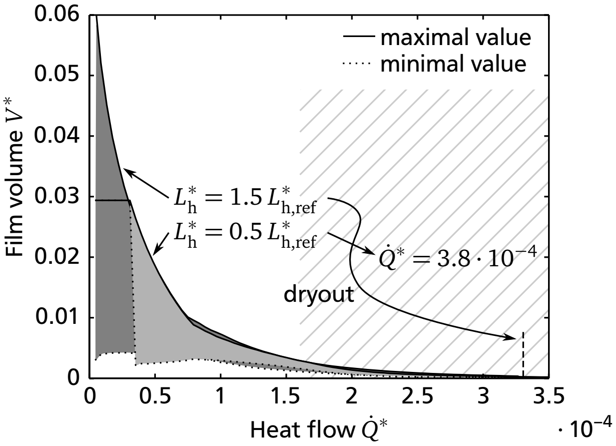

Figure 6.17: Variation of tunnel height L_h^*

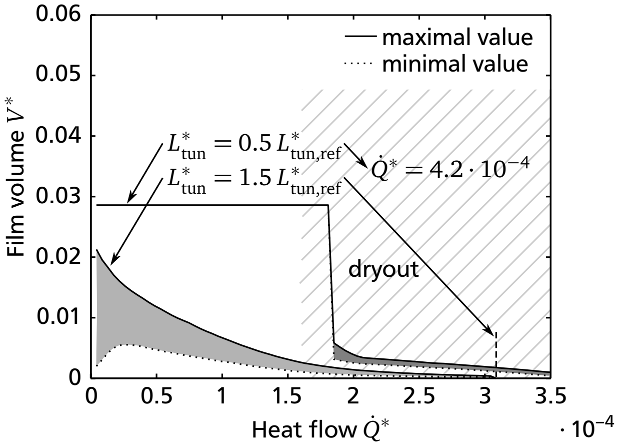

Figure 6.18: Variation of tunnel width L_tun^*

The tunnel height only affects the point of flooding and dryout, while the minimal and maximal film volume stay almost the same in-between. Apparently, the effect of changing the amount of liquid that can be hold by the tunnel is larger than the effect on the pressure jump across the liquid-vapor interface in this parameter range. Opposed to that, decreasing the width of the tunnel strongly increases the pressure jump and consequently more liquid is flowing into the tunnel. This effect, combined with the smaller tunnel volume, leads to early flooding and slightly later dryout.

Based on the parametric study, a “good” and a “bad” setup are created to demonstrate how the combination of properties can lead to cases with the suction evaporation mode existing for a wide range or for an extremely short range of heat flows. The dimensionless numbers for the cases are given in Table 6.3. The numbers not given in the table are the same as in the reference case. Figure 6.19 gives the film volume for those two cases.

Table 6.3: Dimensionless numbers for “good” and “bad” setup

	Θ	A_p^*	ζ^*	$V_\mathrm{b,dep}^*$	L_h^*
“good” setup	10 deg	$2A_\mathrm{p,ref}^*$	$0.5\,\zeta_\mathrm{ref}^*$	$0.5\,V_\mathrm{b,dep,ref}^*$	$2\,L_\mathrm{h,ref}^*$
“bad” setup	30 deg	$0.5A_\mathrm{p,ref}^*$	$8\,\zeta_\mathrm{ref}^*$	$2\,V_\mathrm{b,dep,ref}^*$	$0.5\,L_\mathrm{h,ref}^*$

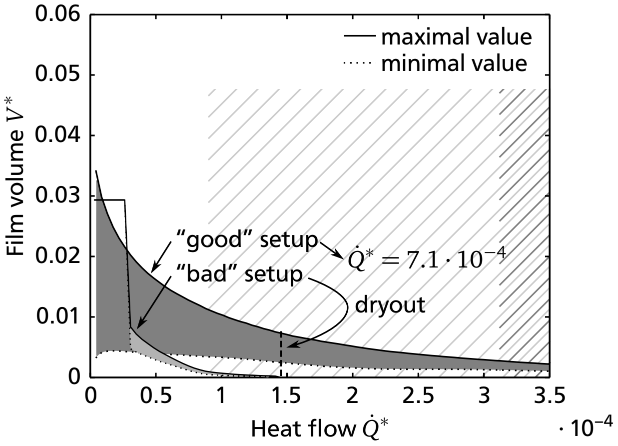

Figure 6.19: Combination of parameters leading to short and large range of suction evaporation mode

The suction evaporation mode for the “bad” setup is extremely small. The shallow tunnel together with the large bubble departure diameter leads to early flooding. The small cross section area of the pore and the large contact angle to early dryout. Opposed to that, the suction evaporation mode extends to large values of $\dot{Q}^*$ and flooding is prevented with the “good” setup.

It should be noted that the dimensionless numbers showed here are no suggestion for designing a reentrant structure on a tube as the model only applies to the setup shown in the CFD simulation. Additional effects that need to be considered with a tubular surface are discussed in Chapter 7. Furthermore, by changing one geometric property, several dimensionless parameters can be affected. For example, changing the pore size affects the bubble departure diameter and the flow resistance as well. The influence of the dimensionless parameters on the boiling process is further discussed in Chapter 7.

7 Conclusions Regarding Reentrant Type Structured Surfaces

In this chapter, the findings of the numerical simulations and analysis are discussed with regard to realistic structures and subsurface tunnels employed with tubular surfaces. The observed processes within the structures are interpreted and the implications for the design of a boiling surface given. Finally, suggestions are given concerning modeling approaches aiming at optimization and prediction of heat transfer with reentrant type structured surfaces.

7.1 Processes within reentrant cavities and subsurface tunnels

The numerical simulations presented in Chapter 4 show that with perfect circular reentrant cavities, processes occurring within an activated cavity during boiling probably do not affect heat transfer if the pore diameter is significant smaller than the bubble departure diameter. Hutter et al. [48] came to the same conclusion for cylindrical cavities. If the pore diameter approaches the scale of the bubble departure diameter, additional effects can occur inside the cavity influencing heat transfer and the boiling process. Due to repeated flooding of the cavity, boiling might not be very stable. After flooding, with a new bubble growing inside the structure, heat transfer can be increased as thin films evaporate inside the structure. Such a process was also observed in the numerical simulations of Lee and Son [75] for multi step cavities.

With square cavities connected through square or rectangular pores to the liquid pool, liquid can flow into the cavity during bubble growth and bubble departure. This should be considered if such a kind of cavity is employed to create nucleation sites. The simulations with single cavities show that in order to obtain the suction evaporation mode for a larger range of heat fluxes, separate openings for bubble growth and liquid flow from the pool to the cavity are required. Therefore, structures consisting of an array of single reentrant cavities are probably less suitable as structures with connected cavities or subsurface tunnels to enhance boiling heat transfer. Furthermore, corners located within the cavity are beneficial to obtain a large area covered by thin films and a long three phase contact line, as was also observed experimentally with subsurface tunnels.

For the subsurface tunnels, numerical simulations, just as experiments, suggest that thin film evaporation during the suction evaporation mode is the most effective heat transfer mechanism. A high heat transfer coefficient is obtained if thin liquid films exist in the corners of the tunnel and the three phase contact line is elongated. If vertical structures are present in the tunnel, liquid can be fed from the upper to the lower liquid corner.

From visualization studies, Chien and Webb [29] concluded that within the subsurface tunnel there can exist parts that are flooded and parts that are operated in the suction evaporation mode at the same time. Nakayama et al. [93] observed in the initial stage of boiling a vapor bubble expanding inside the tunnel. The numerical simulations show that partial dryout can occur decreasing the heat transfer coefficient but not immediately leading to a complete dryout of the tunnel. From this, the concept of the boiling modes can be extended by dividing the suction evaporation mode into sub-stages as illustrated in Figure 7.1. In the vapor expansion stage, parts of the tunnel are operated in the suction evaporation mode with thin

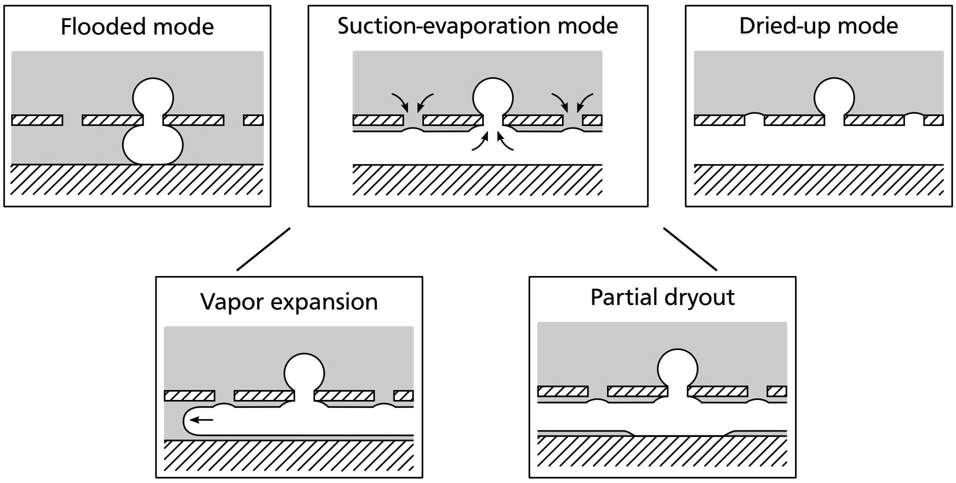

Figure 7.1: Additional stages in the suction evaporation mode

film evaporation in the corners, while other parts of the tunnel are flooded. With increasing heat flux, the fraction of the tunnel being flooded decreases. In the partial dryout stage, liquid supply to some parts of the thin films located in the corners of the structure is not sufficient to balance evaporation. Partial dryout can occur also with the vapor region expanding inside the tunnel such that the two stages appear simultaneous.

Surfaces showing a decreasing heat transfer coefficient with increasing heat flux, as observed for example by Ribatsky and Thome [104], are probably affected by partial dryout. The increasing heat transfer coefficient with heat flux observed with other surfaces can be caused by the increase in forced convection on the outer surface as well as an increase in area operated in the suction evaporation mode in the vapor expansion stage. In the numerical simulations, heat transfer coefficients are obtained which are at the upper end of the experimentally observed values. As in experiments a larger portion of the heat is furthermore transferred by convection on the outer boundaries of the structure, there are two possible explanations for this observation. First, there are less vertical connections in the tunnels increasing the film area with industrial tubes than in the CFD geometry. Second, the full subsurface tunnel is never completely operated in a perfect suction evaporation mode, but partial dryout or partial flooding always are present in some parts of the tunnel.

The numerical simulations show that in the suction evaporation mode the pressure of the vapor in the channel can be considerably increased over the pressure inside the bubble due to Carnot's shock loss at the pore. With a subsurface tunnel connecting several pores, the importance of this dynamic effect further increases as the number of inactive pores at low heat fluxes is much higher than the number of active pores. Additional pores can only be activated permanently if the pressure inside the tunnel exceeds the highest pressure observed inside the bubble. With the vapor produced in a longer piece of tunnel flowing to an active pore, bubble growth velocity can become very high and, as was demonstrated by dimensional analysis of the model in Chapter 6, inertia of the liquid surrounding the bubble can further increase the pressure of the vapor in the tunnel.

7.2 Considerations regarding the design of subsurface tunnels

From the remarks above, in order to obtain a high heat transfer coefficient, the design of the subsurface tunnel should promote

- a large area covered by thin liquid films inside the tunnel,

- an efficient vapor expansion inside the tunnel,
- sufficient liquid flow to all parts of the liquid film.

Assuming liquid films being located in the corners of the tunnel as well as in vertical connections in the tunnel, a deep and thin tunnel leads to a large surface area covered by thin films. With a thin tunnel, the total length of the tunnel per unit area can be increased and thus the area of liquid films. A deep tunnel increases the total surface area and the size of the liquid films in the vertical connections. Any kind of surface roughness in the tunnel can potentially increase the liquid film area and thus the heat transfer coefficient as well.

In order to find measures suitable to obtain an efficient vapor expansion, the results from the parameter study in Section 6.2 can be employed. Due to the model setup, the behavior of the system can be expected to rather reproduce the boiling process in the suction evaporation mode at a low heat flux. In this case, vapor is only locally present in the tunnel and only one pore is active within each vapor region. The evaporation rate is low enough for dynamic effects playing a minor role. In order to expand the vapor region inside the tunnel, the curvature of the vapor front in the tunnel should be low and pressure of the vapor high. The curvature of the vapor front is small if the tunnel is deep and wide. A large contact angle would be beneficial as well, but is usually related to the wall superheat. The pressure of the vapor is high if the bubble departs at small diameters. Opposed to the parametric study in Section 6.2, the effect of flow resistance through the pore should be small in the expansion stage as liquid is fed to the films from the flooded parts of the tunnel. Consequently, for the case of the bubble curvature being higher than the curvature of the liquid-vapor front in the tunnel, vapor should spread inside the tunnel. The setup is illustrated in Figure 7.2.

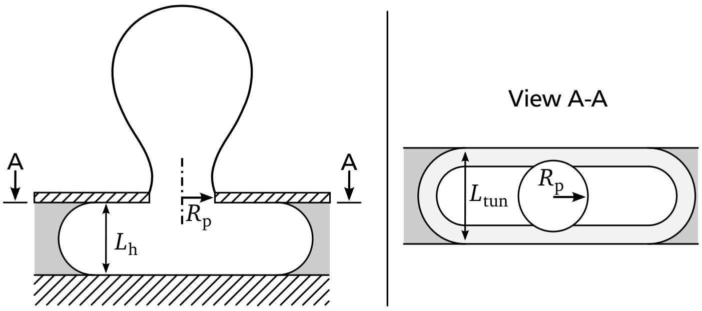

Figure 7.2: Important dimensions for vapor spreading

From the pressure data calculated in Section 6.1.2 it can be taken that the curvature of the bubble at 50 % of the departure volume is approximately given by $\kappa_b = 1.8\, a^{-0.61} R_p^{-0.39}$. For the curvature of the liquid-vapor interface κ_v in the rectangular tunnel, a solution can be obtained with the help of SURFACE EVOLVER for different contact angles. For a perfectly wetting fluid and $L_{tun} < L_h$, Ajaev and Homsy [3] gave the relation $\kappa_v = C_\kappa\, 2/L_{tun}$ with the values for C_κ given in Table 7.1, which they took from the solution of the Young-Laplace equation by Wong et al. [136].

Table 7.1: Values for C_κ from Ajaev and Homsy [3]

L_h/L_{tun}	1	1.2	1.5	2.0
C_κ	1.8862	1.7300	1.5759	1.4247

With $\kappa_\mathrm{b} > \kappa_\mathrm{v}$ the vapor should expand most of the time also with dynamic effects at the bubble neglected. By curve fitting the values in Table 7.1 with the function $C_\kappa = 0.87\,L_\mathrm{tun}/L_\mathrm{h} + 1$ this leads to the geometric guideline (7.1).

$$R_\mathrm{p} < \left(\frac{1.8\,a^{-0.61}}{\frac{1.74}{L_\mathrm{h}} + \frac{2}{L_\mathrm{tun}}} \right)^{1/0.39} \tag{7.1}$$

It should be considered that constrictions in the tunnel (like the ledge employed in the CFD simulation) can act as obstacles to the spreading of the vapor and decrease the effective tunnel width. Calculating the required pore radius for a circular pore with typical tunnel dimensions found in literature, it becomes clear that a rather small pore would be required. From this it can be concluded that typical tubes employed

- require dynamic effects to expand the vapor,
- are probably operated in the vapor expansion stage.

Liquid flow to the tunnel is dominated by flow through inactive pores as can be taken from the numerical simulations presented in Chapter 5. Different flow paths are possible depending on whether the system is operated in the vapor expansion stage or the partial dryout stage. The flow paths are illustrated in Figure 7.3.

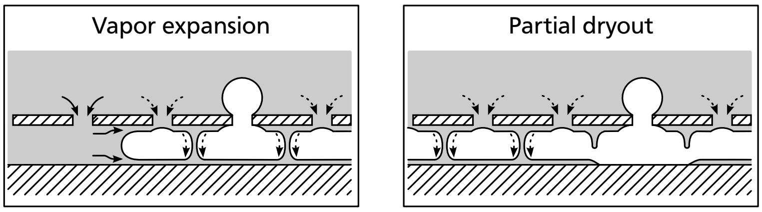

Figure 7.3: Flow to the liquid films in the suction evaporation mode

With parts of the tunnel being flooded during the vapor expansion stage, liquid can effectively enter the tunnel at the flooded pores and from there flow to the upper and lower corners. If the vapor expands completely along the tunnel, liquid needs to flow from the pool through a thin film into the tunnel and spread from there on inside the tunnel. Liquid flow from the upper to the lower corner is only possible if vertical structures exist.

To assess the effect of parameter changes on the boiling process in a subsurface channel with several pores being activated, the model presented in Chapter 6 can be modified. In this case, the pressure inside the tunnel should be approximately equal to the pressure required to activate a pore. If the heat flow increases, more pores are activated but the pressure approximately stays the same. The flow resistance between the pool and the tunnel is given by the flow resistance of a single inactive pore divided by the number of inactive pores. The flow resistance of the single pore is set to $\zeta_0^* = 100\,\zeta_\mathrm{ref}^*$ as the liquid films are very small already at low heat flows with this setup. All other settings are those of the reference case in Section 6.2. With the pressure inside the tunnel being constant, the size of the liquid films can be calculated directly for each heat flow. Figure 7.4 shows the liquid volume fraction of the upper and lower film for 20 pores being calculated. If a much longer piece of the tunnel is considered, the resistance for the flow of liquid along the tunnel from inactive to active pores starts to play a more dominant role. The dimensionless heat flow $\dot{Q}^*$ is provided to each section of the tunnel having the same dimensions as in the reference case. Therefore, the total heat flow depends on the number of pores.

Interestingly, in this stage the bubble departure diameter has almost no effect on the point of dryout. The flow resistance of the individual pores affects the liquid volume in the film. With a smaller contact

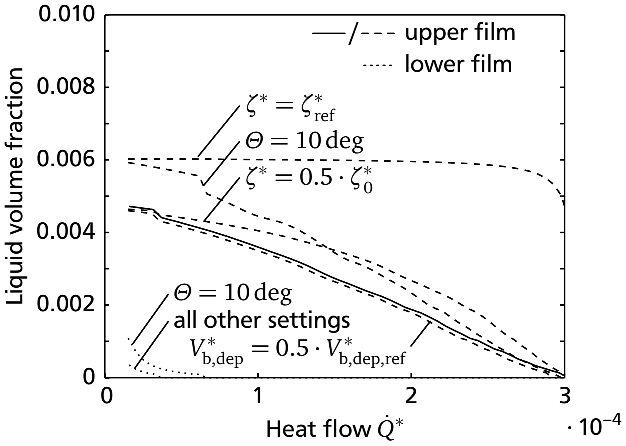

Figure 7.4: Liquid volume fraction with 20 pores calculated

angle, more liquid is located in the upper and the lower liquid film at low heat fluxes, but the point of dryout is hardly affected. The graph shows that the lower film dries out early, suggesting that for this geometry liquid in the lower corner is only present during the vapor expansion stage. This also explains why it might be beneficial to operate in the vapor expansion stage as in this case liquid is fed to the lower corners as well.

With the liquid films being this small but still connected to the pool, dryout is induced by the increasing number of active pores. Consequently, the point of dryout can be delayed by delaying the activation of additional pores. To do so in the model, the size of the active pore A^*_{p} needs to be increased. Figure 7.5 shows qualitatively the point of dryout and the point of flooding as a function of the pore size and heat flow. Dryout is assumed to occur if the film volume falls below 0.1 % of the tunnel volume. The point of flooding is calculated with the setup of Section 6.2 and the bubble departure diameter being predicted by the calculation of bubble growth with the according pore size. As the model is not accounting for vapor expansion inside the tunnel and flow of liquid in the films along the tunnel, it can only give the principle behavior.

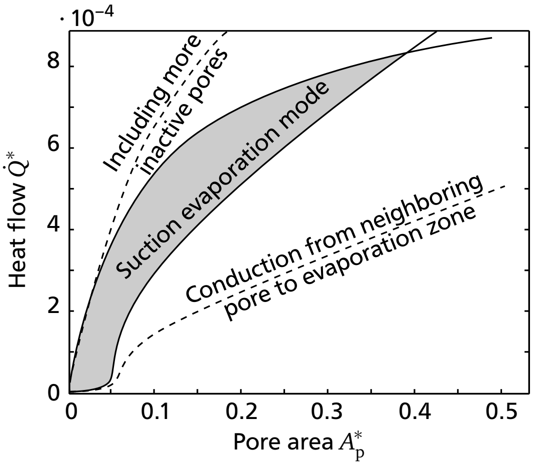

Figure 7.5: Flooding and dryout as a function of heat flow and pore size

For calculating flooding it is assumed that only the heat flow at the active pore is contributing to evaporation and the heat flow to the other pores is transmitted by free convection. If heat from the neighboring pores is conducted through the wall to the evaporation zone, the lower line limiting the range of the suction evaporation mode drops. This shows that the conductivity of the wall influences the operation range. If liquid flow is possible from pores being further away than ten pores in each direction of the active pore, the upper curve becomes steeper and the range for operating in the suction evaporation mode expands as well. In order to quantify this effect, liquid flow in direction of the tunnel needs to be modeled, which is not performed in this work.

In the following the effect of individual geometric properties on heat transfer area, vapor expansion, and flow to the films is summarized.

Pores: At active pores, small bubbles are desired for vapor expansion but a large pore area to prevent dryout. At inactive pores, flow to the liquid films should be possible also for very small films to prevent early dryout. Therefore, the pores should expand to the corner of the tunnel. As a consequence, rectangular pores are beneficial as they allow a larger pore area with small bubble departure diameter and extend over the tunnel width to connect the film with the pool.

Vertical structures: A vertical ledge increases the thin film area and liquid flow to the lower corner. On the downside, it can promote flooding and hinder vapor expansion.

Tunnel height: A deep tunnel also increases thin film area and promotes vapor expansion but flow to the lower corners through vertical structures is impeded.

Tunnel width: A wide tunnel decreases thin film area but promotes vapor expansion. A thin tunnel impedes vapor expansion.

Pore distance: The pore distance was not investigated explicitly in this work, but from the understanding of the boiling modes it should mainly affect the flow resistance between liquid pool and tunnel.

7.3 Modeling of the boiling process and prediction of heat transfer

In literature, several models were presented to predict the heat transfer during the suction evaporation mode. As parameter variations with an interface resolving CFD simulation of a tube section containing several hundred pores will not be feasibly in near future, simplified models are required to reduce empiricism. With the experiences from modeling and CFD simulations in this work, requirements can be formulated for a model truly being able to predict the heat transfer. The listed requirements can be taken to be necessary but might not be sufficient.

To predict the boiling process, fluid flow and heat transfer need to be modeled. Figure 7.6 gives the required contents of a model based on calculating heat and fluid flow. Modeling of heat transfer can be separated in modeling of internal heat transfer and external heat transfer as suggested by Nakayama et al. [94]. Models for external heat transfer typically require bubble departure diameter and frequency, which can be obtained from the flow model. The model should account for forced convection induced by bubbles and bundle effects if several tubes are employed. Internal heat transfer can be approximated if the geometry of the liquid films is known. Inside the film, an approximation of 2D conduction can give reasonable accurate results. For evaporation in the vicinity of the three phase contact line, models are readily available. From the heat transfer model, the contact angle as well as the evaporation rate are required for the flow model.

In the flow model, the pore shape of the individual pores needs to be considered and active and inactive pores have to be identified. With bubbles growing at active pores, inertia of the surrounding liquid and the acceleration of vapor through the pore need to be considered. The flow resistance at inactive pores needs to be calculated based on pore geometry and liquid film volume in the tunnel below the pore.

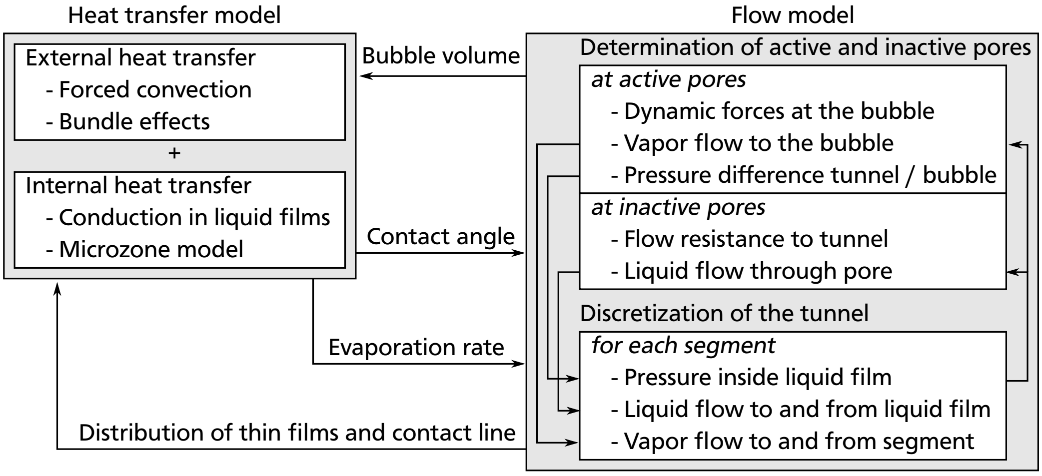

Figure 7.6: Contents of a model for predicting heat transfer

The tunnel can be discretized into several elements in two dimensions as presented in Chapter 6. As proposed by Jiang et al. [52], conservation equations can be formulated for liquid and vapor. From the liquid volume and the tunnel geometry, the film shape and pressure can be calculated assuming equilibrium conditions with a program like SURFACE EVOLVER. The front of the vapor bubble expanding inside the tunnel during the expansion stage requires special treatment. Both, vapor expansion and partial dryout need to be accounted for in the model. Concerning the models presented in literature, all of them neglect some of the effects mentioned above.

A model as suggested in Figure 7.6 requires iterations and a discretization in time and space, but simpler models neglect many significant processes. Submodels like the microzone model or the relation between film volume and pressure jump need to be solved beforehand and parameterized to reduce the computational effort. Some parts of the suggested model were already presented in this work or in literature. Calculation of external heat transfer and dynamic forces at the bubble are challenging and so far only approaches based on empirical correlations were presented.

8 Summary and Outlook

In this work, numerical simulations and modeling were performed to study liquid flow into and inside single cavities and subsurface tunnels during pool boiling. For CFD simulations, a well tested solver implemented in OPENFOAM was employed. In there, the full incompressible Navier-Stokes equations are solved with a finite volume discretization. The liquid-vapor interface is captured with the help of the VOF method and reconstructed to allow an accurate calculation of the evaporation rate and determination of the position of the three phase contact line. Evaporation in the vicinity of the three phase contact line is accounted for through a subgrid scale model. To reduce spurious currents, the curvature is smoothed. The wall boundary treatment was adjusted from the original formulation to allow the accurate simulation of capillary flows. An anti-diffusion method is implemented enabling modeling of complex geometries with contact lines being pinned at corners of the geometry. With an implicit formulation of the evaporation model, simulations of boiling flows are possible on rather coarse grids. The CFD model is fully parallelized with dynamic mesh refinement available.

In the following, the results from CFD simulation and modeling are summarized and suggestions for the extension of this work given.

8.1 Numerical simulations with single cavities and subsurface tunnels

Three principal geometries of single reentrant cavities were created. These are a circular cavity with circular pore, a square cavity with square or rectangular pore, and a circular cavity with an additional channel next to the pore connecting the liquid pool with the cavity. After setting an initial bubble nucleus into the cavity, simulations were performed until a quasi-steady state was obtained or flooding occurred. For the first two principal geometries a fixed wall superheat was set at the fluid-solid interface and for the cavity with additional channel conjugate heat transfer was calculated with a fixed heat flux at the lower boundary of the solid domain. The dimensions of the cavities, size and shape of the pores, and the heat flow were varied in the study. Fluid properties were set to those of R134a at $T_{\text{sat}} = 20\,^{\circ}\text{C}$. The sensitivity of the simulation results on selected input parameters was tested to be able to interpret the results.

The results show that with single circular reentrant cavities, either dryout or flooding of the cavity occurs depending on the size of the pore and the initial conditions. Furthermore, the thermal boundary layer on the outer surface is only slightly disturbed with a single bubble growing and departing at the pore. With a square cavity, liquid films were observed in the corners strongly enhancing heat transfer. A liquid film is located within the square or rectangular pore, connecting the liquid in the cavity with the liquid pool during bubble growth. Even though liquid can flow to the cavity this way during bubble growth and departure, dryout or flooding was observed for most settings. If a parameter range exists in which liquid flow to the cavity is in equilibrium with evaporation, it probably is small. Connecting the cavity through an additional thin channel with the pool resulted in a liquid film in the cavity and a process less prone to dryout or flooding. The liquid film is growing and shrinking with bubble growth and departure. If the liquid film reaches the bottom of the cavity during one bubble cycle, flooding occurs. For the case of the liquid film extending through the pore upwards, bubble departure is induced. A larger bubble departure diameter leads to a lower pressure inside the cavity and a longer growth period, increasing the volume of the liquid film. Increasing the width of the channel reduces the flow resistance between liquid pool and cavity, also leading to larger film volumes. The heat transfer coefficient decreases with increasing heat flux due to the characteristics of evaporation in the vicinity of the three phase contact line.

To study the processes occurring at the pores of subsurface tunnels, a piece of subsurface tunnel was simulated with two pores. Inside the tunnel, a vertical ledge was introduced to enable the spreading of the liquid film from the upper to the lower corner of the tunnel. A fixed wall superheat was applied and simulations performed until the liquid film volume was quasi-steady. With this setup, the depth of the tunnel, shape and size of the pores, size of the ledge, and wall superheat were varied.

In the simulations with two pores, the bubble was growing at one pore while liquid was flowing into the tunnel at the other pore. Again, liquid flow to the tunnel is related with bubble growth. The pressure of the vapor in the tunnel was found to be increased over the pressure inside the bubble due to large velocities of vapor flowing through the pore and Carnot's shock loss at the point of expansion into the bubble after the pore. It was shown that pore size and shape have a strong influence on the flow into the tunnel through their effect on bubble departure diameter and flow resistance between liquid pool and liquid film. With small or unfavorable shaped pores, partial or complete dryout of the tunnel were observed, while with a large circular pore or a shallow tunnel, flooding occurred. The heat transfer coefficient was found to be related to the area covered by liquid films and the thickness of the liquid films. The analysis of the heat transfer shows that the increase in heat transfer coefficient with such surfaces is based not solely on an increase in surface area.

8.2 Analysis of the influence of parameters and application to realistic structures

It was found that liquid flow into the tunnel can accurately be calculated if the pressure jump across the liquid-vapor interfaces, between bubble and vapor in the tunnel, and the flow resistance between liquid pool and liquid film is known. Employing this, a simple model was created to study a wider range of parameters. The pressure jump across the liquid-vapor interface of the bubble is calculated by solving the Young-Laplace equation in MATLAB for a bubble growing at a circular pore. The pressure jump at the liquid-vapor interface of the liquid film is solved for with the help of the software SURFACE EVOLVER, which is based on the minimization of surface energies. The model is validated by a comparison with the results of the CFD simulation and the limits of the model are discussed.

The model gives characteristic dimensionless numbers, which can be employed to analyze the boiling process. Based on the setup of the CFD simulation, a parametric study was performed giving the influence of parameters on the point of flooding and the point of dryout. Flooding occurs at larger heat flows if the bubble departure diameter is large, the tunnel is shallow or thin. Early dryout is obtained with a large flow resistance between pool and tunnel, a small active pore area or a large contact angle.

If the influence of the dimensionless parameters on the boiling process with a realistic surface is investigated, additional effects have to be considered. Next to the experimentally observed partial flooding of the subsurface tunnel during the suction evaporation mode, the numerical simulations show that also partial dryout of the tunnel is possible. Based on this, two additional sub-stages of the suction evaporation mode are suggested, which are the vapor expansion stage and the partial dryout stage. Therefore, in order to obtain a large heat transfer coefficient, the area covered by thin liquid films should be large, the vapor efficiently expand inside the tunnel, and liquid flow to all parts of the liquid film should be sufficient. To obtain a large area of thin liquid films, deep and thin tunnels are beneficial. Vapor expansion is influenced by bubble departure diameter and tunnel geometry. A requirement is formulated for the dimensions of tunnel and pore if vapor expansion without dynamic effects is desired. The point of dryout is significantly influenced by how fast additional pores are activated. Therefore, to delay dryout, large active pores are required. The opposing requirements for vapor expansion and preventing dryout can be fulfilled if the pore shape is adapted from circular to rectangular. In order to allow sufficient liquid flow to the lower corners, an operation of the surface in the vapor expansion stage might be beneficial.

In order to be able to model the boiling process in the future, a high level of detail is required. Otherwise, important processes influencing heat transfer and the point of flooding or dryout are neglected. The shape and dimensions of the pores and the tunnel have to be considered. Dynamic effects resulting from the inertia of liquid surrounding the bubble and the flow of the vapor through the pore have to be implemented. Furthermore, the model requires a discretization of the tunnel in two dimensions. To save computational time, submodels like the model for evaporation in the vicinity of the three phase contact line and the calculation of the pressure jump have to be solved in advance for a set of parameters and the results provided to the full model.

8.3 Outlook

In future studies, extending the CFD simulations to the vapor expansion stage would be of interest, as it is the dominating boiling mode at low heat flows. To do this, the existing CFD method and geometries can be employed and the initial and boundary conditions be adapted to find the interrelation between process parameters and the vapor expansion. If one additional pore is added to the computational domain, the processes occurring at high heat flows can be studied up to the activation of a second pore.

To investigate a large parameter range and improve the understanding of the interrelations, a full model based on the suggestions in Chapter 7 can be created. Even if several parts of the model require semi-empiric correlations, the development of structured surfaces with subsurface tunnels could be facilitated.

As was described in Chapter 2, boiling of mixtures is of interest in many technical applications but not well understood. Especially with structured surfaces, additional effects can appear influencing the boiling process, which are still under discussion. In order to study the effect of mixtures, the flow solver can be extended to account for a non-evaporating component. With this, accumulation of the less volatile component inside the structure and conditions leading to its effective removal can be investigated.

Bibliography

[1] H. S. Abarajith and V. K. Dhir. A Numerical Study of the Effect of Contact Angle on the Dynamics of a Single Bubble During Pool Boiling. In *Proceedings of ASME International Mechanical Engineering Congress and Exposition*, New Orleans, Louisiana, USA, 2002.

[2] H. S. Abarajith, V. K. Dhir, G. Warrier, and G. Son. Numerical Simulation and Experimental Validation of the Dynamics of Multiple Bubble Merger During Pool Boiling Under Microgravity Conditions. *Annals of the New York Academy of Sciences*, 1027(1):235–258, 2004.

[3] V. S. Ajaev and G. M. Homsy. Modeling Shapes and Dynamics of Confined Bubbles. *Annual Review of Fluid Mechanics*, 38(1):277–307, 2006.

[4] E. Aktinol and V. K. Dhir. Numerical Simulation of Nucleate Boiling Phenomenon Coupled with Thermal Response of the Solid. *Microgravity Science and Technology*, 24(4):255–265, 2012.

[5] A. Albadawi, D. B. Donoghue, A. J. Robinson, D. B. Murray, and Y. M. C. Delauré. Influence of Surface Tension Implementation in Volume of Fluid and Coupled Volume of Fluid with Level Set Methods for Bubble Growth and Detachment. *International Journal of Multiphase Flow*, 53:11–28, 2013.

[6] A. Alke, D. Bothe, M. Kröger, B. Weigand, D. Weirich, and H. Weking. Direct Numerical Simulation of High Schmidt Number Mass Transfer from air Bubbles Rising in Liquids Using the Volume-of-Fluid-Method. *Ercoftac Bulletin*, 82:5–10, 2010.

[7] Z. H. Ayub and A. E. Bergles. Pool Boiling from GEWA Surfaces in Water and R-113. *Wärme- und Stoffübertragung*, 21:209–219, 1987.

[8] Z. H. Ayub and A. E. Bergles. Nucleate Pool Boiling Curve Hysteresis for GEWA-T Surfaces in Saturated R-113. *Experimental Thermal and Fluid Science*, 3(2):249–255, 1990.

[9] H. D. Baehr and K. Stephan. *Wärme- und Stoffübertragung*. Springer, Berlin, Heidelberg, 2013.

[10] Q. Bai and Y. Fujita. Numerical Simulation of Bubble Growth in Nucleate Boiling - Effects of System Parameter. *Multiphase Science and Technology*, 12(3&4), 2000.

[11] S. Batzdorf. *Heat Transfer and Evaporation During Single Drop Impingement onto a Superheated Wall*. PhD thesis, submitted, TU Darmstadt, 2015.

[12] S. Batzdorf, J. Dietl, and P. Stephan. Accurate Calculation of Interfacial Temperature Gradients for Simulation of Evaporation and Condensation in a VOF Framework. In *Proceedings of the 2nd International Conference on Numerical Methods in Multiphase Flows*, Darmstadt, Germany, 2014.

[13] S. H. Bhavnani, G. Fournelle, and R. C. Jaeger. Immersion-cooled Heat Sinks for Electronics: Insight from High-speed Photography. *IEEE Transactions on Components and Packaging Technologies*, 24(2):166–176, 2001.

[14] C. H. Bosanquet. On the Flow of Liquids into Capillary Tubes. *Philosophical Magazine Series 6*, 45(267):525–531, 1923.

[15] J. U. Brackbill, D. B. Kothe, and C. Zemach. A Continuum Method for Modeling Surface Tension. *Journal of Computational Physics*, 100(2):335–354, 1992.

[16] K. A. Brakke. The Surface Evolver. *Experimental Mathematics*, 1(2):141–165, 1992.

[17] M. W. Browne and P. K. Bansal. Heat Transfer Characteristics of Boiling Phenomenon in Flooded Refrigerant Evaporators. *Applied Thermal Engineering*, 19(6):595–624, 1999.

[18] Y. A. Buyevich and B. W. Webbon. Dynamics of Vapour Bubbles in Nucleate Boiling. *International Journal of Heat and Mass Transfer*, 39(12):2409–2426, 1996.

[19] V. P. Carey. *Liquid-vapor Phase-change Phenomena: An Introduction to the Thermophysics of Vaporization and Condensation Processes in Heat Transfer Equipment*. Taylor & Francis Group, 2008.

[20] Y. Chen and M. Groll. Dynamics and Shape of Bubbles on Heating Surfaces: A Simulation Study. *International Journal of Heat and Mass Transfer*, 49(5–6):1115–1128, 2006.

[21] Y. Chen, M. Groll, and R. Mertz. A Dynamic Model for Pool Boiling Heat Transfer on Enhanced Surfaces with Sub-surface Channels. In *Proceedings of 3rd International Symposium on Two-Phase Flow Modeling and Experimentation*, Pisa, Italy, 2004.

[22] Y. Chen, M. Groll, R. Mertz, and R Kulenovic. Bubble Dynamics of Boiling of Propane and Iso-Butane on Smooth and Enhanced Tubes. *Experimental Thermal and Fluid Science*, 28(2–3):171–178, 2004.

[23] Y. Chen, M. Groll, R. Mertz, and R. Kulenovic. Pool Boiling Heat Transfer of Propane, Isobutane and their Mixtures on Enhanced Tubes with Reentrant Channels. *International Journal of Heat and Mass Transfer*, 48(11):2310–2322, 2005.

[24] Y. Chen, M. Groll, R. Mertz, and R. Kulenovic. Visualization and Mechanisms of Pool Boiling of Propane, Isobutane and their Mixtures on Enhanced Tubes with Reentrant Channels. *International Journal of Heat and Mass Transfer*, 48(12):2516–2528, 2005.

[25] L. H. Chien and R. L. Webb. Measurement of Bubble Dynamics on an Enhanced Boiling Surface. *Experimental Thermal and Fluid Science*, 16(3):177–186, 1998.

[26] L. H. Chien and R. L. Webb. A Nucleate Boiling Model for Structured Enhanced Surfaces. *International Journal of Heat and Mass Transfer*, 41(14):2183–2195, 1998.

[27] L. H. Chien and R. L. Webb. A Parametric Study of Nucleate Boiling on Structured Surfaces, Part I: Effect of Tunnel Dimensions. *Journal of Heat Transfer*, 120(4):1042–1048, 1998.

[28] L. H. Chien and R. L. Webb. A Parametric Study of Nucleate Boiling on Structured Surfaces, Part II: Effect of Pore Diameter and Pore Pitch. *Journal of Heat Transfer*, 120(4):1049–1054, 1998.

[29] L. H. Chien and R. L. Webb. Visualization of Pool Boiling on Enhanced Surfaces. *Experimental Thermal and Fluid Science*, 16(4):332–341, 1998.

[30] M. G. Cooper and A. J. P. Lloyd. The Microlayer in Nucleate Pool Boiling. *International Journal of Heat and Mass Transfer*, 12(8):895–913, 1969.

[31] A. K. Das, P. K. Das, and P. Saha. Nucleate Boiling of Water from Plain and Structured Surfaces. *Experimental Thermal and Fluid Science*, 31(8):967–977, 2007.

[32] V. K. Dhir, G. R. Warrier, and E. Aktinol. Numerical Simulation of Pool Boiling: A Review. *Journal of Heat Transfer*, 135(6), 2013.

[33] S. Di Bari and A. J. Robinson. Experimental Study of Gas Injected Bubble Growth from Submerged Orifices. *Experimental Thermal and Fluid Science*, 44:124–137, 2013.

[34] J. Dietl and P. Stephan. Numerical Simulation and Modeling of Liquid Film Evaporation Inside Axisymmetric Reentrant Cavities. *MATEC Web of Conferences*, 18, 2014.

[35] J. Dietl and P. Stephan. Numerical Simulation of Boiling from a Single Reentrant-Cavity. In *Proceedings of the 15th International Heat Transfer Conference*, Kyoto, Japan, 2014.

[36] D. Enright, R. Fedkiw, J. Ferziger, and I. Mitchell. A Hybrid Particle Level Set Method for Improved Interface Capturing. *Journal of Computational Physics*, 183(1):83–116, 2002.

[37] D. Fuster, G. Agbaglah, C. Josserand, S. Popinet, and S. Zaleski. Numerical Simulation of Droplets, Bubbles and Waves: State of the Art. *Fluid Dynamics Research*, 41(6), 2009.

[38] VDI Gesellschaft. Stoffwerte von R134a (1,1,1,2-Tetrafluorethan). In *VDI-Wärmeatlas*, pages 232–248. Springer Berlin Heidelberg, 2006.

[39] VDI Gesellschaft. Stoffwerte von reinen Metallen und Metallegierungen. In *VDI-Wärmeatlas*, pages 382–396. Springer Berlin Heidelberg, 2006.

[40] F. Gibou, R. Fedkiw, L. T. Cheng, and M. Kang. A Second-Order-Accurate Symmetric Discretization of the Poisson Equation on Irregular Domains. *Journal of Computational Physics*, 176(1):205–227, 2002.

[41] D. Gorenflo, P. Sokol, and S. Caplanis. Zum Wärmeübergang beim Blasensieden von Kohlenwasserstoffen und Halogen-Kältemitteln an einem Glattrohr und einem Hochleistungs-Rippenrohr. *Wärme- und Stoffübertragung*, 26:273–281, 1991.

[42] A. Goyal, R. C. Jaeger, S. H. Bhavnani, C. D. Ellis, N. K. Phadke, M. Azimi-Rashti, and J. S. Goodling. Re-entrant Cavity Heat Sinks Formed by Anisotropic Etching and Silicon Direct Wafer Bonding. In *Proceedings of Eighth Annual IEEE Semiconductor Thermal Measurement and Management Symposium. SEMI-THERM VIII*, San Jose, CA, USA, 1992.

[43] I. Haider and R. L. Webb. A Transient Micro-Convection Model of Nucleate Pool Boiling. *International Journal of Heat and Mass Transfer*, 40(15):3675–3688, 1997.

[44] S. Hardt and F. Wondra. Evaporation Model for Interfacial Flows Based on a Continuum-field Representation of the Source Terms. *Journal of Computational Physics*, 227(11):5871–5895, 2008.

[45] S. Herbert, S. Fischer, T. Gambaryan-Roisman, and P. Stephan. Local Heat Transfer and Phase Change Phenomena During Single Drop Impingement on a Hot Surface. *International Journal of Heat and Mass Transfer*, 61:605–614, 2013.

[46] C. W. Hirt, A. A. Amsden, and J. L. Cook. An Arbitrary Lagrangian-Eulerian Computing Method for all Flow Speeds. *Journal of Computational Physics*, 14(3):227–253, 1974.

[47] C. W. Hirt and B. D. Nichols. Volume of Fluid (VOF) Method for the Dynamics of Free Boundaries. *Journal of Computational Physics*, 39(1):201–225, 1981.

[48] C. Hutter, D. B. R. Kenning, K. Sefiane, T. G. Karayiannis, H. Lin, G. Cummins, and A. J. Walton. Experimental Pool Boiling Investigations of FC-72 on Silicon with Artificial Cavities and Integrated Temperature Microsensors. *Experimental Thermal and Fluid Science*, 34(4):422–433, 2010.

[49] J. Israelachvili. *Intermolecular and Surface Forces*. Academic Press, Elsevier, 2011.

[50] R. I. Issa. Solution of the Implicitly Discretised Fluid Flow Equations by Operator-Splitting. *Journal of Computational Physics*, 62(1):40–65, 1986.

[51] D. Jamet, O. Lebaigue, N. Coutris, and J. M. Delhaye. The Second Gradient Method for the Direct Numerical Simulation of Liquid–Vapor Flows with Phase Change. *Journal of Computational Physics*, 169(2):624–651, 2001.

[52] Y. Y. Jiang, W. C. Wang, D. Wang, and B. X. Wang. Boiling Heat Transfer on Machined Porous Surfaces with Structural Optimization. *International Journal of Heat and Mass Transfer*, 44(2):443–456, 2000.

[53] D. Jung, K. An, and J. Park. Nucleate Boiling Heat Transfer Coefficients of HCFC22, HFC134a, HFC125, and HFC32 on Various Enhanced Tubes. *International Journal of Refrigeration*, 27:202–206, 2004.

[54] D. Jung, H. Lee, D. Bae, and J. Ha. Nucleate Boiling Heat Transfer Coefficients of Flammable Refrigerants on Various Enhanced Tubes. *International Journal of Refrigeration*, 28(3):451–455, 2005.

[55] D. Juric and G. Tryggvason. Computations of Boiling Flows. *International Journal of Multiphase Flow*, 24(3):387–410, 1998.

[56] M. A. Kedzierski. Calorimetric and Visual Measurements of R123 Pool boiling on Four Enhanced Surfaces. Technical Report, 5732, US Departement of Commerce, Washington DC, 1995.

[57] M. A. Kedzierski. The Effect of Lubricant Concentration, Miscibility, and Viscosity on R134a Pool Boiling. *International Journal of Refrigeration*, 24(4):348–366, 2001.

[58] J. Kim. Review of Nucleate Pool Boiling Bubble Heat Transfer Mechanisms. *International Journal of Multiphase Flow*, 35(12):1067–1076, 2009.

[59] N. H. Kim and K. K. Choi. Nucleate Pool Boiling on Structured Enhanced Tubes Having Pores with Connecting Gaps. *International Journal of Heat and Mass Transfer*, 44(1):17–28, 2001.

[60] N. H. Kim and D. Y. Kim. Pool Boiling of R-123/Oil Mixtures on Enhanced Tubes Having Different Pore Sizes. *International Journal of Heat and Mass Transfer*, 53(9–10):2311–2317, 2010.

[61] N. H. Kim, E. J. Lee, and H. W. Byun. Pool Boiling of R-134a/Oil Mixtures on Enhanced Tubes Having Different Pore and Gap Sizes. *International Journal of Heat and Mass Transfer*, 66:118–127, 2013.

[62] N. H. Kim and C. K. Min. Pool Boiling of Refrigerant-Oil Mixtures on Enhanced Tubes Having Different Pore Sizes. In *Proceedings of International Refrigeration and Air Conditioning Conference*, West Lafayette, USA, 2004.

[63] J. F. Klausner, R. Mei, D. M. Bernhard, and L. Z. Zeng. Vapor Bubble Departure in Forced Convection Boiling. *International Journal of Heat and Mass Transfer*, 36(3):651–662, 1993.

[64] N. I. Kolev. The Influence of Mutual Bubble Interaction on the Bubble Departure Diameter. *Experimental Thermal and Fluid Science*, 8(2):167–174, 1994.

[65] O. Kruck and A. Luke. Pool Boiling of R134a and Propane on Horizontal Mild Steel Tubes with Enhanced Surfaces. In *Proceedings of ECI International Conference on Boiling Heat Transfer*, Florianópolis, Brazil, 2009.

[66] H. Kubo, H. Takamatsu, and H. Honda. Effects of Size and Number Density of Micro-reentrant Cavities on Boiling Heat Transfer from a Silicon Chip Immersed in Degassed and Gas-dissolved FC-72. *Journal of Enhanced Heat Transfer*, 6(2-4):151–160, 1999.

[67] C. Kunkelmann. *Numerical Modeling and Investigation of Boiling Phenomena*. PhD thesis, TU Darmstadt, 2011.

[68] C. Kunkelmann, K. Ibrahem, N. Schweizer, S. Herbert, P. Stephan, and T. Gambaryan-Roisman. The Effect of Three-Phase Contact Line Speed on Local Evaporative Heat Transfer: Experimental and Numerical Investigations. *International Journal of Heat and Mass Transfer*, 55(7–8):1896–1904, 2012.

[69] C. Kunkelmann and P. Stephan. Modification and Extension of a Standard Volume-of-Fluid Solver for Simulating Boiling Heat Transfer. In *Proceedings of ECCOMAS CFD*, Lisbon, Portugal, 2010.

[70] C. Kunkelmann and P. Stephan. Numerical Simulation of the Transient Heat Transfer during Nucleate Boiling of Refrigerant HFE-7100. *International Journal of Refrigeration*, 33(7):1221–1228, 2010.

[71] W. Kühnel. *Differentialgeometrie*. Springer-Verlag, 2005.

[72] B. Lafaurie, C. Nardone, R. Scardovelli, S. Zaleski, and G. Zanetti. Modelling Merging and Fragmentation in Multiphase Flows with SURFER. *Journal of Computational Physics*, 113(1):134–147, 1994.

[73] R. C. Lee and J. E. Nydahl. Numerical Calculation of Bubble Growth in Nucleate Boiling From Inception Through Departure. *Journal of Heat Transfer*, 111(2):474–479, 1989.

[74] W. Lee and G. Son. Numerical Simulation of Boiling Enhancement on a Microstructured Surface. *International Communications in Heat and Mass Transfer*, 38(2):168–173, 2011.

[75] W. Lee, G. Son, and H. Y. Yoon. Numerical Study of Bubble Growth and Boiling Heat Transfer on a Microfinned Surface. *International Communications in Heat and Mass Transfer*, 39(1):52–57, 2012.

[76] Y. Lee, D. G. Kang, J. H. Kim, and D. Jung. Nucleate Boiling Heat Transfer Coefficients of HFO1234yf on Various Enhanced Surfaces. *International Journal of Refrigeration*, 38:198–205, 2014.

[77] Z. D. Li, L. Zhang, J. F. Zhao, H. X. Li, K. Li, and K. Wu. Numerical Simulation of Bubble Dynamics and Heat Transfer with Transient Thermal Response of Solid Wall During Pool Boiling of FC-72. *International Journal of Heat and Mass Transfer*, 84:409–418, 2015.

[78] X. D. Liu, R. P. Fedkiw, and M. Kang. A Boundary Condition Capturing Method for Poisson's Equation on Irregular Domains. *Journal of Computational Physics*, 160(1):151–178, 2000.

[79] A. Luke and O. Kruck. Heat Transfer Measurements of R134a and Propane Boiling at Evaporator Tubes with Plain and Enhanced Finned Surfaces. In *Proceedings of International Refrigeration and Air Conditioning Conference*, West Lafayette, USA, 2008.

[80] A. Luke and B. C. F. Müller. Heat Transfer Mechanisms of Propane Boiling on Horizontal Steel Tubes With Smooth and Enhanced Surfaces. In *Proceedings of the 14th International Heat Transfer Conference*, Washington DC, USA, 2010.

[81] M. Mann, K. Stephan, and P. Stephan. Influence of Heat Conduction in the Wall on Nucleate Boiling Heat Transfer. *International Journal of Heat and Mass Transfer*, 43(12):2193–2203, 2000.

[82] R. Marek and J. Straub. Analysis of the Evaporation Coefficient and the Condensation Coefficient of Water. *International Journal of Heat and Mass Transfer*, 44(1):39–53, 2001.

[83] P. J. Marto and V. J. Lepere. Pool Boiling Heat Transfer From Enhanced Surfaces to Dielectric Fluids. *Journal of Heat Transfer*, 104(2):292–299, 1982.

[84] P. J. Marto and W. M. Rohsenow. Effects of Surface Conditions on Nucleate Pool Boiling of Sodium. *Journal of Heat Transfer*, 88(2):196–203, 1966.

[85] S. B. Memory, N. Akcasayar, H. Eraydin, and P. J. Marto. Nucleate Pool Boiling of R-114 and R-114-Oil Mixtures from Smooth and Enhanced Surfaces II. Tube Bundles. *International Journal of Heat and Mass Transfer*, 38(8):1363–1376, 1995.

[86] S. B. Memory, D. C. Sugiyama, and P. J. Marto. Nucleate Pool Boiling of R-114 and R-114-Oil Mixtures from Smooth and Enhanced Surfaces I. Single Tubes. *International Journal of Heat and Mass Transfer*, 38(8):1347–1361, 1995.

[87] R. Mertz. *Beitrag zum Behältersieden von Kohlenwasserstoffen an Rohren mit hinterschnittenen Oberflächen*. PhD thesis, Universität Stuttgart, 2001.

[88] B. B. Mikic and W. M. Rohsenow. A New Correlation of Pool-Boiling Data Including the Effect of Heating Surface Characteristics. *Journal of Heat Transfer*, 91(2):245–250, 1969.

[89] K. Mohrlok, K. Spindler, and E. Hahne. The Influence of a Low Viscosity Oil on the Pool Boiling Heat Transfer of the Refrigerant R507. *International Journal of Refrigeration*, 24(1):25–40, 2001.

[90] A. Mukherjee and V. K. Dhir. Study of Lateral Merger of Vapor Bubbles During Nucleate Pool Boiling. *Journal of Heat Transfer*, 126(6):1023–1039, 2004.

[91] A. Mukherjee and S. Kandlikar. Numerical Study of Single Bubbles with Dynamic Contact Angle during Nucleate Pool Boiling. *International Journal of Heat and Mass Transfer*, 50(1–2):127–138, 2007.

[92] T. G. Myers and J. P. F. Charpin. A Mathematical Model of the Leidenfrost Effect on an Axisymmetric Droplet. *Physics of Fluids (1994-present)*, 21(6), 2009.

[93] W. Nakayama, T. Daikoku, H. Kuwahara, and T. Nakajima. Dynamic Model of Enhanced Boiling Heat Transfer on Porous Surfaces—Part I: Experimental Investigation. *Journal of Heat Transfer*, 102(3):445–450, 1980.

[94] W. Nakayama, T. Daikoku, H. Kuwahara, and T. Nakajima. Dynamic Model of Enhanced Boiling Heat Transfer on Porous Surfaces—Part II: Analytical Modeling. *Journal of Heat Transfer*, 102(3):451–456, 1980.

[95] W. Nakayama, T. Daikoku, and T. Nakajima. Effects of Pore Diameters and System Pressure on Saturated Pool Nucleate Boiling Heat Transfer From Porous Surfaces. *Journal of Heat Transfer*, 104(2):286–291, 1982.

[96] N. Nimkar, S. H. Bhavnani, and R. C. Jaeger. Effect of Nucleation Site Spacing on the Pool Boiling Characteristics of a Structured Surface. *International Journal of Heat and Mass Transfer*, 49(17-18):2829–2839, 2006.

[97] S. Nukiyama. The Maximum and Minimum Values of the Heat Q Transmitted from Metal to Boiling Water under Atmospheric Pressure. *Journal of the Japan Society of Mechanical Engineers*, 7:367–374, 1934.

[98] N. K. Phadke, S. H. Bhavnani, A. Goyal, R. C. Jaeger, and J. S. Goodling. Re-Entrant Cavity Surface Enhancements for Immersion Cooling of Silicon Multichip Packages. *IEEE Transactions on Components, Hybrids, and Manufacturing Technology*, 15(5):815–822, 1992.

[99] D. M. Qiu, S. Singh, and V. K. Dhir. Dynamics of Bubble Growth on a Heated Surface under Low Gravity Conditions. *AIP Conference Proceedings*, 504(1):751–758, 2000.

[100] M. Raessi, J. Mostaghimi, and M. Bussmann. Advecting Normal Vectors: A New Method for Calculating Interface Normals and Curvatures When Modeling Two-Phase Flows. *Journal of Computational Physics*, 226(1):774–797, 2007.

[101] E. G. Ragi. Composite Structure for Boiling Liquids and Its Formation. Patent, US3684007 A, 1972.

[102] K. G. Rajulu, R. Kumar, B. Mohanty, and H. K. Varma. Enhancement of Nucleate Pool Boiling Heat Transfer Coefficient by Reentrant Cavity Surfaces. *Heat and Mass Transfer*, 2004.

[103] C. Ramaswamy, Y. Joshi, W. Nakayama, and W. B. Johnson. Semi-Analytical Model for Boiling from Enhanced Structures. *International Journal of Heat and Mass Transfer*, 46(22):4257–4269, 2003.

[104] G. Ribatski and J. R. Thome. Nucleate Boiling Heat Transfer of R134a on Enhanced Tubes. *Applied Thermal Engineering*, 26(10):1018–1031, 2006.

[105] D. M. Robinson and J. R. Thome. Local Bundle Boiling Heat Transfer Coefficients on a Turbo-BII HP Tube Bundle (RP-1089). *HVAC&R Research*, 10(4):441–457, 2004.

[106] R. W. Schrage. *A Theoretical Study of Interphase Mass Transfer*. Columbia University Press, 1953.

[107] P. R. Sharma. Determination of Heat Transfer Rates in Nucleate Pool Boiling of Pure Liquids for a Wide Range of Pressure and Heat Flux. In *Proceedings of the 11th International Heat Transfer Conference*, Kyongju, South Korea, 1998.

[108] M. Shoji and Y. Takagi. Bubbling Features from a Single Artificial Cavity. *International Journal of Heat and Mass Transfer*, 44(14):2763–2776, 2001.

[109] A. Sielaff, J. Dietl, S. Herbert, and P. Stephan. The Influence of System Pressure on Bubble Coalescence in Nucleate Boiling. *Heat Transfer Engineering*, 35(5):420–429, 2014.

[110] A. Sielaff and P. Stephan. The Influence of Single Bubble Growth and Bubble Coalescence on Boiling Heat Transfer. In *Proceedings of the 15th International Heat Transfer Conference*, Kyoto, Japan, 2014.

[111] G. Son and V. K. Dhir. Numerical Simulation of Film Boiling Near Critical Pressures With a Level Set Method. *Journal of Heat Transfer*, 120(1):183–192, 1998.

[112] G. Son, V. K. Dhir, and N. Ramanujapu. Dynamics and Heat Transfer Associated With a Single Bubble During Nucleate Boiling on a Horizontal Surface. *Journal of Heat Transfer*, 121(3):623–631, 1999.

[113] G. Son, N. Ramanujapu, and V. K. Dhir. Numerical Simulation of Bubble Merger Process on a Single Nucleation Site During Pool Nucleate Boiling. *Journal of Heat Transfer*, 124(1):51–62, 2002.

[114] K. Spindler and E. Hahne. The Influence of Oil on Nucleate Pool Boiling Heat Transfer. *Heat and Mass Transfer*, 45:979–990, 2009.

[115] P. Stephan and C. A. Busse. Analysis of the Heat Transfer Coefficient of Grooved Heat Pipe Evaporator Walls. *International Journal of Heat and Mass Transfer*, 35(2):383–391, 1992.

[116] P. Stephan, A. Sielaff, S. Fischer, J. Dietl, and S. Herbert. A Contribution to the Basic Understanding of Nucleate Boiling Phenomena: Generic Experiments and Numerical Simulations. *Thermal Science and Engineering*, 21(2):39–57, 2013.

[117] Y. Sui, H. Ding, and P. D. M. Spelt. Numerical Simulations of Flows with Moving Contact Lines. *Annual Review of Fluid Mechanics*, 46(1):97–119, 2014.

[118] M. Sussman and E. G. Puckett. A Coupled Level Set and Volume-of-Fluid Method for Computing 3d and Axisymmetric Incompressible Two-Phase Flows. *Journal of Computational Physics*, 162(2):301–337, 2000.

[119] M. Sussman, P. Smereka, and S. Osher. A Level Set Approach for Computing Solutions to Incompressible Two-Phase Flow. *Journal of Computational Physics*, 114(1), 1994.

[120] R. A. Tatara and P. Payvar. Pool Boiling of Pure R134a from a Single Turbo-BII-HP Tube. *International Journal of Heat and Mass Transfer*, 43:2233–2236, 2000.

[121] J. R. Thome. *Enhanced Boiling Heat Transfer*. Hemisphere Pub. Corp., London, 1990.

[122] J. R. Thome and D. M. Robinson. Prediction of Local Bundle Boiling Heat Transfer Coefficients: Pure Refrigerant Boiling on Plain, Low Fin, and Turbo-BII HP Tube Bundles. *Heat Transfer Engineering*, 27(10):20–29, 2006.

[123] R. R. Trewin, M. K. Jensen, and A. E. Bergles. Enhanced Boiling Heat Transfer in Horizontal Test Bundles. Technical Report DOE/ID/12772–3, Rensselaer Polytechnic Inst., New York, 1994.

[124] S. O. Unverdi and G. Tryggvason. A Front-Tracking Method for Viscous, Incompressible, Multi-Fluid Flows. *Journal of Computational Physics*, 100(1):25–37, 1992.

[125] C. H. Wang and V. K. Dhir. On the Gas Entrapment and Nucleation Site Density During Pool Boiling of Saturated Water. *Journal of Heat Transfer*, 115(3):670–679, 1993.

[126] P. C. Jr. Wayner, Y. K. Kao, and L. V. LaCroix. The Interline Heat-Transfer Coefficient of an Evaporating Wetting Film. *International Journal of Heat and Mass Transfer*, 19(5):487–492, 1976.

[127] R. L. Webb and N. H. Kim. *Principles of Enhanced Heat Transfer*. Taylor & Francis, Boca Raton, 2005.

[128] R. L. Webb and C. Pais. Nucleate Pool Boiling Data for Five Refrigerants on Plain, Integral-Fin and Enhanced Tube Geometries. *International Journal of Heat and Mass Transfer*, 35(8):1893–1904, 1992.

[129] J. E. Welch, F. H. Harlow, J. P. Shannon, and B. J. Daly. The MAC Method. A Computing Technique for Solving Viscous, Incompressible, Transient Fluid-Flow Problems Involving Free Surfaces. In *Los Alamos Scientific Laboratory Report*. Los Alamos Laboratory, 1966.

[130] S. W. J. Welch. Local Simulation of Two-Phase Flows Including Interface Tracking with Mass Transfer. *Journal of Computational Physics*, 121(1):142–154, 1995.

[131] S. W. J. Welch and J. Wilson. A Volume of Fluid Based Method for Fluid Flows with Phase Change. *Journal of Computational Physics*, 160(2):662–682, 2000.

[132] H. G. Weller, G. Tabor, H. Jasak, and C. Fureby. A Tensorial Approach to Computational Continuum Mechanics Using Object-Oriented Techniques. *Computers in Physics*, 12(6):620–631, 1998.

[133] F. Wondra, J. Dittmann, P. Stephan, and A. Beutler. Optimization of High Performance Evaporator Tubes through Structural Modifications for Pool Boiling Heat Transfer. In *Proceedings of 5th European Thermal-Sciences Conference*, Eindhoven, Netherlands, 2008.

[134] F. Wondra and P. Stephan. Experimentelle Untersuchung der Mikroskalenverdampfung in hinterschnittenen Oberflächenstrukturen. *Chemie Ingenieur Technik*, 79(8):1229–1234, 2007.

[135] F. Wondra and P. Stephan. Nucleate Pool Boiling on Tubes with Subsurface Mini and Micro Channels. In *Proceedings of the 6th International ASME Conference on Nanochannels, Microchannels and Minichannels*, Darmstadt, Germany, 2008.

[136] H. Wong, S. Morris, and C. J. Radke. Three-Dimensional Menisci in Polygonal Capillaries. *Journal of Colloid and Interface Science*, 148(2):317–336, 1992.

[137] J. Wu and V. K. Dhir. Numerical Simulations of the Dynamics and Heat Transfer Associated With a Single Bubble in Subcooled Pool Boiling. *Journal of Heat Transfer*, 132(11), 2010.

[138] J. Wu, V. K. Dhir, and J. Qian. Numerical Simulation of Subcooled Nucleate Boiling by Coupling Level-Set Method with Moving-Mesh Method. *Numerical Heat Transfer, Part B: Fundamentals*, 51(6):535–563, 2007.

[139] M. Wörner. Numerical Modeling of Multiphase Flows in Microfluidics and Micro Process Engineering: A Review of Methods and Applications. *Microfluidics and Nanofluidics*, 12(6):841–886, 2012.

[140] Y. Yamamoto, T. Ito, T. Wakimoto, and K. Katoh. Numerical Simulations of Spontaneous Capillary Rises with Very Low Capillary Numbers Using a Front-Tracking Method Combined with Generalized Navier Boundary Condition. *International Journal of Multiphase Flow*, 51:22–32, 2013.

[141] H. Y. Y. Yoon, S. Koshizuka, and Y. Oka. Direct Calculation of Bubble Growth, Departure, and Rise in Nucleate Pool Boiling. *International Journal of Multiphase Flow*, 27(2):277–298, 2001.

[142] V. Zarnescu, R. L. Webb, and L. H. Chien. Effect of Oil On the Boiling Performance of Structured and Porous Surfaces. *HVAC&R Research*, 6:41–53, 2000.

[143] L. Z. Zeng, J. F. Klausner, and R. Mei. A Unified Model for the Prediction of Bubble Detachment Diameters in Boiling Systems— I. Pool Boiling. *International Journal of Heat and Mass Transfer*, 36(9):2261–2270, 1993.

[144] L. Zhang, Z. D. Li, K. Li, H. X. Li, and J. F. Zhao. Influence of Heater Thermal Capacity on Bubble Dynamics and Heat Transfer in Nucleate Pool Boiling. *Applied Thermal Engineering*, 2014.

[145] J. F. Zhao, Z. D. Li, and L. Zhang. Numerical Simulation of Single Bubble Pool Boiling in Different Gravity Conditions. In *Proceedings of the Sixth International Conference on Fluid Mechanics*, Guangzhou, China, 2011.

[146] N. Zuber. Nucleate Boiling. The Region of Isolated Bubbles and the Similarity with Natural Convection. *International Journal of Heat and Mass Transfer*, 6(1):53–78, 1963.

List of Figures

Figures 2.5, 2.6, and 2.11 are reprinted with permission of Elsevier Limited.

List of Tables

A Material Properties

Table A.1: Fluid properties of R134a at saturation from VDI heat atlas [38]

Property	Unit	Value
T_{sat}	°C	20
p_{sat}	$10^5\,\mathrm{Pa}$	5.717
σ	$10^{-3}\,\mathrm{N/m}$	8.78
Δh_{v}	J/kg	182200
ρ_{l}	$\mathrm{kg/m^3}$	1225.3
ρ_{v}	$\mathrm{kg/m^3}$	27.78
c_{l}	J/kgK	1405
c_{v}	J/kgK	1001
ν_{l}	$10^{-7}\,\mathrm{m^2/s}$	1.692
ν_{v}	$10^{-7}\,\mathrm{m^2/s}$	4.135
k_{l}	W/mK	0.08328
k_{v}	W/mK	0.01333

Table A.2: Properties of copper from VDI heat atlas [39]

Property	Unit	Value
ρ	$\mathrm{kg/m^3}$	8900
c	J/kgK	381
k	W/mK	401

B Full Nondimensional Model

The nondimensional numbers employed are

$N^* = \frac{\mu_\mathrm{l}^2}{\rho_\mathrm{v} a \sigma}$	“viscosity number”,
$\rho^* = \frac{\rho_\mathrm{v}}{\rho_\mathrm{l}}$	density ratio,
Θ	contact angle,
$\zeta^* = \zeta_\mathrm{l,up} \frac{a^3}{\mu_\mathrm{l}}$	flow resistance,
$\dot{Q}^* = \frac{\dot{Q}_\mathrm{f} \mu_\mathrm{l}}{\Delta h_\mathrm{v} \rho_\mathrm{v} a^2 \sigma}$	heat flow,
$\Delta p^* = \Delta p \frac{a}{\sigma}$	pressure difference,
$L^* = \frac{L}{a}$	length,
$A^* = \frac{A}{a^2}$	area,
$V^* = \frac{V}{a^3}$	volume,
$\dot{V}^* = \frac{\dot{V} \Delta h_\mathrm{v} \rho_\mathrm{v}}{\dot{Q}}$	volume change rate,
$\Delta\tau^* = \frac{\Delta\tau\sigma}{\mu_\mathrm{l} a}$	bubble departure time.

The pressure difference between the upper liquid film and the liquid pool is given given by Equation (B.1), the pressure difference between the upper and the lower liquid film by Equation (B.2).

$$\begin{aligned} \Delta p^*_\mathrm{l,up} &= -\left(\Delta p^*_\mathrm{b,l} + \Delta p^*_\mathrm{up,v} + \Delta p^*_\mathrm{v,b}\right) && \text{(B.1)} \\ \Delta p^*_\mathrm{up,lo} &= \Delta p^*_\mathrm{up,v} - \Delta p^*_\mathrm{lo,v} && \text{(B.2)} \end{aligned}$$

The pressure differences $\Delta p^*_\mathrm{b,l}$, $\Delta p^*_\mathrm{up,v}$, and $\Delta p^*_\mathrm{lo,v}$ are given by Equation (B.3) with $f(\Theta, V^*, \mathrm{geometry})$ being given by the solution of the Young-Laplace equation.

$$\Delta p^* = f(\Theta, V^*, \mathrm{geometry}) \tag{B.3}$$

The volume change rates can be calculated from Equations (B.4) to (B.6).

$$\begin{aligned} \dot{V}^*_\mathrm{b} &= 1 + \dot{V}^*_\mathrm{lo} + \dot{V}^*_\mathrm{up} && \text{(B.4)} \\ \dot{V}^*_\mathrm{up} &= -0.5\,\rho^* + \frac{\Delta p^*_\mathrm{l,up}}{\dot{Q}^* \zeta^*} - \frac{\Delta p^*_\mathrm{up,lo}}{\dot{Q}^* \zeta^*_\mathrm{up,lo}} && \text{(B.5)} \\ \dot{V}^*_\mathrm{lo} &= -0.5\,\rho^* + \frac{\Delta p^*_\mathrm{up,lo}}{\dot{Q}^* \zeta^*_\mathrm{up,lo}} && \text{(B.6)} \end{aligned}$$

The pressure difference between vapor in the tunnel and bubble is given by Equation (B.7).

$$\Delta p^*_\mathrm{v,b} = 2\left(\frac{\dot{V}^*_\mathrm{b}}{A^*_\mathrm{p}}\right)^2 \frac{\left(\dot{Q}^*\right)^2}{N^*} \tag{B.7}$$

The time for one bubble cycle is given by Equation (B.8).

$$\Delta\tau^* = \frac{V^*_{\mathrm{b,dep}} - V^*_{\mathrm{b,res}}}{\dot{Q}^*} \tag{B.8}$$

The flow resistance between the upper and the lower liquid film is given by Equation (B.9).

$$\zeta^*_{\mathrm{up,lo}} = 3\frac{L^*_{\mathrm{H}}/2}{A^*_{\mathrm{f,up,lo}}\left(\frac{A^*_{\mathrm{f,up,lo}}}{L^*_{\mathrm{f,up,lo}}}\right)^2} \tag{B.9}$$

C Dynamic Forces at the Bubble and in the Film

Klausner et al. [63] introduced the pressured due to the drag of the bubble in the liquid as given in Equation (C.1).

$$\Delta p_{\mathrm{dyn}} = \rho_{\mathrm{l}} \left(R\ddot{R} + \frac{3}{2}\dot{R}^2 \right) \tag{C.1}$$

Zeng et al. [143] extended Equation (C.1) by introducing the empirical parameter $C_{\mathrm{s}} = 20/3$ to Equation (C.2)

$$\Delta p_{\mathrm{dyn}} = \rho_{\mathrm{l}} \left(R\ddot{R} + \frac{3}{2}C_{\mathrm{s}}\dot{R}^2 \right) \tag{C.2}$$

Ramaswamy et al. [103] modeled the lift force, caused by other bubbles as given in Equation (C.3)

$$F_{\mathrm{lift}} = \frac{\pi}{2} C_{\mathrm{lift}} \rho_{\mathrm{l}} \left(4R\dot{R} \right)^2 \tag{C.3}$$

with the empirical constant $C_{\mathrm{lift}} = 1.2$. The liquid inertia force is given by Equation (C.4).

$$F_{\mathrm{l,i}} = V_{\mathrm{b}} \rho_{\mathrm{l}} \ddot{R} \tag{C.4}$$

The forces can be transformed into an additional pressure acting at the liquid-vapor interface with the surface area of the bubble A_{b} as given in Equation (C.5) and (C.6).

$$\Delta p_{\mathrm{lift}} = -\frac{8\pi\rho_{\mathrm{l}}}{A_{\mathrm{b}}} C_{\mathrm{lift}} \left(R\dot{R} \right)^2 \tag{C.5}$$

$$\Delta p_{\mathrm{l,i}} = -\frac{V_{\mathrm{b}}\rho_{l}}{A_{\mathrm{b}}} \ddot{R} \tag{C.6}$$

The pressure increase in the surrounding of the bubble can be given in a general form (C.7).

$$\Delta p_{\mathrm{dyn}} = \rho_{\mathrm{l}} \left(C_{\mathrm{A}} R\ddot{R} + C_{\mathrm{B}} \dot{R}^2 \right) \tag{C.7}$$

For a hemispherical bubble the area of the bubble is given by $A_{\mathrm{b}} = 2\pi R^2$ and the volume by $V_{\mathrm{b}} = 2/3\pi R^3$. Assuming a constant volume flow rate $\dot{V}_{\mathrm{b}}$ to the bubble, the radial velocity and acceleration are given by Equation (C.8).

$$\dot{R} = \frac{\dot{V}_{\mathrm{b}}}{2\pi R^2} \qquad \ddot{R} = -2\frac{\dot{R}^2}{R} \tag{C.8}$$

For a bubble with a spherical shape, the surface area is given by $A_{\mathrm{b}} = 4\pi R^2$ and the volume by $V_{\mathrm{b}} = 4/3\pi R^3$, resulting in a radial velocity and acceleration as given in Equation (C.9).

$$\dot{R} = \frac{\dot{V}_{\mathrm{b}}}{4\pi R^2} \qquad \ddot{R} = -2\frac{\dot{R}^2}{R} \tag{C.9}$$

It shall be noted that the constant bubble growth rate is valid for the domain studied in the CFD simulation, but for several pores, the vapor flow is distributed to several bubbles, with the ratio of the flow rates depending on the pressure inside the bubble. Assuming a hemispherical bubble shape, Equation (C.7) can be written in nondimensional form as given in Equation (C.10).

$$\Delta p^*_{\mathrm{dyn}} = \frac{1}{4}\left(C_{\mathrm{B}} - 2C_{\mathrm{A}}\right)\left(\frac{\dot{V}^*_{\mathrm{b}}}{\pi\left(R^*\right)^2}\right)^2\left(\dot{Q}^*\right)^2\frac{1}{\rho^* N^*} \tag{C.10}$$

The term $1/4\left(C_{\mathrm{B}} - 2C_{\mathrm{A}}\right)$ can be summarized into a new constant C^*. For the case of a spherical bubble, the constant is given by $C^* = 1/16\left(C_{\mathrm{B}} - 2C_{\mathrm{A}}\right)$. The values for C^* considering the different models are given in Table C.1

Table C.1: Constant C^* for different models

	hemispherical bubble	spherical bubble
Klausner et al. [63]	$C_{\mathrm{A}} = 1$, $C_{\mathrm{B}} = 3/2$, $C^* = -0.125$	$C_{\mathrm{A}} = 1$, $C_{\mathrm{B}} = 3/2$, $C^* \approx -1/32$
Zeng et al. [143]	$C_{\mathrm{A}} = 1$, $C_{\mathrm{B}} = 10$, $C^* = 2$	$C_{\mathrm{A}} = 1$, $C_{\mathrm{B}} = 10$, $C^* = 0.5$
Ramaswamy et al. [103]	$C_{\mathrm{A}} = 4/3$, $C_{\mathrm{B}} = 5.2$, $C^* \approx 2/3$	$C_{\mathrm{A}} = 4/3$, $C_{\mathrm{B}} = 7.6$, $C^* \approx 1/3$

The Reynolds number of the liquid film in the pore can be approximated as given in Equation (C.11).

$$Re_{\mathrm{f}} = \frac{\rho_{\mathrm{l}} u L_{\mathrm{char}}}{\mu_{\mathrm{l}}} \tag{C.11}$$

The average velocity of the film is given by Equation (C.12).

$$u = \frac{\dot{Q}_{\mathrm{f}}}{\Delta h_{\mathrm{v}} \rho_{\mathrm{l}} A_{\mathrm{p}}} = \frac{\dot{Q}^* \sigma \rho_{\mathrm{v}}}{\mu_{\mathrm{l}} A^*_{\mathrm{p}} \rho_{\mathrm{l}}} \tag{C.12}$$

Replacing $A^*_{\mathrm{p}}/L^*_{\mathrm{char}}$ by R^*_{p}, Equation (C.13) is obtained.

$$Re_{\mathrm{f}} = \frac{\dot{Q}^*}{N^* R^*_{\mathrm{p}}} \tag{C.13}$$

D Source Code for Generating Liquid Film in SURFACE EVOLVER

```
// Input Parameters
PARAMETER   angle = 20                              // contact angle
PARAMETER   TLENGTH =0.24                           // width of ledge
PARAMETER   BSTEG=0.06                              // half thickness of ledge
PARAMETER   BLENGTH =0.94                           // half pore distance - half thickness of ledge
PARAMETER   HLENGTH =1.14                           // half tunnel height
PARAMETER   VOL= 0.1                                // film volume
PARAMETER   tens = 1                                // surface tension

PARAMETER   startFac=sqrt(2*VOL/(TLENGTH+BLENGTH+HLENGTH));
gravity_ constant 0                                 // gravity
#define WALLT (-cos(angle*pi/180)*tens)             // virtual tension of facet on plane

//Contraints for boundaries
constraint 1
formula: x1 = 0
constraint 2
formula: x2 = 0
constraint 3
formula: x3 = 0
constraint 4
formula: x1 = TLENGTH
constraint 5
formula: x2 = BLENGTH
constraint 6
formula: x3 = HLENGTH
constraint 10
formula: x2 = -BSTEG
constraint 7
formula x3 = 0
energy: e1: -(WALLT*y) e2: 0 e3: 0
constraint 8
formula x1 = 0
energy: e1: 0 e2: -(WALLT*z) e3: 0
constraint 9
formula x2 = 0
energy: e1: (WALLT*z) e2: 0 e3: 0
constraint 11
formula x1 = TLENGTH
energy: e1: 0 e2: -(WALLT*z) e3:0
constraint 12
formula x3 = 0
energy: e1: 0 e2: (WALLT*x-WALLT*TLENGTH) e3: 0
constraint 13 nonpositive
formula x1-TLENGTH
constraint 14 nonpositive
```

```
formula x3-HLENGTH
constraint 15 nonnegative
formula x1
constraint 16 nonnegative
formula x2
constraint 17 nonnegative
formula x3

// building the initial geometry
vertices
1      TLENGTH startFac 0.0              constraint 3
2      startFac startFac 0               constraint 3
3      startFac BLENGTH 0.0              constraint 3,5
4      0.0 BLENGTH startFac              constraint 1,5,14
5      0 startFac startFac               constraint 1,14
6      0.0 startFac HLENGTH              constraint 1,6
7      startFac 0.0 HLENGTH              constraint 2,6,13
8      startFac 0 startFac               constraint 2,13
9      TLENGTH 0.0 startFac              constraint 2,4,17
10     TLENGTH 0.0 0.0                   fixed
11     0.0 BLENGTH 0.0                   fixed
12     0.0 0.0 HLENGTH                   fixed
13     TLENGTH+startFac 0.0 0.0          constraint 2,3
14     TLENGTH+startFac -BSTEG 0.0       constraint 10,3
15     TLENGTH -BSTEG startFac           constraint 10,4
16     TLENGTH -BSTEG 0.0                fixed

edges  // given by endpoints of vertices
1      1 2          constraint 7
2      2 3          constraint 7
3      3 4          constraint 5
4      4 5          constraint 8,14
5      5 6          constraint 8,14
6      6 7          constraint 6
7      7 8          constraint 9,13
8      8 9          constraint 9,13
9      9 1
10     8 2          constraint 16
11     2 5
12     5 8          constraint 16
13     10 16        fixed no_refine
14     3 11         constraint 5,7 no_refine
15     11 4         constraint 1,5 no_refine
16     6 12         constraint 8,6 no_refine
17     12 7         constraint 9,6 no_refine
18     9 10         constraint 2 no_refine
19     9 13
20     13 1         constraint 7
21     9 15         constraint 11
22     15 14        constraint 10
23     14 13        constraint 12
24     16 15        constraint 10,4 no_refine
25     16 14        constraint 10,3 no_refine
26     9 16         constraint 4, no_refine
27     9 14
```

```
faces   // given by oriented edge loop
1       1 -10 8 9       tension tens constraint 15,16,17
2       2 3 4 -11       tension tens constraint 15,16,17
3       5 6 7 -12       tension tens constraint 15,16,17
4       10 11 12        tension tens constraint 15,16,17
5       13 -26 18       no_refine tension 0
6       14 15 -3        no_refine tension 0
7       16 17 -6        no_refine tension 0
8       19 20 -9        tension tens constraint 15,16,17
9       25 -22 -24      no_refine tension 0
10      22 -27 21       tension tens constraint 17
11      27 23 -19       tension tens constraint 17
12      24 -21 26       no_refine tension 0

bodies  // one body, defined by its oriented faces
1       1 2 3 4 5 6 7 8 9 10 11 12      volume VOL      density 0

// methods
read
// Local refinement
groom := { refine edges where length > 0.1 and not fixed and not no_refine; u; V; u; V; };

// Iterate until convergence with refinement
gogo:=
{
        change:=100; olden:=total_energy; countr:=0;
        for (countr:=0; countr<=3;countr+=1)
        {
                countiter:=0; change:=100;
                while change>1e-7 and countiter<1000 do
                {
                        g 100;
                        change:=abs(olden-total_energy);
                        olden:=total_energy;
                        countiter+=1;
                        if countiter==1000 then {printf"Warning, not converged"};
                        if change<=1e-7 then
                        {
                                foreach facet ff do
                                {
                                        if ff.area ==0 then {V 5; u 2; V 5; change:=1};
                                };
                        }
                };
                if countr<2 then { groom 2; };
                if countr==2 then { r; u; V; }
        }
}
```

Curriculum vitae

Name	Jochen Dietl
Geburtsdatum	1. August 1986
Geburtsort	Ulm

Schulbildung

1993 – 1997	Grundschule Illerkirchberg
1997 – 2006	Alber-Einstein-Gymnasium Ulm

Studium

2006 – 2008	TU Darmstadt, Bachelorstudium Maschinenbau
2008 – 2009	Virginia Tech, Bachelorstudium Maschinenbau
2009 – 2011	TU Darmstadt, Masterstudium Maschinenbau

Berufliche Tätigkeit

seit 2011	TU Darmstadt, Fachgebiet Technische Thermodynamik Wissenschaftlicher Mitarbeiter